



저작자표시-비영리-변경금지 2.0 대한민국

이용자는 아래의 조건을 따르는 경우에 한하여 자유롭게

- 이 저작물을 복제, 배포, 전송, 전시, 공연 및 방송할 수 있습니다.

다음과 같은 조건을 따라야 합니다:



저작자표시. 귀하는 원저작자를 표시하여야 합니다.



비영리. 귀하는 이 저작물을 영리 목적으로 이용할 수 없습니다.



변경금지. 귀하는 이 저작물을 개작, 변형 또는 가공할 수 없습니다.

- 귀하는, 이 저작물의 재이용이나 배포의 경우, 이 저작물에 적용된 이용허락조건을 명확하게 나타내어야 합니다.
- 저작권자로부터 별도의 허가를 받으면 이러한 조건들은 적용되지 않습니다.

저작권법에 따른 이용자의 권리는 위의 내용에 의하여 영향을 받지 않습니다.

이것은 [이용허락규약\(Legal Code\)](#)을 이해하기 쉽게 요약한 것입니다.

[Disclaimer](#)

공학박사 학위논문

**Fabrication and Application of  
Organic/Inorganic Hybrid Nanoparticles for  
Cancer Imaging and Therapy**

암 진단 및 치료를 위한 하이브리드 나노입자의 제조 및  
응용에 관한 연구

2012년 8 월

서울대학교 대학원

재료공학부

차 의 준

# Fabrication and Application of Organic/Inorganic Hybrid Nanoparticles for Cancer Imaging and Therapy

지도 교수 안 철 희

이 논문을 공학박사 학위논문으로 제출함

2012 년 5 월

서울대학교 대학원

재료공학부

차 의 준

차의준의 박사 학위논문을 인준함

2012 년 5 월

위 원 장 \_\_\_\_\_ (인)

부위원장 \_\_\_\_\_ (인)

위 원 \_\_\_\_\_ (인)

위 원 \_\_\_\_\_ (인)

위 원 \_\_\_\_\_ (인)

## **Abstract**

# **Fabrication and Application of Organic/Inorganic Hybrid Nanoparticles for Cancer Imaging and Therapy**

Eui-Joon Cha

Department of Materials Science and Engineering

College of Engineering

Seoul National University

Theranagnosis, combined diagnosis using various imaging modalities and efficient drug delivery system, is an emerging research topic in biomedical field. This study described a novel platform technology for theragnostic materials based on superparamagnetic iron oxide nanoparticle (SPION), polymeric micelles and calcium phosphate.

In the first part, fluorescence quenching property of SPION was demonstrated (chapter 2) and distance dependent quenching effect was observed using silica coated iron oxide nanoparticles. Imaging probes based

on silica/PEG (chapter 3) or glycol chitosan (chapter 4) coated SPION was developed. Developed imaging probes showed tumor selective fluorescence recovery due to selective cleavage of fluorophore labeled MMP specific peptides, decorated on the surface of nanoparticles. Furthermore, tumor was successfully visualized in vivo by magnetic resonance imaging.

In the second part, amphiphilic block copolymer containing carboxyl acid groups on the junction point was synthesized and polymeric micelles based on the prepared block copolymer were investigated as a potential drug delivery system. Micelles were stabilized by ionic interaction between cation and carboxyl acid groups in the block copolymer.

In the third part, theragnostic nanoparticles were developed and the potential as a theragnostic agent was demonstrated. For CT and MRI imaging, gold nanoparticle (chapter 7) and iron oxide nanoparticle (chapter 8) were used respectively. Nanoparticles were coated with block copolymer and calcium phosphate for drug encapsulation. Block copolymers with PEG and aspartic acid were used for immobilization of calcium ion and doxorubicin. Drug loaded hybrid nanoparticles were successfully synthesized and showed pH dependent solubility drug release profile due to pH sensitivity of calcium phosphate layers. In addition, prepared nanoparticles based on iron oxide

were imaged by magnetic resonance imaging in vivo.

**Keywords:** Theragnosis, molecular imaging, iron oxide nanoparticle, gold nanoparticle, drug delivery system

**Student Number:** 2007-30810

## **Contents**

<b>Abstract</b> .....	<b>i</b>
<b>Contents</b> .....	<b>iv</b>
<b>List of Tables and Schemes</b> .....	<b>viii</b>
<b>List of Figures</b> .....	<b>ix</b>

### **Chapter 1.**

<b>Introduction</b> .....	<b>1</b>
1.1 Nanomaterials in theragnosis .....	2
1.2 Enhanced permeability and retention effect in cancer .....	3
1.3 Molecular imaging modalities in cancer imaging .....	7
1.4 Multi modal imaging.....	9
1.5 Activatable fluorescence imaging.....	11
1.6 Research objectives.....	14
1.7 References .....	17

### **Chapter 2.**

<b>Distance-dependent fluorescence quenching of fluorophore labeled iron oxide core-shell nanoparticles with high T2 relaxivity</b> .....	<b>22</b>
---	-----------

2.1	Introduction .....	23
2.2	Experimental.....	27
2.3	Results and discussion .....	32
2.4	Conclusion.....	45
2.5	References .....	46

### **Chapter 3.**

#### **Development of MRI/NIRF ‘activatable’ multimodal imaging probe based on iron oxide nanoparticles ..... 50**

3.1	Introduction .....	51
3.2	Experimental.....	53
3.3	Results and discussion .....	56
3.4	Conclusion.....	67
3.5	References .....	68

### **Chapter 4.**

#### **Activatable NIRF/MRI dual imaging probe using glycol chitosan coated superparamagnetic iron oxide nanoparticles ..... 72**

4.1	Introduction .....	73
4.2	Experimental.....	75
4.3	Results and discussion .....	80

4.4	Conclusion.....	90
4.5	References .....	91

## **Chapter 5.**

### **Stabilized polymeric micelles by electrostatic interactions for drug delivery system ..... 94**

5.1	Introduction .....	95
5.2	Experimental.....	97
5.3	Results and discussion .....	104
5.4	Conclusion.....	116
5.5	References .....	117

## **Chapter 6.**

### **pH sensitive drug delivery system using ionically stabilized polymeric micelles ..... 121**

6.1	Introduction .....	122
6.2	Experimental.....	123
6.3	Results and discussion .....	126
6.4	Conclusion.....	133
6.5	References .....	134

## **Chapter 7.**

### **Development of novel nanocarriers for pH sensitive drug release using calcium phosphate coated gold nanoparticles ..... 137**

7.1	Introduction .....	138
7.2	Experimental.....	140
7.3	Results and discussion .....	146
7.4	Conclusion.....	161
7.5	References .....	162

## **Chapter 8.**

### **Development of calcium phosphate coated superparamagnetic iron oxide nanoparticles for combined MRI and drug delivery ..... 168**

8.1	Introduction .....	169
8.2	Experimental.....	171
8.3	Results and discussion .....	177
8.4	Conclusion.....	189
8.5	References.....	189

### **국문 요약 ..... 193**

## **List of Tables and Schemes**

**Table 2-1.** Sample codes, diameters and  $\zeta$ -potential of each sample.

**Table 2-2.** Fluorescence intensity of CY-CS nanoparticles with/without HF treatment, number of Cy5.5 on a particle and quenching efficiency.

**Table 5-1.** Adjustment of the number of aspartic acids.

**Scheme 5-1.** Synthetic procedure of mPEG–Asp–PCL.

**Scheme 7-1.** Synthetic scheme of mPEG-Asp-Cys.

**Scheme 8-1.** Synthetic scheme of mPEG-Asp(OBzl)<sub>50</sub>-DOPAC.

## List of Figures

**Figure 1-1.** Schematic illustration of concept of theragnosis.

**Figure 1-2.** Various nanomaterials for bioapplication.

**Figure 1-3.** Enhanced permeation and retention (EPR) effect in tumor region.

**Figure 1-4.** Molecular imaging modalities for cancer imaging.

**Figure 1-5.** Schematic illustration of fluorescence resonance energy transfer (FRET) and self quenching effect by FRET.

**Figure 1-6.** Fluorescence quenching effect of gold nanoparticle.

**Figure 1-7.** Comparison of computed tomography and magnetic resonance imaging.

**Figure 1-8.** Schematic illustration of research objectives.

**Figure 2-1.** Schematic diagram of core-shell nanoparticle formation.

**Figure 2-2.** TEM images of CS nanoparticles. (a) CS20, (b) CS33, (c) CS60, and (d) CS113 (scale bar: 50 nm).

**Figure 2-3.** Fluorescence spectra of CY-CS nanoparticles. (a) Before HF treatment. (b) After HF treatment. (c) NIRF image of CY-CS nanoparticles.

**Figure 2-4.** T2-weighted MR images of PEGylated CS nanoparticles and Feridex.

**Figure 2-5.** Cell viability of (a) CS20 and (b) PEGylated CS20.

**Figure 2-6.** In vivo (a) MR, (b) NIRF image and (c) NIRF image of excised tumor with CY-CS20 and CY-CS113.

**Figure 3-1.** Fabrication method of PCM-CS; (i) Triton-X, 1-Octanol, TEOS, NH<sub>4</sub>OH, Cyclohexane, rt, 72 h; (ii) APTES, EtOH, 25 °C, 6 h; (iii) Cy5.5-MMP substrate, EDC, NHS, H<sub>2</sub>O, 25 °C, 12 h; (iv) mPEG-COOH, EDC, NHS, H<sub>2</sub>O, 25 °C, 12 h.

**Figure 3-2.** (a) TEM images of PCM-CS nanoparticles, (b) size distribution of PCM-CS by dynamic light scattering, (c) stability of PCM-CS in PBS, (d) Fluorescence spectra of PCM-CS, HF treated PCM-CS, MMP-2 treated PCM-CS, and CS20.

**Figure 3-3.** Fluorescence recovery against MMP-2 in various condition (a) time dependent fluorescence spectra with 15 nM MMP-2, (b) time dependent fluorescence change at 695 nm, and (c) NIRF image sections of a 96-well microplate of the PCM-CS containing various MMP-2

concentration and (d) corresponding fluorescence intensity at 695 nm.

**Figure 3-4.** NIRF tomographic images of tumor-bearing mice after injection of PCM-CS (a) without inhibitor, (b) with inhibitor and (c) normal mice after injection of PCM-CS (blue: low intensity, red: high intensity).

**Figure 3-5.** Images of excised organs and tumor at 24 h post injection of PCM-CS (a) white light image, (b) NIRF image and (c) merged image.

**Figure 3-6.** Magnetic resonance images of PCM-CS treated mice at various time points, (a) Pre-injection (b) 3 h, (c) 6 h, (d) 12 h, (e) 24 h after injection, and (f) relative T2 intensity of tumor regions.

**Figure 4-1.** (a) Synthesis of GC-DOPAC and (b) fabrication of BCMG-SPION; (i) DOPAC, EDC, NHS, DMSO, rt, 24 h; (ii) GC-DOPAC, H<sub>2</sub>O, 6 h; (iii) Cy5.5-MMP substrate-BHQ, EDC, NHS, H<sub>2</sub>O, 25 °C, 12 h.

**Figure 4-2.** (a) TEM image and (b) size distribution of BCMG-SPION.

**Figure 4-3.** (a) Fluorescence spectra and (b) NIRF images of BCMG-SPION after 2 h reaction with MMP-2.

**Figure 4-4.** NIRF tomographic images of tumor-bearing mice after injection of (a) BCMG-SPION without inhibitor, (b) fluorescence intensity of tumor site and (c) BCMG-SPION with inhibitor (blue: low intensity, red:

high intensity).

**Figure 4-5.** (a) NIRF images and (b) signal intensity of ROI of excised organs and tumor at 48 h post injection of BCMG-SPION.

**Figure 4-6.** (a) Magnetic resonance images of PCM-CS treated mice at various time points, (b) relative T2 intensity of tumor regions.

**Figure 5-1.** Chemical structure and  $^1\text{H-NMR}$  spectra of mPEG-Asp(OBzl) in  $\text{CDCl}_3$ : (a) chemical structure; (b), (c)  $^1\text{H-NMR}$  spectra.

**Figure 5-2.**  $^1\text{H}$  NMR spectrum of mPEG-Asp-PCL in  $\text{DMSO-d}_6$ .

**Figure 5-3.** GPC traces of activated PCL, mPEG-Asp(OBzl) and mPEG-Asp-PCL using THF as an eluent.

**Figure 5-4.** Size distribution of (a) non-stabilized micelle; (b) ionically stabilized micelle; (c) paclitaxel-loaded micelle; (d) ionically stabilized and paclitaxel-loaded micelle.

**Figure 5-5.** Ratio of intensity at 373 nm and 383 nm of pyrene emission spectra as a function of log concentration: (a) non-stabilized micelle; (b) stabilized micelle.

**Figure 5-6.** Pictures of non-stabilized and ionically stabilized micelle

solution at the concentration of (a) 2.0 mg/mL above CMC, and (b) 0.02 mg/mL below CMC.

**Figure 5-7.** In vitro paclitaxel release profiles from non-stabilized micelles (●) and ionically stabilized micelles (△) in aqueous medium at 37 °C.

**Figure 6-1.** (a) Chemical structure of mPEG-Asp-PCL. Size distribution of (b) doxorubicin-loaded micelle; (c) ionically stabilized doxorubicin-loaded micelle.

**Figure 6-2.** In vitro doxorubicin release profiles from non-stabilized micelle (■) and stabilized micelle (●) at 37 °C.

**Figure 6-3.** Plausible mechanism of pH dependent drug release patterns from (a) non-stabilized micelle and (b) stabilized micelle.

**Figure 7-1.** GPC traces of mPEG-Asp(OBzl) and mPEG-NH<sub>2</sub> using DMF as an eluent.

**Figure 7-2.** NMR spectra of (a) mPEG-Asp(OBzl)-Cys(Z) and (b) mPEG-Asp-Cys.

**Figure 7-3.** Synthetic method of PEGylated Dox-Au@CaP.

**Figure 7-4.** (a) TEM image, (b) size distribution, (c) stability of PEGylated Dox-AuNP@CaP with/without GSH and (d) UV spectra of PEGylation Dox-Au@CaP and PEGylated AuNP with GSH.

**Figure 7-5.** Drug release profiles of PEGylated Dox-Au@CaP.

**Figure 7-6.** Cytotoxicity of PEGylated Dox-Au@CaP and PEGylated Au@CaP as a function of (a) incubation time and (b) concentration.

**Figure 7-7.** Schematic illustration of (a) Tumor specific NIRF probe based on gold nanoparticle, (b) NIRF/CT dual imaging probe based on gold nanoparticle and (c) calcium phosphate coated gold nanoparticle for therngnosis.

**Figure 8-1.** Fabrication method of PEGylated Dox-FeO<sub>x</sub>@CaP ; i) PEG-Asp(Obzl)<sub>50</sub>-DOPAC, 12 h; ii) 0.1 N NaOH aq. solution, 6 h; iii) Dox, 2 h; iv) CaCl<sub>2</sub>, 1 h; v) Na<sub>2</sub>HPO<sub>4</sub>, 12 h.

**Figure 8-2.** (a) TEM image and (b) size distribution in PBS of PEGylated Dox-FeO<sub>x</sub>@CaP.

**Figure 8-3.** Doxorubicin release profiles of PEGylated Dox-FeO<sub>x</sub>@CaP with media change (■) and without media change (□).

**Figure 8-4.** Cell viability of PEGylated Dox-FeO<sub>x</sub>@CaP as a function of

(a) incubation time and (b) Fe concentration.

**Figure 8-5.** Magnetic resonance images after (a) intratumoral injection of particles, intravenous injection of (b) particles and (c) saline.

**Figure 8-6.** Immunohistological results with Prussian blue staining after (a) intratumoral injection of particles, intravenous injection of (b) particles and (c) saline.

**Figure 8-7.** Fluorescence image of tumors at 530 nm emission after (a) intratumoral injection of particles, intravenous injection of (b) particles and (c) saline.

# **Chapter 1.**

## **Introduction**

## **1.1. Nanomaterials in theragnosis**

Theragnosis is treatment strategy that combines therapy with diagnosis to develop personalized medicines with enhanced efficacy. Essential requirements for theragnosis are an efficient drug delivery system with target-specificity and controlled drug release at the target site as well as an imaging probe to selectively image the disease sites in anatomical and functional ways for an effective diagnosis (Figure 1-1) <sup>[1]</sup>.

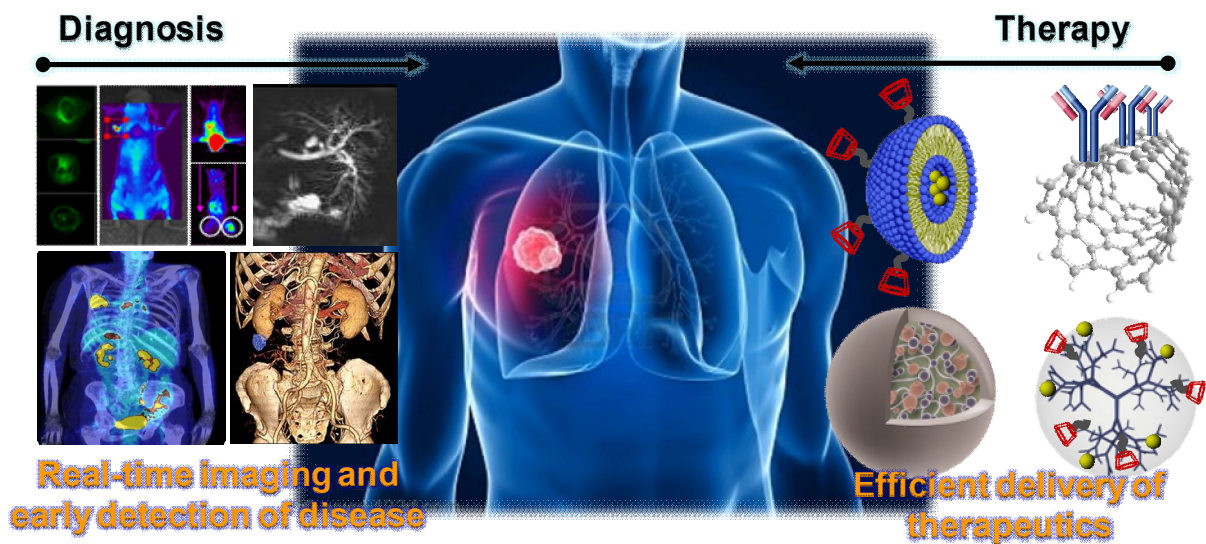
Nanotechnology has led the evolutions in theragnosis, as a result of the development of variety materials with size dimensions in the range of 1-200 nm, and their unique properties that are not found in their bulk materials. These properties include quantum confinement in quantum dots, superparamagnetism in certain oxide nanoparticles, and surface plasmon resonance in noble metal nanoparticles, among others. Because of these unique properties, a number of nanomaterials, such as noble metal nanoparticles, carbon nanotube, iron oxide nanoparticles and others, are investigated as a potential molecular imaging agent with high sensitivity and cost-effective imaging agents. Gold and silver nanoparticles are investigated for contrast agent of computed tomography and optical quencher due to their high X-ray absorption and surface plasmon resonance. Iron oxide

nanoparticles with superparamagnetism were developed as a contrast agent for magnetic resonance imaging. Above this, quantum dots and carbon nanotube have been researched as imaging probes for fluorescence imaging and photoacoustic imaging. Polymeric materials, such as micelle, liposome and dendrimer, are have been researched as a delivery carrier of therapeutics and imaging agents. Micelle and liposome have hydrophobic interior which appropriate to encapsulate hydrophobic agents and can be used to increase local concentration of therapeutic and imaging agent by carrying the drug to the disease site. Numerous natural and synthetic polymers are used as delivery carrier and some of them are clinically approved. Recently, hybrid materials, with metallic/inorganic nanomaterials as an imaging agent and polymeric matierlas as a delivery carrier, have been focused for efficient theragnosis (Figure 1-2) <sup>[1-6]</sup>.

## **1.2. Enhanced permeability and retention effect in cancer**

Of the tumor targeting strategies, the enhanced permeability and retention (EPR) effect of nanoparticles is one of the key mechanism for solid tumor targeting. When tumor cells grow and cell cluster reaches a size of 2-3 mm, angiogenesis is induced to cater for the ever-increasing nutrition

and oxygen demands of the growing tumor <sup>[7]</sup>. This neovasculature is different with vasculature of normal tissues in microscopic anatomical



## Therapy + Diagnosis → Theragnosis

**Figure 1-1.** Schematic illustration of concept of theragnosis.

architecture <sup>[8]</sup>. The shape of blood vessels in the tumor are irregular dilated, leaky or defective, and the alignment of endothelial cells are poor and disorganized. Also, tumor vessels have a wide lumen, whereas tumor tissues have poor lymphatic drainage <sup>[9-11]</sup>. This abnormal structure of vasculature results in extensive leakage of blood plasma components, such as

macromolecules and nanoparticles, into the tumor tissue. Moreover, the poor lymphatic clearance means that nanoparticles are retained in the tumor, whereas extravasation into tumor interstitium continues (Figure 1-3). This phenomenon, termed the EPR effect, was discovered by H. Maeda group, and is the basis for the selective targeting of nanoparticles to the tumors [12].

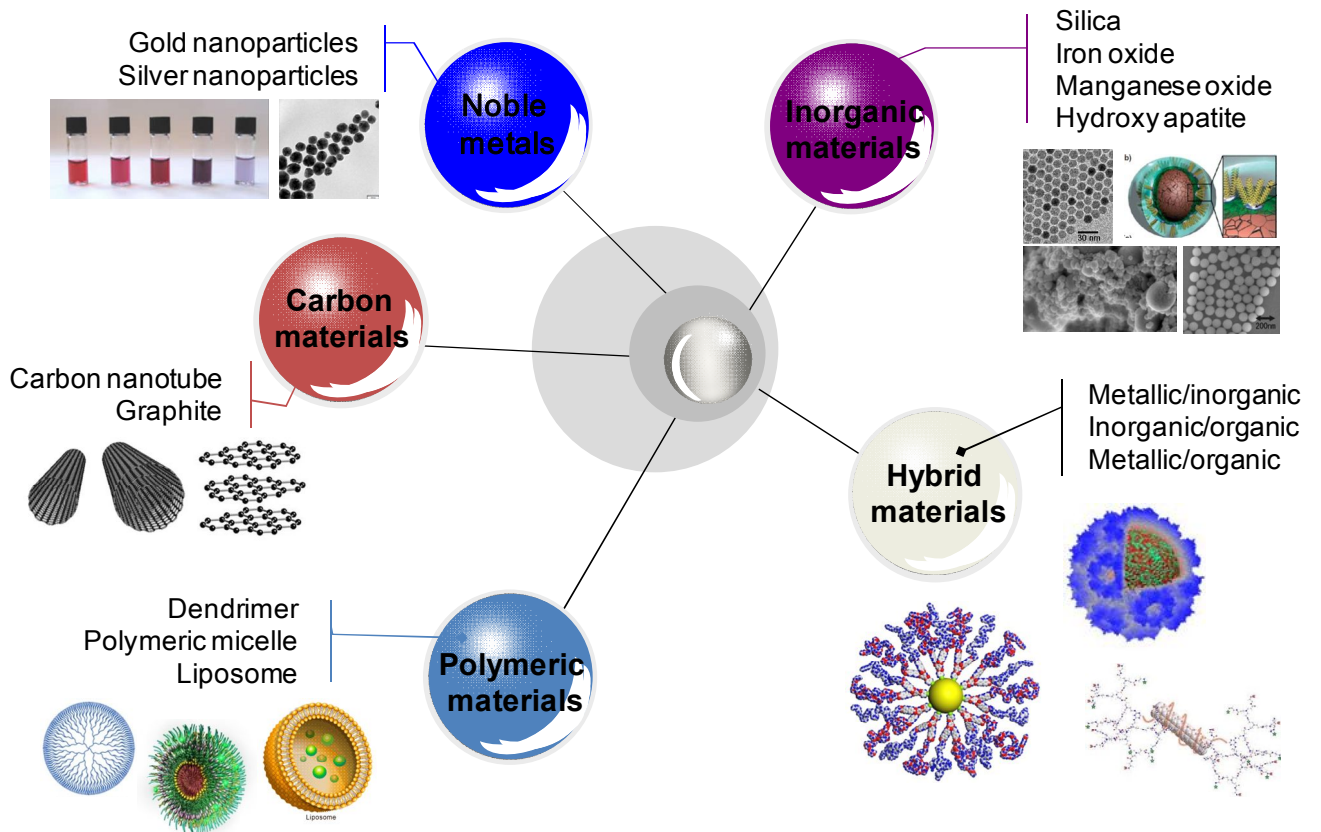


**Figure 1-2.** Various nanomaterials for bioapplication.

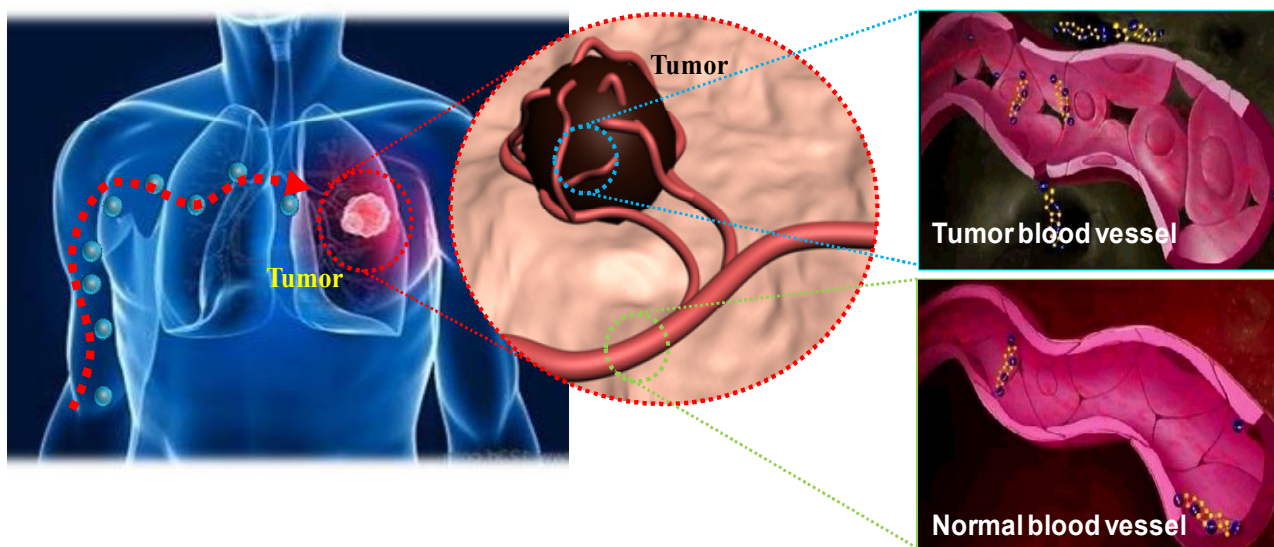


**Figure 1-3.** Enhanced permeation and retention (EPR) effect in tumor region.

For last decades after discovery, a number of nano-sized carriers were developed for drug delivery and imaging based on EPR effect and became a standard of tumor targeting. Inorganic nanoparticles, metal nanoparticles, polymer conjugate based nanoparticles and polymeric micelles are the most well-established materials for tumor targeted drug delivery carrier and imaging probe.

### **1.3. Molecular imaging modalities in cancer imaging**

The goal of the molecular imaging is provision of anatomical information, characterization and quantification of biological events, such as gene regulation, disease progression and enzyme activity, in intact living subjects. For these purpose, a number of imaging modalities, such as magnetic resonance imaging, computed tomography, ultrasound sonography, optical imaging, positron emission tomography (PET) and single photoemission tomography (SPECT), are developed and widely used in clinical use (Figure 1-4).

CT is one of the well-known and widely used imaging modality in clinical practice. In CT, X-rays are emitted from an X-ray source rotating around a subject placed in the center of the CT scanner and the amount of X-ray absorption is detected by a detector on the opposite side. Based on the X-ray absorption, high-resolution tomographic anatomical images are provided with a spatial resolution of up to  $\sim 6 \mu\text{m}$  in small animal scanners<sup>[13]</sup>. While CT is able to provide high resolution image, CT is limited by poor soft tissue contrast. Furthermore, a large amount of contrast agent are needed to obtain enhanced contrast of soft tissue due to the low sensitivity and X-ray radiation problems are also remained.

MRI is a medical imaging technique used in radiology to visualize internal structures of the body in detail. MRI makes use of the property of nuclear magnetic resonance (NMR) to image nuclei of atoms inside the body. MRI provides excellent contrast between the different soft tissues of the body and specialized to image the brain, muscles, the heart, and cancers compared with other medical imaging techniques such as CT or X-rays. Unlike CT scans or traditional X-rays, MRI has advantages in terms of radiation problem and contrast agent dose <sup>[14-17]</sup>.

Optical imaging uses fluorescence and bioluminescence which are based on the absorption of energy from an external excitation light of one wavelength by a fluorophore (fluorescence imaging) and light generated by a chemiluminescent reaction, respectively. Optical imaging is highly sensitive, and quick and easy to obtain imaging signal with relatively low cost. For these reasons, optical imaging is widely used for drug screening and validation process. Optical imaging has several limitations for in vivo application such as low penetration depth and autofluorescence problems. To overcome these problems, light in the range of near infrared region was used due to the low tissue absorption and relatively high penetration depth of near infrared.

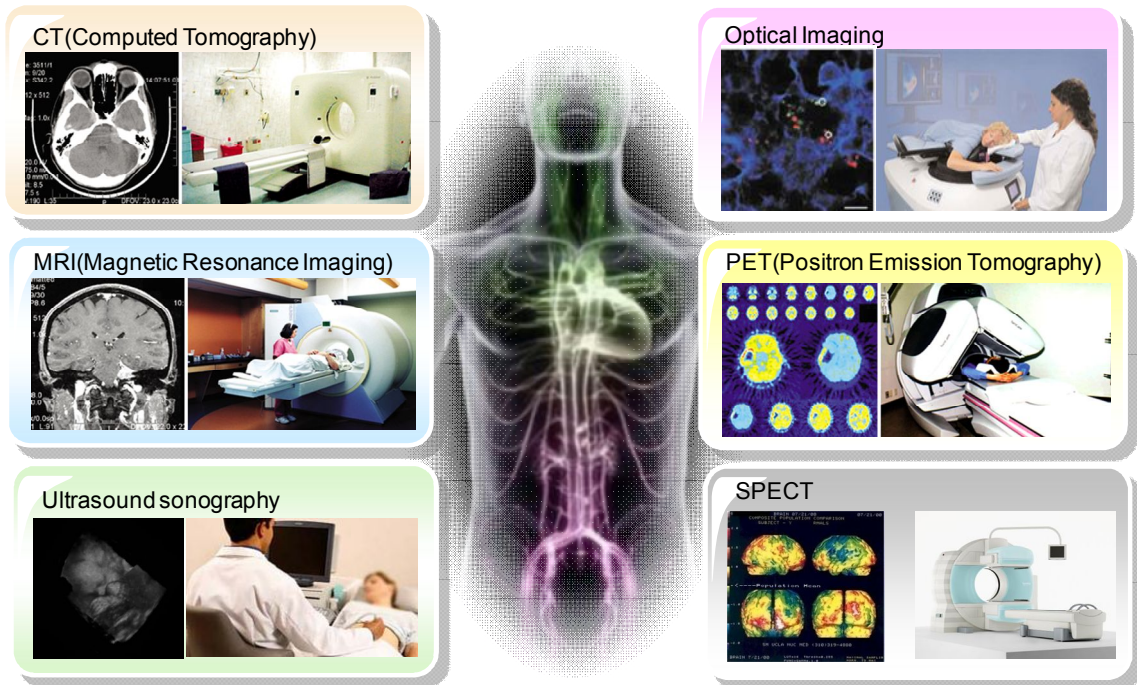


**Figure 1-4.** Molecular imaging modalities for cancer imaging.

#### 1.4. Multi modal imaging

Imaging modalities can be broadly divided into anatomical and functional imaging. Anatomical imaging technique such as computed tomography, magnetic resonance imaging and ultrasound, are characterized by high spatial resolution. However, they also have limitations of disable to detect disease progress until structural changes of tissues are clear enough to

be detected by the imaging modality.

In contrast, functional imaging modalities such as optical imaging, PET and SPECT, provide a potential to detect molecular change of disease before the disease is progress enough to cause structural changes. However, these modalities have a limitation due to their poor spatial resolution with currently available techniques.

Combining the strengths of anatomical and functional imaging modalities allows the detection of physiological changes in early phase of disease at high spatial resolution and provides a potential to overcome limitations of each imaging modalities. For these reasons, multi modal imaging techniques, which have two or more imaging modalities, were investigated extensively. MRI/optical<sup>[18-29]</sup>, MRI/PET<sup>[30-32]</sup> and PET/CT<sup>[33-34]</sup> is the most well-known combinations that have both anatomical imaging modality and functional imaging modality. Combination of MRI and optical imaging has focused for decade because they are highly complementary imaging techniques and widely used in clinical practice. MRI is a great technique for providing anatomical information, but has limitation in detecting molecular events such as gene expression and protease activity. On the other hand, optical imaging can visualize functional events at

molecular level using various fluorescent probes, but it provides insufficient anatomical information. Combination of these two imaging modalities complements each weakness and maximizes strengths.

### **1.5. Activatable fluorescence imaging**

A number fluorescence probes was developed based on fluorescence resonance energy transfer (FRET) properties. FRET is a mechanism describing energy transfer between two fluorophores. FRET is a distance-dependent interaction between the electronic excited states of two dye molecules in which excitation is transferred from a donor molecule to an acceptor molecule without emission of a photon. Schematic illustration of the FRET is shown in Figure 1-5. In some cases, self quenching effect was observed due to FRET and imaging probes using this self quenching effect were reported. Weisslder group reported poly L-lysine based imaging probe using enzyme specific peptide and cyanine dye. Fluorescence of the probe was quenched by FRET in normal state and fluorescence was recovered by cleavage of peptide linker <sup>[35]</sup>.

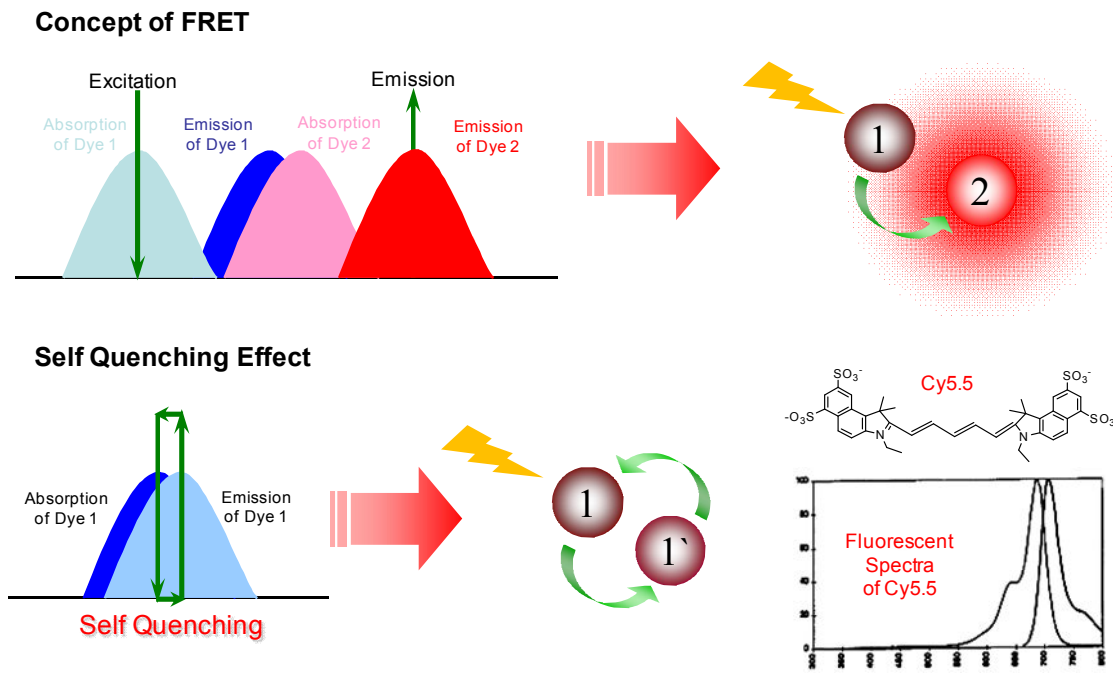


**Figure 1-5.** Schematic illustration of fluorescence resonance energy transfer (FRET) and self quenching effect by FRET.

However, FRET based optical imaging probes have limitation due to their insufficient quenching efficacy and gold nanoparticles are focused for efficient fluorescence quenching, consequently. Noble metal nanoparticles such as gold/silver nanoparticles <sup>[36]</sup> offer a considerable advantage in obtaining optical images through their nearinfrared-fluorescence (NIRF) quenching properties. Chromophores in close proximity to gold

nanoparticles (with in 10 nm) experience strong electronic interactions with the surface, which results in donation of excited electrons to the metal nanoparticles and almost perfect quenching of the fluorescence (Figure 1-6) [37, 38]

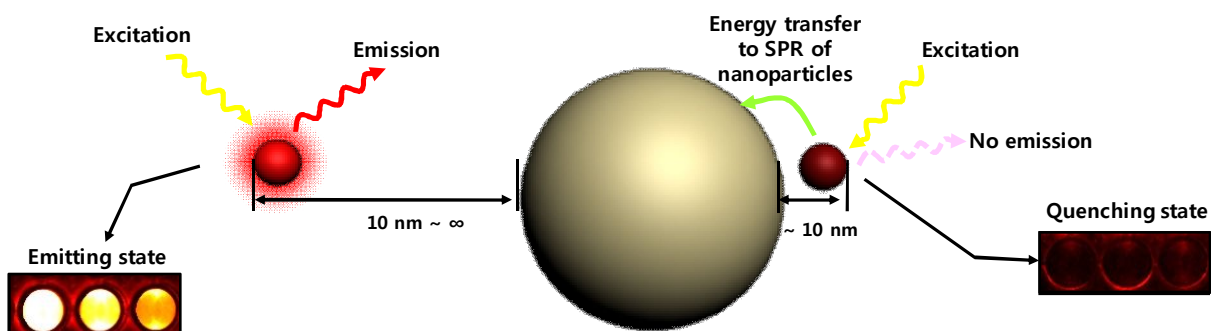


**Figure 1-6.** Fluorescence quenching effect of gold nanoparticle.

In 2006, Mirkin et. al. described the use of Cy5.5 labeled nucleotide conjugated gold nanoparticles that could detect specific gene regulation. Specific DNase detectable probe was fabricated using nucleotides which cleaved by target DNase and gold nanoparticles. Fluorescence of the probe was recovered with target DNase and gene regulation was measured by degree of the fluorescence recovery [39]. Recently, Glycol chitosan coated gold nanoparticle based NIRF/CT dual imaging probe was developed using

fluorescence quenching effect of gold nanoparticles. The probe was activated by MMP enzyme in tumor tissue and successfully recovered fluorescence at tumor site in vivo [40].

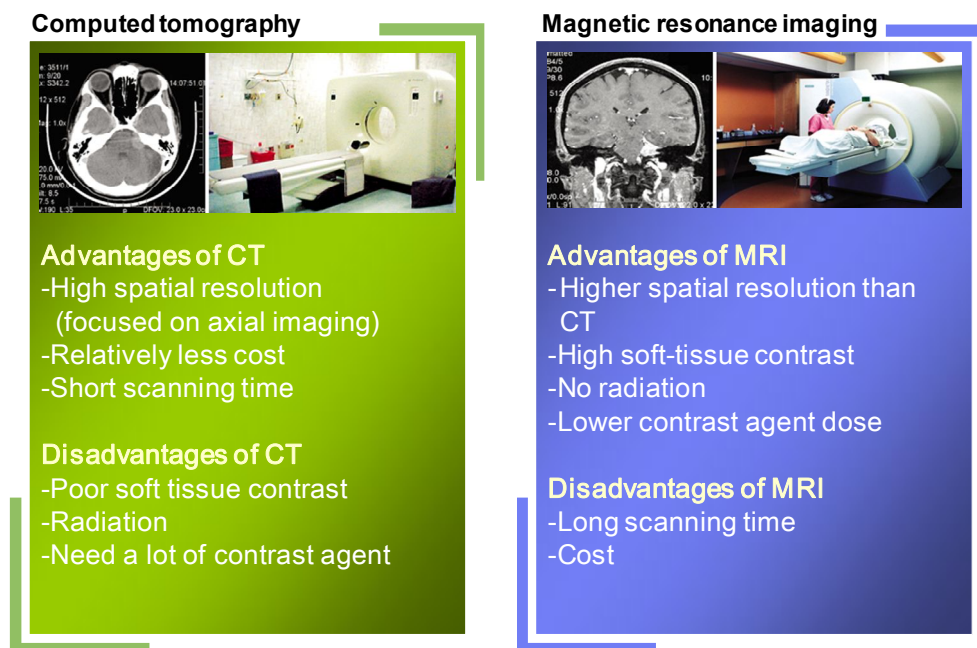


**Figure 1-7.** Comparison of computed tomography and magnetic resonance imaging.

### 1.6. Research objectives

During the last decade, nanoparticles have been used extensively for wide variety of biological and medical applications owing to their unique

properties originating from small size and structure. Many nanoparticles, including metallic, inorganic and organic nanoparticles, were studied for disease diagnosis and therapy. A number of techniques and materials are developed for diagnosis and therapy, respectively. Recently, multi-functional nanoparticles, which are combined imaging modalities and drug carriers, have been attracted much attention in terms of clinically effective disease treatment and a lot of researches are on progress. However, there are few achievements using multi-functional nanoparticles which show successful results in vivo. In this study, fabrication method of nanoparticle based imaging probes for MRI and optical imaging. MRI was selected as an anatomical imaging modality because it has advantages in terms of soft tissue contrast and toxicity problems compare to CT (Figure 1-7). After investigation of the imaging probes, drug delivery system based on polymeric micelles was studied and biomedical applications of the micelles were demonstrated. The last, we combined imaging modalities and drug carriers for efficient disease diagnosis and therapy using calcium phosphate coated nanoparticles.

In chapter 2, we investigated fluorescence quenching effect of iron oxide nanoparticles using silica coated iron oxide nanoparticles and

demonstrated potential as a contrast agent. Iron oxide based magnetic nanoparticles with controlled silica layer were used to reveal the relationship between quenching efficacy and distance from iron oxide.

Fabrication method and application of activatable dual imaging probe based on silica coated iron oxide were described in chapter 3. PEG decorated silica-iron oxide core shell nanoparticles were used for MRI contrast agent and Cy5.5 labeled MMP specific peptide were introduced on the surface of nanoparticles for activatable optical imaging.

In chapter 4, glycol chitosan coated iron oxide nanoparticles were studied for enhanced tumor targeting and activatable NIRF/MRI dual imaging probe. Because the probe which was developed in chapter 3 showed relatively low tumor selectivity, we introduced glycol chitosan as a coating material and glycol chitosan coated probe was showed enhanced tumor selectivity.

Polymeric micelles with ionic stabilization were introduced in chapter 5 and 6 for efficient drug delivery. Micelle is concentration-dependent self assembled structure and easily dissociated under critical micelle concentration. Micelle based drug carrier limited in vivo application due to its stability problem. In these chapters, micelles were stabilized by calcium

cation and doxorubicin, positively charged drug, via electrostatic interaction and potential as a drug carrier was revealed.

Theranostic nanoparticles based on imaging nanoparticles with calcium phosphate layer were investigated in chapter 7 and 8. Gold nanoparticle (chapter 7) and iron oxide nanoparticles (chapter 8) were used for providing imaging modality and calcium phosphate, well known biocompatible and pH sensitive material, was deposited. In these chapters, we described fabrication method and potential as an in vivo theragnostic nanoparticle were described.

## 1.7. References

- [1] C. Fang, M. Zhang, *J. Control. Release* **2010**, *146*, 2.
- [2] K. Kim, J. H. Kim, H. Park, Y.-S. Kim, K. Park, H. Nam, S. Lee, J. H. Park, R.-W. Park, I.-S. Kim, K. Cho, S. Y. Kim, K. Park, I. C. Kwon, , *J. Control. Release*,**2010**, *146*, 219.
- [3] R. Weissleder, M.J. Pittet, *Nature* **2008**, *452*, 580.
- [4] A. Nel, L. Mädler, D. Velegol, T. Xia, E. Hoek, P. Somasundaran, F. Klaessig, V. Castranova, M. Thompson, *Nat. Mater.* **2009**, *8*, 543.
- [4] D. Majumdar, X.H. Peng, D.M. Shin, *Curr. Top. Med. Chem.* **2010**, *10*,

1211.

- [6] P. Debbage, W. Jaschke, *Histochem. Cell Biol.* **2008**, *130*, 845.
- [7] J. Folkman, *Nat. Med.* **1995**, *1*, 27.
- [8] S. Skinner, *Cancer Res.* **1990**, *50*, 2411.
- [9] M. Suzuki, K. Hori, I. Abe, S. Saito and H. Sato, *J.Natl.Cancer Inst.* **1981**, *67*,663.
- [10] H. Maeda and Y. Matsumura, *Crit. Rev. Ther. Drug Carrier Syst.* **1989**, *6*, 193.
- [11] K. Iwai, H. Maeda and T. Konno, *Cancer Res.* **1984**, *44*, 2115.
- [12] Y. Matsumura and H. Maeda, *Cancer Res.* **1986**, *46*, 6387.
- [13] E. L. Ritman, *Annu. Rev. Biomed. Eng.* **2004**, *6*, 185.
- [14] B. J. Salmeron and E. A. Stein, *Psychopharmacol. Bull.* **2002**, *36*, 102.
- [15] P. Schweinhardt, C. Bountra and I. Tracey, *NMR Biomed.* **2006**, *19*, 702.
- [16] A. M. Oros and N. J. Shah, *Phys. Med. Biol.* **2004**, *49*, R105.
- [17] M. O. Leach, *Phys. Med. Biol.* **2006**, *51*, R61.
- [18] M. Rudin, R. Weissleder, *Nat. Rev. Drug Discov.* **2003**, *2*, 123.
- [19] L. E. Jennings, N. J. Long, *Chem. Commun.* **2009**, *28*, 3511.
- [20] L. Zhang, B. Liu, S. Dong, *J. Phys. Chem. B* **2007**, *111*, 10448.

- [21] M. Ogawa, C. A. Regino, J. Seidel, M. V. Green, W. Xi, M. Williams, N. Kosaka, P. L. Choyke, H. Kobayashi, *Bioconjugate Chem.* **2009**, *20*, 2177.
- [22] S. K. Mandal, N. Lequeux, B. Rotenberg, M. Tramier, J. Fattaccioli, J. Bibette, B. Dubertret, *Langmuir* **2005**, *21*, 4175.
- [23] Z. Medarova, W. Pham, Y. Kim, G. Dai, A. Moore, *Int. J. Cancer* **2006**, *118*, 2796.
- [24] S. Aime, M. Botta, M. Fasano, E. Terreno, *Chem. Soc. Rev.* **1998**, *27*, 19.
- [25] M. Mulder, A. W. Griffioen, G. J. Strijkers, D. P. Cormode, K. Nicolay, Z. A. Fayad, *Nanomedicine* **2007**, *2*, 307.
- [26] E. A. Schellenberger, D. Sosnovik, R. Weissleder, L. Josephson, *Bioconjugate Chem.* **2004**, *15*, 1062.
- [27] T. R. Sathe, A. Agrawal, S. Nie., *Anal. Chem.* **2006**, *78*, 5627.
- [28] L. Josephson, M. F. Kircher, U. Mahmood, Y. Tang, R. Weissleder, *Bioconjugate Chem.* **2002**, *13*, 554.
- [29] K. Chen, J. Xie, H. Xu, D. Behera, M. H. Michalski, S. Biswal, A. Wang, X. Chen, *Biomaterials* **2009**, *30*, 6912.
- [30] C. Wong, T. Stylianopoulos, J. Cui, J. Martin, V. P. Chauhan, W. Jiang,

- Z. Popovic, R. K. Jain, M. G. Bawendi, D. Fukumura, *Proc. Natl. Acad. Sci.* **2011**, *108*, 2426.
- [31] J. Xie, K. Chen, J. Huang, S. Lee, J. Wang, J. Gao, X. Li, X. Chen., *Biomaterials* **2010**, *31*, 3016.
- [32] T. Nam, S. Park, S. Y. Lee, K. Park, K. Choi, I. C. Song, M. H. Han, J. J. Leary, S. A. Yuk, I. C. Kwon, K. Kim, S. Y. Jeong, *Bioconjugate Chem.* **2010**, *21*, 578.
- [33] X. Yang, H. Hong, J. J. Grailer, I. J. Rowland, A. Javadi, S. A. Hurley, Y. Xiao, Y. Yang, Y. Zhang, R. J. Nickles, W. Cai, D. A. Steeber, and S. Gong, *Biomaterials* **2011**, *32*, 4151.
- [33] H. Y. Lee, Z. Li, K. Chen, A. R. Hsu, C. Xu, J. Xie, S. Sun, and X. Chen, *J. Nucl. Med.* **2008**, *49*, 1371.
- [34] G. Antoch, F. M. Vogt, L. S. Freudenberg, F. Nazaradeh, S. C. Goehde, J. Barkhausen, G. Dahmen, A. Bockisch, J. F. Debatin, and S. G. Ruehm, *J. Am. Med. Assoc.* **2003**, *290*, 3199.
- [35] C. Bremer, S. Bredow, U. Mahmood, R. Weissleder, and C.-H. Tung, *Radiology* **2001**, *221*, 523.
- [36] E. E. Connor, J. Mwamuka, A. Gole, C. J. Murphy, M. D. Wyatt, *Small* **2005**, *1*, 325.

- [37] B. Dubertret, M. Calame, A. J. Libchaber, *Nat. Biotechnol.* **2001**, *19*, 365.
- [38] C. S. Yun, A. Javier, T. Jennings, M. Fisher, S. Hira, S. Peterson, B. Hopkins, N. O. Reich, G. F. Strouse, *J. Am. Chem. Soc.* **2005**, *127*, 3115.
- [39] N. L. Rosi, D. A. Giljohann, C. S. Thaxton, A. K. Lytton-Jean, M. S. Han, C. A. Mirkin, *Science* **2006**, *312*, 1027.
- [40] I.-C. Sun, D.-K. Eun, H. Koo, C.-Y. Ko, H.-S. Kim, D. K. Yi, K. Choi, I. C. Kwon, K. Kim, and C.-H Ahn, *Angew. Chem. Int. Ed.* **2011**, *50*, 9348.

## **Chapter 2.**

**Distance-dependent fluorescence quenching of  
fluorophore labeled iron oxide core-shell  
nanoparticles with high T2 relaxivity**

## **2.1. Introduction**

Magnetic resonance imaging (MRI) and optical imaging are two highly complementary techniques <sup>[1-3]</sup>, one providing anatomical details and the other providing functional and molecular information. MRI excels at representing anatomy, but has limited ability in measuring gene expression or depicting specific targets. On the other hand, optical imaging can detect molecular activity using different fluorescent probes, but the technique lacks anatomical information. Moreover, since the fluorescent probes used in optical imaging are often conjugated to larger particles for size-specific targeting, it is not always clear whether the resulting image is generated by the whole intact nanoparticle or the reporting moiety that has floated off due to cleavage from the core particle. Therefore, the combination of two modalities complements the weaknesses present in each system and provides clinicians with a definitive tool for identification and characterization of specific targets in living subjects' anatomical context.

Optical imaging, in most applications, requires contrast agents that differentiate the target tissue/cell types from the surrounding environment. This is usually achieved by the use of fluorescent probes that accumulate preferentially at the target site (e.g. through enhanced permeability and

retention (EPR) effect in targeting tumor cells) or that become fluorescent near the target. MRI also benefits from the use of contrast agents due to its inherent low sensitivity in detecting pathological tissues <sup>[4]</sup>. In fact, about 35% of clinical MRI scans use contrast agents <sup>[5]</sup>. Therefore, development of a contrast agent that works for both MRI and optical imaging is not only useful but also imperative for MRI/optical multimodal imaging diagnosis.

Of the materials tested for MRI contrasting purpose, gadolinium and iron oxide have been most widely used <sup>[6-10]</sup>. Gadolinium is paramagnetic and generates a positive contrast, while iron oxide is superparamagnetic and produces a negative contrast <sup>[11]</sup>. Although several systems using gadolinium have been successful, iron oxide nanoparticle is a better material in terms of higher relaxivity and longer circulation time in vivo <sup>[12, 13]</sup>. Because of these advantages, a number of iron oxide-based contrast agents have been studied, and researchers are trying to develop MRI probes with higher relaxivity for efficient visualization of disease based on MRI <sup>[10, 14-18]</sup>.

In the course of developing multimodal contrast agents based on iron oxide nanoparticles, researchers have reported that iron oxide has the ability to quench fluorescence <sup>[12, 19-23]</sup>. Weissleder et al. reported fluorescence quenching by iron oxide and fabricated magnetic nanoparticle based MRI

contrast agents that have enzyme triggered near-infrared fluorescence (NIRF) imaging modality <sup>[12]</sup>. Zhang et al. has demonstrated fabrication method for bifunctional magnetic nanoparticle using silica shell to prevent fluorescence quenching by iron oxide core <sup>[22]</sup>. However, in spite of much research on iron oxide nanoparticles, the mechanism behind fluorescence quenching by iron oxide has not been clearly elucidated.

There are several hypotheses to explain fluorescence quenching by iron oxide, among which are 1) electron coupling effect between iron oxide and the fluorescent dye and 2) broad absorption by iron oxide <sup>[22]</sup>. The first mechanism is through which gold nanoparticles quench fluorescence <sup>[19]</sup>; some researchers have assumed that iron oxide quenches fluorescence through the same mechanism <sup>[23]</sup>. However, Nie et al. has demonstrated that fluorescence quenching could be still observed in dilute solutions of iron oxide and quantum dot, in which iron oxide and the dye are not in direct contact <sup>[21]</sup>, thereby suggesting that iron oxide quenches fluorescence through a different mechanism rather than energy transfer through electron coupling.

Although fluorescence quenching by iron oxide is a useful property that can be exploited to develop efficient multimodal contrast agents and

despite the fact that the phenomenon has been reported in many studies, no study on distance-dependent fluorescence quenching by iron oxide has been reported. In this study, we demonstrate the distance-dependent fluorescence quenching by iron oxide core-shell (CS) nanoparticle through careful control of the distance between the iron oxide core and the fluorescent dye, which is accomplished by varying the silica shell width.

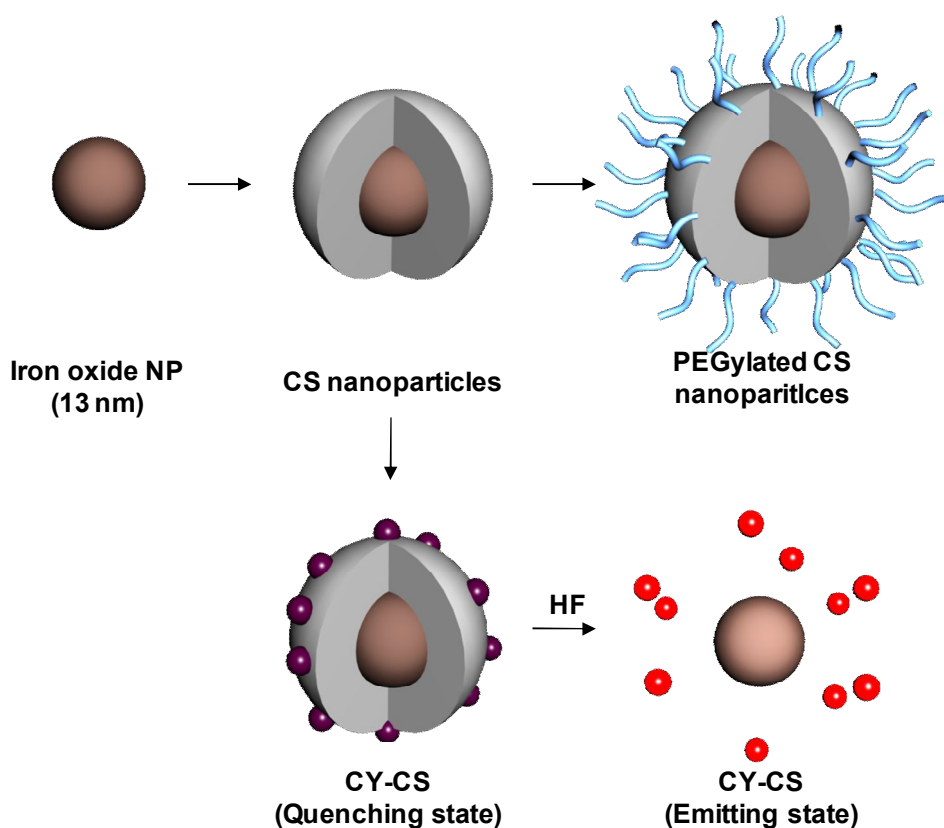


**Figure 2-1.** Schematic diagram of core-shell nanoparticle formation.

## 2.2. Experimental

**Preparation of silica coated iron oxide nanoparticles.** To study the quenching property of iron oxide, we fabricated Cy5.5-conjugated FeO<sub>x</sub>@SiO<sub>2</sub> nanoparticles (Figure 2-1). First, silica was coated onto the surface of the hydrophobic Fe<sub>3</sub>O<sub>4</sub> nanoparticles with oleic acid ligand, which was accomplished by the modified reverse microemulsion procedure<sup>[9]</sup>. Briefly, different volume of (10, 20, 60, and 300 μL) the FeO<sub>x</sub> nanoparticles (10 mg Fe/mL) with 13 nm diameter were each dispersed into 60 mL of cyclohexane, respectively. Triton-X 100 (1.12 mL), 1-octanol (400 μL), tetraethyl orthosilicate (TEOS, 200 μL), and NH<sub>4</sub>OH (152.8 μL) were added into each of the Fe<sub>3</sub>O<sub>4</sub> nanoparticles dispersed in cyclohexane solution. The reaction mixture was continuously stirred for 3 days at 600 rpm. The final product was then dispersed into 60 mL of anhydrous EtOH after washing with EtOH through centrifugation at 20000 rpm for 30 min. Silica thickness, which was controlled from 4.6 to 42 nm by increasing the concentration of the Fe<sub>3</sub>O<sub>4</sub> nanoparticles from 10 to 300 μL, was confirmed by transmission electron microscopy (TEM). The codes for each sample were CS20 (20.2 nm, 300 μL Fe<sub>3</sub>O<sub>4</sub>), CS33 (32.6 nm, 60 μL Fe<sub>3</sub>O<sub>4</sub>), CS60 (59.2 nm, 60 μL Fe<sub>3</sub>O<sub>4</sub>), and CS113 (113.8 nm, 10 μL Fe<sub>3</sub>O<sub>4</sub>). The codes

were assigned according to the target particle diameters. The final concentration of nanoparticles was determined as 45.8 (CS113), 44.8 (CS60), 51.0 (CS33), and 56.3  $\mu\text{g Fe per mL}$  (CS20) by inductively coupled plasma mass spectrometry (ICP-MS) analysis and the  $\zeta$ -potential were carried out using ELS-Z system (Otsuka electronics Co. Ltd., Osaka, Japan) equipped with He-Ne laser at a wavelength of 630 nm.

**Cy conjugation on the surface of nanoparticles.** After the silica coating, (3-aminopropyl) triethoxysilane (APTES, 1.0 mL) was added to 10.0 mL of the CS nanoparticles to introduce amine groups on the surface of nanoparticles for fluorescent dye conjugation. The reaction was carried out for 12 h, with vigorous stirring at room temperature. Unreacted APTES was removed by 5 times centrifugation with absolute ethanol, and the mixture was redispersed in deionized water after washing.

Fluorescence modality was conferred to the nanoparticles by conjugating the fluorescent dye, Cy5.5 mono acid, on the surface of the nanoparticles. Cy 5.5 mono acid (0.1 mg) and 1.0 mg EDC/NHS were dissolved in 1.0 mL of deionized water, and the resulting solution was added to the 5.0 mL of APTES-capped CS nanoparticles. The reaction was carried

out in darkness for 12 h with vigorous stirring. The final product was dispersed into 5.0 mL of deionized water after washing with distilled water through 5 times centrifugation at 13000 rpm to remove unreacted reactants. The codes for final products were CY-CS20, CY-CS33, CY- CS60, and CY-CS113.

**Fluorescence quenching study.** For fluorescence quenching studies, fluorescence of untreated CY-CS20, CY-CS30, CY-CS50, and CY-CS100 which are Cy5.5 conjugated CS nanoparticles were measured. Then, each CY-CS nanoparticles (5.0 mL aliquot) was mixed with 5.0 mL of HF in 50 mL PTFE beaker and the reaction mixtures were stirred for 3 h to decompose silica shell. Residual HF and byproducts were removed by 3 times evaporation with 60.0 mL of distilled water at 160 °C. After evaporation, nanoparticles and free Cy5.5 were dissolved in 5.0 mL of deionized water and fluorescence of the solution was measured. Fluorescence of nanoparticles was measured by using a Shimadzu spectrophotometer and Kodak imaging station system (Kodak, New Haven, CT) with 4000MM charge coupled device (CCD) camera and Cy5.5 emission filter.

**Magnetic resonance imaging study.** For magnetic resonance imaging study, surface of CS nanoparticles were decorated by PEGs to enhance water stability (Figure 2-1). Briefly, APTES (0.5 mL) was added to 5.0 mL of CS nanoparticles to introduce amine groups on the surface of nanoparticles for PEG conjugation. Then, amine capped CS nanoparticles in ethanol were centrifuged at 14500 rpm for 30 min and re-dispersed 3 times in 5.0 mL of anhydrous ethanol to remove unreacted APTES and finally re-dispersed in deionized water. After the solvent exchange, mPEG (1.0 mg) activated by NHS was added into the amine capped CS nanoparticles and the solution was stirred vigorously at room temperature. After 3 h stirring, PEGylated CS nanoparticles were centrifuged 3 times with deionized water at 14500 rpm for 30 min and re-dispersed in 5.0 mL of deionized water for the further experiments.

Magnetic resonance imaging studies were carried by using a MRI scanner at 3T field strength. Transverse relaxation time ( $T_2$ ) of each nanoparticle sample was obtained at RT and 60 Hz, and the  $T_2$  relaxivity of each sample was calculated by fitting the  $1/T_2$  ( $r_2$ ) values versus iron contents of CS nanoparticle samples according to the equation of  $1/T_2 = A$   $[Fe]$ , where  $T_2$  is the transverse relaxation time at a given iron concentration

([Fe]) and A is the relaxivity of nanoparticle sample.

**Cell viability.** In vitro cytotoxicity of CS nanoparticles was evaluated using MTT assay. 5000 HeLa cells were grown in each well of 96-well plates in 0.2 mL of DMEM medium with 10 % FBS. Then, cells were washed with pre-warmed PBS and incubated with pre-warmed DMEM medium for 30 min before the addition of non-PEGylated and PEGylated CS nanoparticles. Cells were incubated for 4 h at 37 °C with nanoparticle dispersed DMEM medium and medium was replaced by a fresh DMEM medium. The control cells were incubated without nanoparticles. After incubation, MTT solution (1 mg/mL, 0.1 mL) was added to each well and cells were incubated for additional 4 h. Then, formazan crystal was dissolved in 0.2 mL of DMSO and fluorescence of solution was measured at 570 nm using a micro-plate reader.

**In vivo imaging.** For in vivo visualization of CS nanoparticles, SCC7 cells cultured in RPMI 1640 medium with 10 % FBS were inoculated into the back of BALB/C nude mouse by subcutaneous injection. When tumor had grown up, Cy-CS20 and Cy-CS113 (0.3 mL, 0.15 Fe mg/mL) was

injected intratumorally and images were obtained by two different imaging modalities, magnetic resonance image and NIRF tomographic image. Magnetic resonance images were obtained using a MRI scanner at 3.0-T field strength (Tim Trio; Siemens, Erlangen, Germany). Mice were placed on the tray of the MRI scanner and imaged before/after injection. T2-weighted MR images were obtained by a multi-spin echo multi-slice imaging sequence with following parameters: TR=51 ms, TE=20 ms and slice thickness of 0.6 mm. NIRF tomographic images were obtained with an eXplore Optix system (ART Advanced Research Technologies Inc., Montreal, Canada). The fluorescence in SCC7 tumor-bearing mice were imaged by mice on the animal plate in the eXplore Optix system. Laser power and integration time were 10  $\mu$ W and 0.3 s, respectively. A 670 nm laser was applied to excite Cy5.5 fluorescence dyes and 700 nm emission filters was applied to collect fluorescence emission of Cy5.5. After NIRF imaging, mice were sacrificed and the NIRF images of excised tumor was obtained using a Kodak Image Station 4000MM Digital Imaging System.

### **2.3. Results and discussion**

To study the effect of distance between iron oxide and the dye on the

fluorescence, four samples with varying diameters were made by the above procedure. Diameters of CS nanoparticles were 20.2 (CS20), 32.6 (CS33), 59.2 (CS60), and 113.8 nm (CS113) (Table 2-1). The  $\zeta$ -potential values of the samples were -3.3, -5.3, -16.2, and -29.3 mV, respectively. The negative  $\zeta$ -potential values indicate that silica is successfully coated on the surface of Fe<sub>3</sub>O<sub>4</sub> nanoparticles. Each sample was relatively mono-dispersed, as demonstrated by TEM images (Figure 2-2). TEM images also show uniform spherical core-shell structure with single iron oxide nanoparticle core and the silica shell with controlled thickness.

**Table 2-1.** Sample codes, diameters and  $\zeta$ -potential of each sample.

Sample code <sup>[a]</sup>	$d_{\text{TEM}}$ (nm)	$d_{\text{DLS}}$ (nm)	$\zeta$ -potential (mV)
CS20	19.3	20.2	-3.32
CS33	31.4	32.6	-5.31
CS60	55.1	59.2	-16.10
CS113	97.1	113.2	-29.32

[a] Sample codes are named based on diameters by DLS measurement

Fluorescence spectra of the Cy5.5 conjugated CS nanoparticles, CY-CS, were measured to study the effect of distance on quenching efficiency by iron oxide core. Excitation wavelength of 676 nm and emission wavelength of 692 nm were used for measurement. Fluorescence of

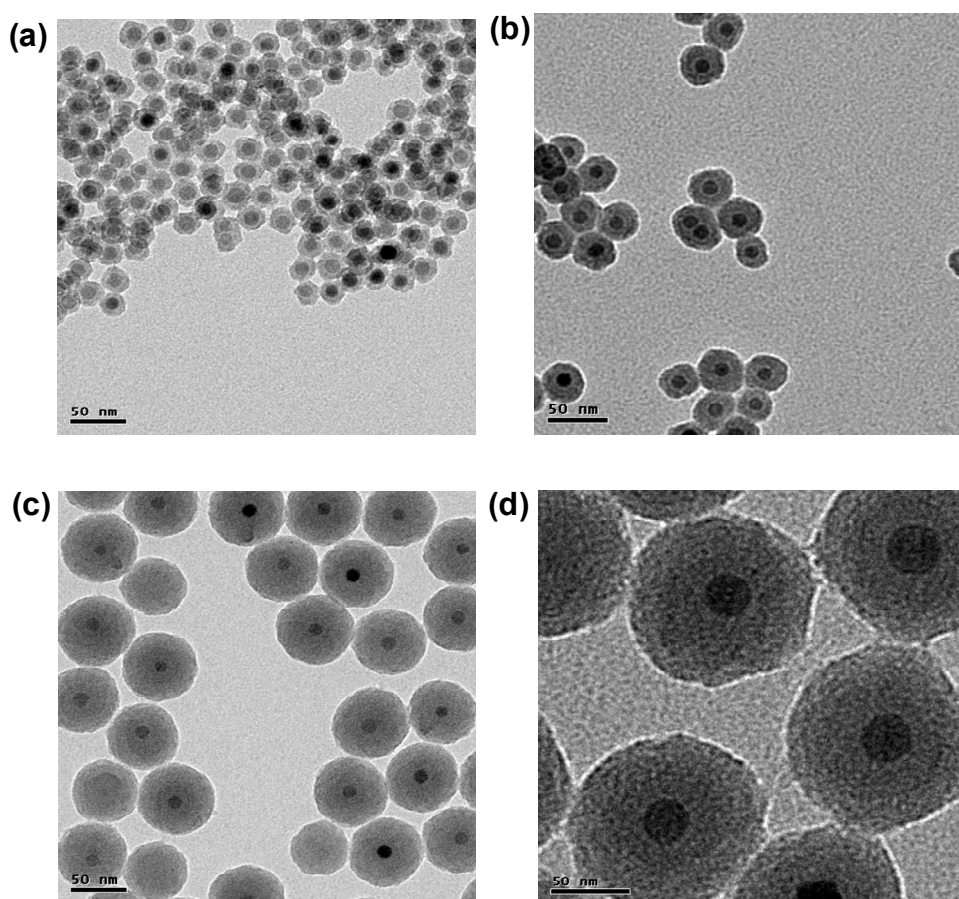


**Figure 2-2.** TEM images of CS nanoparticles. (a) CS20, (b) CS33, (c) CS60, and (d) CS113 (scale bar: 50 nm).

untreated CY-CS20, CY-CS33, CY-CS60, and CY-CS113 were measured (Figure 2-3a). Then the samples were treated with HF to decompose silica shell and to measure the full fluorescence of free Cy5.5 from the iron oxide core, because the fluorescence intensity of Cy5.5 was not affected during the shell-dissolving process by the presence of HF (Figure 2-3b). The average number of Cy5.5 molecules on each particle was calculated using surface area of nanoparticles, the number of nanoparticles and Cy5.5 in nanoparticle solution. The fluorescence was significantly decreased in CY-CS20, and the fluorescence gradually recovered with increase in the silica shell width. Fluorescence levels of HF treated samples have similar values.

Fluorescence was fully quenched in CY-CS20 and strong fluorescence signal was shown in CY-CS113. Fluorescence level was almost similar with  $10^{-5}$  M Cy5.5 solution, same concentration of Cy5.5 on the CY-CS113. The results clearly indicate that the iron oxide significantly reduces the Cy5.5 fluorescence intensity and the fluorescence quenching property of iron oxide was influenced by distance between Cy5.5 and iron oxide.

Quenching efficiency and average distance between each Cy5.5 dyes were calculated for each sample (Table 2-2). The fluorescence of each sample was measured 3 times and averaged values were used for calculation

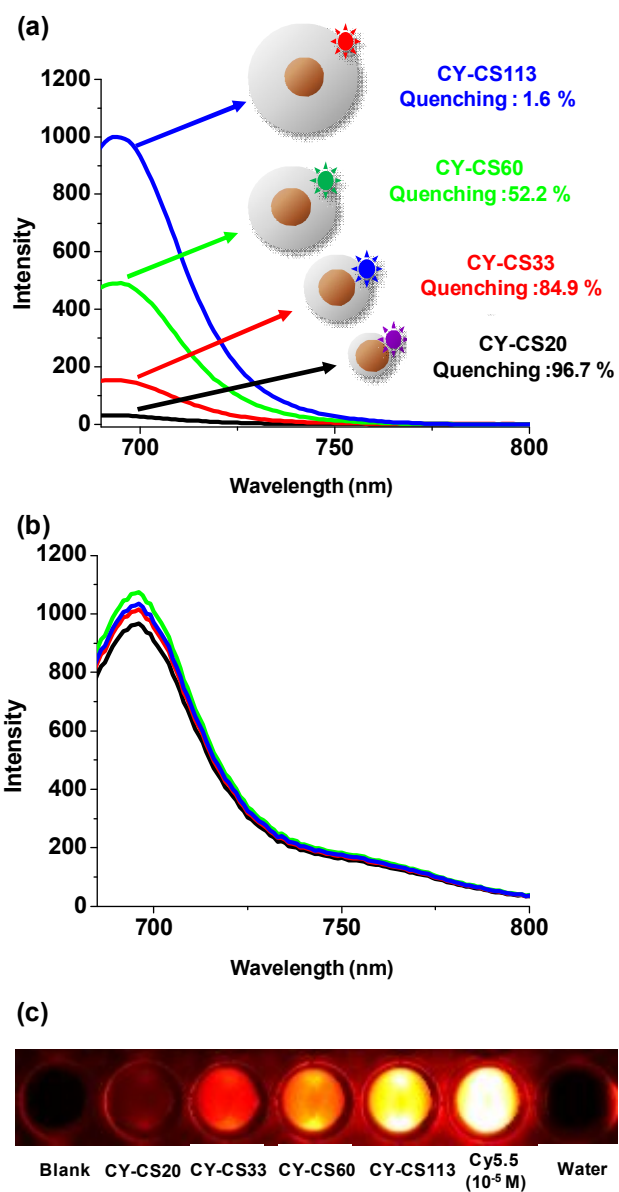


**Figure 2-3.** Fluorescence spectra of CY-CS nanoparticles. (a) Before HF treatment. (b) After HF treatment. (c) NIRF image of CY-CS nanoparticles.

of quenching efficiency. Quenching efficiency was near 100 % in CY-CS20 while near 0 % in CY-CS113. The quenching efficiency was gradually decreased with corresponding thickness of silica shell and this result shows that fluorescence quenching is distance-dependent, and the quenching behavior can be controlled by changing the thickness of silica shell. The possibility of Cy5.5 self-quenching as a fluorescence quenching mechanism can be ruled out from the calculation of average distance between Cy5.5 in each sample, since they are smaller than maximum Förster radius in Cy5.5 molecules, which is around 10 nm<sup>[24]</sup>.

**Table 2-2.** Fluorescence intensity of CY-CS nanoparticles with/without HF treatment, number of Cy5.5 on a particle and quenching efficiency.

Sample	Fluorescence intensity of CY-CS <sup>[a]</sup>		Cy5.5 / particle	Quenching efficiency (%)
	Intact	HF treated		
CY-CS20	31.1	942.1	6.22	96.7
CY-CS33	153.3	988.2	7.59	84.9
CY-CS60	486.7	1046.6	17.86	52.2
CY-CS113	993.2	1007.4	42.46	1.6

[a] PL measurement at 692 nm

Transverse relaxation time was measured using MRI scanner at 3 T magnetic field strength to evaluate the use of CS nanoparticles as MRI contrast agents. Because larger CS nanoparticles (CS60 and CS113) showed poor water stability during MRI scan, CS nanoparticles were PEGylated for enhanced stability. Diameters of PEGylated CS nanoparticles were 26.5 (from CS20), 41.2 (from CS33), 68.1 (from CS60), and 134.4 nm (from CS113) by DLS measurements. Transverse relaxivity ( $r_2$ ) value was 4485.8  $\text{mM}^{-1}\text{s}^{-1}$  in PEGylated CS20, 2149.5  $\text{mM}^{-1}\text{s}^{-1}$  in PEGylated CS33, 359  $\text{mM}^{-1}\text{s}^{-1}$  in PEGylated CS60 and 1479.6  $\text{mM}^{-1}\text{s}^{-1}$  in PEGylated CS113 (Figure 2-4). The  $r_2$  value gradually decreased with increase in silica shell thickness [25]. However, in spite of increase of silica coating thickness, CS113 showed higher relaxivity than CS60 in this study because of the structural difference of CS113. CS113 has larger iron oxide core, about 20 nm than the other CS nanoparticles (Figure 2-2d). Several iron oxide nanoparticles were assembled in silica coating condition of CS113 and the assembly of iron oxide has contributed to higher relaxivity. These  $r_2$  values of PEGylated CS nanoparticles were higher than  $r_2$  value of Feridex (162.2  $\text{mM}^{-1}\text{s}^{-1}$ ), commercially available iron oxide based MRI contrast agent. Especially,  $r_2$  value of PEGylated CS20 was over 20 times higher than Feridex. The  $r_2$

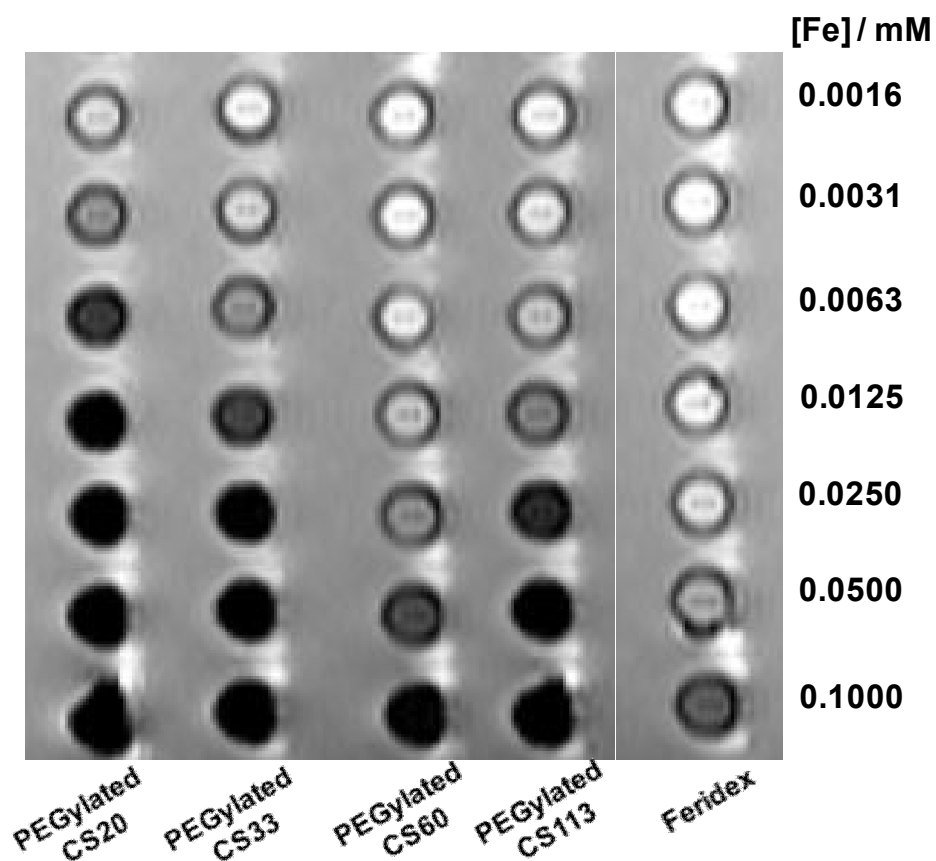


**Figure 2-4.** T2-weighted MR images of PEGylated CS nanoparticles and Feridex.

value of iron oxide nanoparticles, which was used for synthesis of CS nanoparticles, was used as a positive control. The iron oxide nanoparticles were PEGylated because of their poor water stability. The r2 value of

PEGylated iron oxide nanoparticles was similar as CS20 nanoparticles, indicating that high  $r_2$  values of CS nanoparticles were due to magnetic property of the iron oxide core. The reason of high relaxivity is  $Zn^{2+}$  dopant effect of iron oxide nanoparticles.  $Zn^{2+}$  doped iron oxide nanoparticles were used in this study for preparing core-shell nanoparticles and  $Zn^{2+}$  contents was 5 wt% against iron content. According to the previously reported research, the magnetism of the  $Zn^{2+}$  doped iron oxide nanoparticles was gradually increases as the  $Zn^{2+}$  doping level in the range of 0 to 13.3 wt% and  $M_s$  values directly related to the contrast enhancement effects in MRI [26]. Specially, T2 relaxivity represents the degree of T2-weighted MRI contrast effect where the  $r_2$  value is roughly proportional to the square of the  $M_s$  value [27]. Considering these studies, high relaxivity values of nanoparticles are reasonable and high  $M_s$  values of these nanoparticles can be used to accomplish magnetism induced heat generation for hyperthermic treatment and obtain in vivo magnetic resonance images with enhanced resolution.

In vitro cytotoxicity of CS nanoparticles was evaluated by the MTT assay. HeLa cell viabilities after treating with non-PEGylated (Figure 2-5a) or PEGylated CS nanoparticles (Figure 2-5b) decreased as a function of

nanoparticle concentrations. Viability of CS nanoparticle-treated cells decreased from 86.3 % to 40.1 % as nanoparticle concentration increased. PEGylated CS nanoparticle-treated cells showed higher viability than CS nanoparticle-treated cells and values were between 98.7 % and 51.2 %. These results show that surface modification of iron oxide nanoparticles, using silica and PEG, reduces cytotoxicity. Especially, PEGylated iron oxide nanoparticles showed near 90 % cell viability at the concentration of 0.15 Fe mg/mL. In a number of animal studies using nude mice, 0.03~0.05 mL iron oxide nanoparticles (0.1~0.3 Fe mg/mL, 0.25~0.75 Fe mg/kg) were used. Moreover, 0.56 mg Fe/kg (diluted in 100 mL of 5% dextrose) of Feridex has been used in clinic <sup>[28-29]</sup>. Considering these studies, the PEGylated CS nanoparticles showed low toxicity at the concentration for in vivo study and clinical use, and the results demonstrate that these nanoparticles can be excellent candidate for in vivo applications. In vivo imaging of subcutaneous SCC7 xenografted mice was performed using two different imaging modalities, magnetic resonance imaging and NIRF tomographic imaging. CY-CS20 and CY-CS113 were intratumorally injected and nanoparticles were imaged by Tim Trio MRI scanning system (Siemens, Erlangen, Germany). As shown in Figure 2-5a, tumor was significantly dark

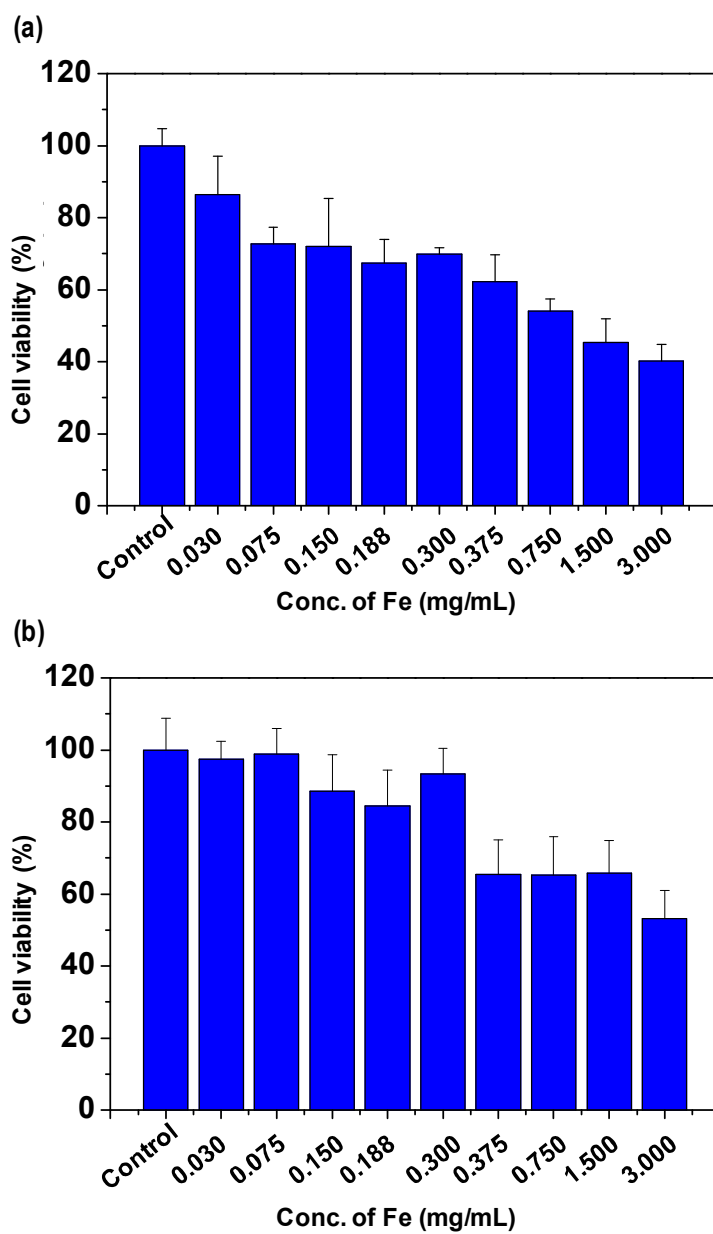
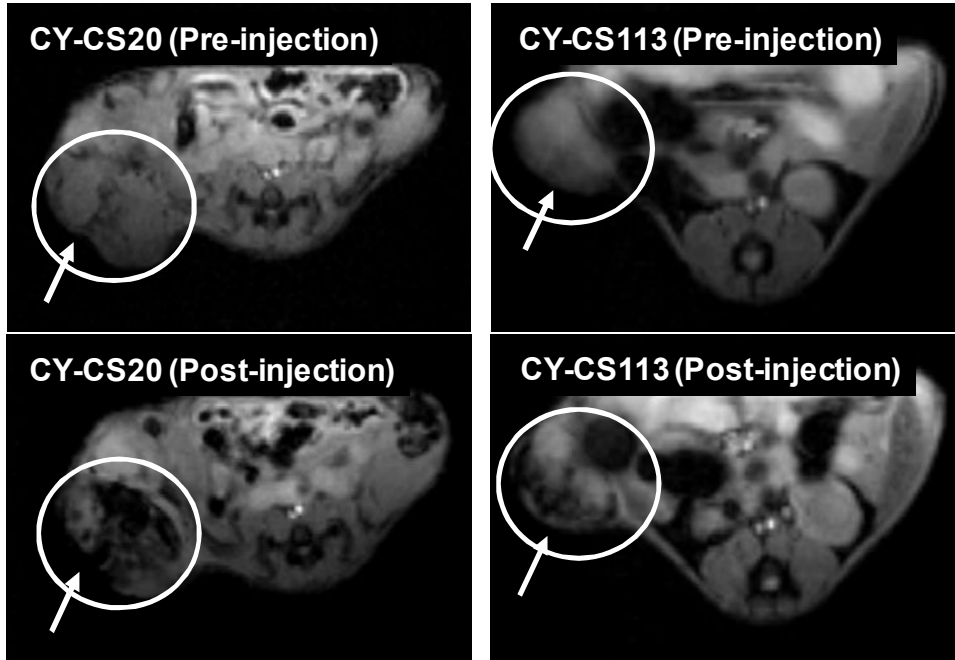


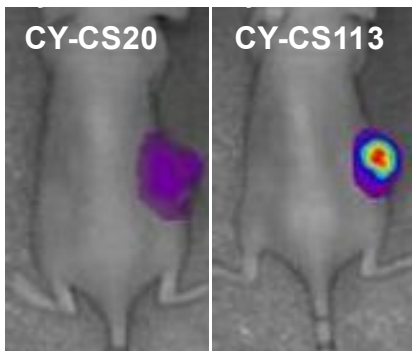
Figure 2-5. Cell viability of (a) CS20 and (b) PEGylated CS20.

ened after nanoparticle injection because of superparamagnetic iron oxide core and the relative signal enhancements were  $41.5 \pm 6.69$  % (CY-CS20) and  $31.2 \pm 3.77$  % (CY-CS113), respectively. The relative signal enhancement of the ROI in the T2-weighted image was obtained by the comparison between the tumor and the healthy muscle. As shown in Figure 2-6a, dark and bright region were mixed in the tumor site because injected nanoparticles does not fully diffuse to whole tumor region. Intratumorally injected nanoparticles remain generally in the extracellular space and the extracellular matrix prevents diffusion of nanoparticles. For these reason, nanoparticle injected region became dark and other region remains bright. After MRI scanning, NIRF tomographic image was evaluated by eXplore Optix system (ART, Montreal, Canada) with NIRF probe detection system setting (excitation and emission at 670 nm and 700 nm, respectively). As shown in Figure 2-6b, weak fluorescence signal was detected in CY-CS20 injected tumor-bearing mouse. On the other hand, CY-CS113 produced strong fluorescence signals in tumor site. These differences of signal intensity were due to the fluorescence quenching properties of iron oxide core. Because of distance between Cy5.5 and iron oxide in CY-CS113 is far enough to avoid fluorescence quenching, CY-CS113 injected tumor site

(a)



(b)



(c)

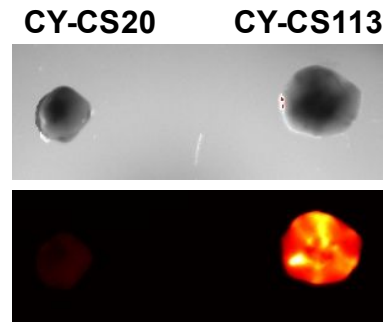


**Figure 2-6.** In vivo (a) MR, (b) NIRF images and (c) NIRF images of excised tumor with CY-CS20 and CY-CS113.

shows strong NIRF signal. Furthermore, self quenching of Cy5.5 by FRET was not observed in CY-CS113 injected tumor site due to low concentration of injected nanoparticle solution, enough to prevent FRET quenching. Figure 2-6c depicts NIRF images of excised tumors with CY-CS20 and CY-CS113. CY-CS113 injected tumor produced strong fluorescence signal and CY-CS20 administered tumor showed weak fluorescence signal, which was in a good agreement with in vivo imaging results. NIRF signal in tumor did not uniform because of poor diffusion of nanoparticles in extracellular space.

#### **2.4. Conclusion**

The current study has investigated for the first time the distance-dependent fluorescence quenching of Cy5.5 by iron oxide in CS nanoparticles, and the effectiveness of the prepared nanoparticles as a MRI contrast agent in terms of relaxivity and cytotoxicity. Furthermore, fluorophore conjugated CS nanoparticles produce a good T2-weighted magnetic resonance images and fluorescence quenching effect was successfully imaged in vivo. This finding may prove useful in developing multimodal imaging contrast agents that utilizes distance-dependent quenching behavior, for example, a contrast agent that can be triggered to

release fluorescent probe in response to an environmental stimuli. At the same time, the exact fluorescence quenching mechanism by iron oxide remains to be elucidated. Discovery of the mechanism will help researchers fully utilize iron oxide as a material for construction multimodal imaging contrast systems, and it will also give insight into development of other imaging contrast agents.

On the other hand, the high relaxivity and biocompatibility of the CS nanoparticle highlight its great potential as an effective multimodal imaging contrast agent. Since the fluorescence quenching efficiency and relaxivity both depend on the particle size, optimization of parameters, such as size and distance, will further improve the system.

## 2.5. References

- [1] M. Doubrovin, I. Serganova, P. Mayer-Kuckuk, V. Ponomarev, R. G. Blasberg, *Bioconjugate Chem.* **2004**, *15*, 1376.
- [2] L. E. Jennings, N. J. Long, *Chem. Commun.* **2009**, *28*, 351
- [3] M. Rudin, R. Weissleder, *Nat. Rev. Drug Discov.* **2003**, *2*, 123.
- [4] W. J. M. Mulder, A. W. Griffioen, G. J. Strijkers, D. P. Cormode, K. Nicolay, Z. A. Fayad, *Nanomedicine* **2007**, *2*, 307.

- [5] S. Aime, M. Botta, M. Fasano, E. Terreno, *Chem. Soc. Rev.* **1998**, *27*, 19.
- [6] Z. Cheng, D. L. J. Thorek, A. Tsourkas, *Angew. Chem. Int. Ed.* **2010**, *49*, 346.
- [7] E. J. Werner, A. Datta, C. J. Jocher, K. N. Raymond, *Angew. Chem. Int. Ed.* **2008**, *47*, 8568.
- [8] A. L. Nivorozhkin, A. F. Kolodziej, P. Caravan, M. T. Greenfield, R. B. Lauffer, T. J. McMurry, *Angew. Chem. Int. Ed.* **2001**, *40*, 2903.
- [9] S. Cheong, P. Ferguson, K. W. Feindel, I. F. Hermans, P. T. Callaghan, C. Meyer, A. Slocombe, C.-H. Su, F.-Y. Cheng, C.-S. Yeh, B. Ingham, M. F. Toney, R. D. Tilley, *Angew. Chem. Int. Ed.* **2011**, *50*, 4206.
- [10] J. Shin, R. M. Anisur, M. K. Ko, G. H. Im, J. H. Lee, I. S. Lee, *Angew. Chem. Int. Ed.* **2009**, *48*, 321.
- [11] W. J. Mulder, G. J. Strijkers, G. A. v. Tilborg, A. W. Griffioen, K. Nicolay, *NMR Biomed.* **2007**, *19*, 142.
- [12] L. Josephson, M. F. Kircher, U. Mahmood, Y. Tang, R. Weissleder, *Bioconjugate Chem.* **2002**, *13*, 554.
- [13] Y.-X. J. Wang, S. M. Hussain, G. P. Krestin, *Eur. Radiol.* **2001**, *11*, 2319.

- [14] J. Kim, H. S. Kim, N. Lee, T. Kim, H. Kim, T. Yu, I. C. Song, W. K. Moon, T. Hyeon, *Angew. Chem. Int. Ed.* **2008**, *47*, 8438.
- [15] M. K. Yu, Y. Y. Jeong, J. H. Park, S. J. Park, J. W. Kim, J. J. Min, K. W. Kim, S. Jon, *Angew. Chem. Int. Ed.* **2008**, *47*, 5362.
- [16] J. H. Choi, S. Lee, H. J. Kang, J. Y. Lee, J. Kim, H. O. Yoo, T. R. Stratton, B. M. Applegate, J. P. Youngblood, H. J. Kim, K. N. Ryu, *Macromol. Res.* **2010**, *18*, 504.
- [17] K. M. K. Selim, J.-H. Lee, S.-J. Kim, Z. Xing, I.-K. Kang, Y. Chang, H. Guo, *Macromol. Res.* **2006**, *14*, 646.
- [18] J. Kim, S. Park, J. E. Lee, S. M. Jin, J. H. Lee, I. S. Lee, I. Yang, J.-S. Kim, S. K. Kim, M.-H. Cho, T. Hyeon, *Angew. Chem. Int. Ed.* **2006**, *45*, 7754.
- [19] E. Dulkeith, A. C. Morteani, T. Niedereichholz, T. A. Klar, J. Feldmann, S. A. Levi, F. C. J. M. v. Veggel, D. N. Reinhoudt, M. M. ller, D. I. Gittins, *Phys. Rev. Lett.* **2002**, *89*, 2030.
- [20] S. K. Mandal, N. Lequeux, B. Rotenberg, M. Tramier, J. Fattaccioli, J. Bibette, B. Dubertret., *Langmuir* **2005**, *21*, 4175.
- [21] T. R. Sathe, A. Agrawal, S. Nie., *Anal. Chem.* **2006**, *78*, 5627
- [22] L. Zhang, B. Liu, S. Dong, *J. Phys. Chem. B* **2007**, *111*, 10448

- [23] D. Ma, J. Guan, F. Normandin, S. Denommee, G. Enright, T. Veres, B. Simard, *Chem. Mater.* **2006**, *18*, 1920.
- [24] F. Chen, W. Bu, Y. Chen, Y. Fan, Q. He, M. Zhu, X. Liu, L. Zhou, S. Zhang, W. Peng, J. Shi, *Chem. Asian J.* **2009**, *4*, 1809.
- [25] U. Schobel, H.-J. Egelhaaf, A. Brecht, D. Oelkrug, G. n. Gauglitz, *Bioconjugate Chem.* **1999**, *10*, 1107.
- [26] J.-T. Jang, H. Nah, J.-H. Lee, S. H. Moon, M. G. Kim, J. Cheon, *Angew. Chem. Int. Ed.* **2009**, *48*, 1234.
- [27] S. H. Koenig, K. E. Kella, *Magn. Reson. Med.* **2005**, *34*, 227.
- [28] L. E. W. LaConte, N. Nitin, O. Zurkiya, D. Caruntu, C. J. O'Connor, X. Hu, G. Bao, *J. Magn. Reson. Imaging* **2007**, *26*, 1634
- [30] C. Zhang, B. Wangler, B. Morgenstern, H. Zentgraf, M. Eisenhut, H. Untenecker, R. Kruger, R. Huss, C. Seliger, W. Semmler, a. F. Kiessling, *Langmuir* **2007**, *23*, 1427.
- [31] Y. Onuki, I. Jacobs, D. Artemov, Y. Kato, *Biomaterials* **2010**, *31*, 7132.

## **Chapter 3.**

# **Development of MRI/NIRF ‘activatable’ multimodal imaging probe based on iron oxide nanoparticles**

### **3.1. Introduction**

For last decade, multimodal imaging probes have been focused because they present promising potential in improving diagnosis of disease [1, 2]. For multimodal imaging, combination of complementary imaging modalities is an important for accurate disease diagnosis and numerous combinations have been developed and underdeveloped, including MRI/optical [1-12], MRI/PET [13-15] and PET/CT [16-18]. Recently, combination of MRI and optical imaging has drawn attention because they are highly complementary imaging techniques and widely used in clinical practice. MRI is a great technique for providing anatomical information, but has limitation in detecting molecular events such as gene expression and protease activity. On the other hand, optical imaging can visualize functional events at molecular level using various fluorescent probes, but it provides insufficient anatomical information. Combination of these two imaging modalities complements each weakness and maximizes strengths.

Superparamagnetic iron oxide nanoparticle (SPION) is one of the popular candidates for magnetic resonance imaging because it has high T2 relaxivity for efficient imaging on T2 weighted MRI and relatively lower toxicity than gadolinium based T1 contrast agent. However, SPION has

limitations such as hydrophobic surface and poor water stability. For these reasons, a number of stabilization methods using various surface modification techniques with biocompatible materials have been developed [19-22]. Recently, stabilized SPION based multimodal imaging probe, consisting MRI and optical imaging modalities, are actively investigated [8, 14, 19, 23, 24]. Zhang et al. reported MRI/optical dual imaging probe for brain tumor imaging using PEGylated chitosan as a outer shell for SPION [19], and Jon et al. published several articles about fabrication method of dye loaded thermally cross-linked SPION for dual imaging [20, 25]. These researches were successful in providing combination of two different modalities; however, there are few researches based on 'activatable' imaging probe. Fluorescence quenching effect of optical dyes and quantum dots using iron oxide nanoparticles or nanocrystal were reported by several research groups. Nie reported that increasing concentration of nanocrystals decreased fluorescence emission intensity of quantum dots embedded in mesoporous silica beads [10]. Weissleder group synthesized CLIO-based dual imaging probes and reported activatable optical imaging based on attachment and detachment of dyes on the surface of MR-responsive iron oxide nanoparticles [11].

Nanoparticles with fluorescence quenching property have been investigated for the past few decades because these nanoparticles can provide activatable fluorescence modality, such as stimuli sensitive fluorescence on-off system, to image molecular event. Noble metals representing with gold and silver nanoparticles are well-known candidates displaying fluorescence quenching property and a number of researches about ‘activatable’ imaging probes using these nanoparticles have been reported [26, 27]. However, there are few researches about ‘activatable’ imaging probes based on fluorescence quenching of iron oxide nanoparticles. Here, simple and novel fabrication method of enzyme triggered ‘activatable’ dual imaging probe for cancer detection is described based on iron oxide and explore the potential of the probe as T2 contrast agent for MRI and NIRF imaging.

### **3.2. Experimental**

**Preparation of PCM-CS.** Cy5.5-MMP substrate and poly(ethylene glycol) (PEG) with the molecular weight of 5 K were conjugated on  $\text{Fe}_3\text{O}_4@\text{SiO}_2$  core-shell nanoparticles. Amine capped  $\text{Fe}_3\text{O}_4@\text{SiO}_2$  nanoparticles were prepared using aminopropyltriethoxysilane. Cy5.5

labeled MMP-2 substrate, Cy5.5-Gly-Pro-Leu-Gly-Val-Arg-Gly, was covalently introduced to the surface of core-shell nanoparticles via EDC/NHS coupling method. 1.0 mg ethyl(dimethylaminopropyl) carbodiimide (EDC) and 1.0 mg N-hydroxysuccinimide (NHS) were dissolved in 1.0 mL deionized water, followed by the addition of 0.5 mg Cy5.5 labeled MMP-2 substrate. The solution was added into 5.0 mL core-shell nanoparticles and the reaction mixture was vigorously stirred for 12 h at room temperature in darkness. The product was dispersed into 5.0 mL deionized water after 3 times washing with deionized water through centrifugation at 13000 rpm for 30 min. The product was stored at 4 °C in darkness for further experiments. Cy5.5 labeled MMP-2 substrate conjugated core-shell nanoparticles were coded CM-CS.

mPEG-COOH was used to modify the surface of CM-CS for enhanced water stability and reduced liver uptake. 2.0 mg mPEG-COOH, 1.0 mg EDC and 1.0 mg NHS were dissolved in 1.0 mL deionized water. After 30 min stirring, the reaction mixture was added into 5.0 mL CM-CS and stirred for additional 12 h. Final product (PCM-CS) was dispersed in 5.0 mL deionized water after 5 times washing with deionized water through centrifugation at 13000 rpm for 30 min. Iron content of the product was

measured by ICP-MS (Perkin-Elmer Sciex, CA, USA) and morphology of the product was evaluated by transmittance electron microscopy (JEM1010, JEOL Ltd., Tokyo, Japan) installed at NICEM in Seoul National University.

**In vivo NIRF imaging.** SCC7 cells ( $1 \times 10^6$  cells/mouse) cultured in RPMI 1640 medium containing 10% fetal bovine serum were injected subcutaneously into the backs of 5-week old BALB/C mice. When tumors had grown to 10 mm in size, the PCM-CS was intravenously injected. In the MMP-2 inhibition experiment, an MMP-2 blocker was intratumorally administered into the SCC7 tumors 30 min prior to injection of the PCM-CS probe. As a negative control, the PCM-CS was intravenously injected into the normal mice without cultured-cell injection. NIRF tomographic images were obtained with an eXplore Optix system (ART Advanced Research Technologies Inc., Montreal, Canada). After injection of PCM-CS, the fluorescence recovery profiles in SCC7 tumor-bearing mice were imaged with the laser power and count time settings optimized at 30 W and 0.3 s per point, respectively. Excitation and emission spots were raster-scanned in 1 mm steps over the selected region of interest to generate emission wavelength scans. A 670 nm pulsed laser diode was applied to excite Cy5.5

molecules. NIR fluorescence emission at 700 nm was collected and detected with a fast photomultiplier tube (Hamamatsu, Japan) and time-correlated single photon counting system (Becker and Hickl GmbH, Berlin, Germany).

**In vivo magnetic resonance imaging.** In vivo magnetic resonance images were obtained using a MRI scanner at 3.0-T field strength (Tim Trio; Siemens, Erlangen, Germany), after the probe was intravenously injected into the mice prepared as described above. Mice were placed in the imaging chamber and imaged before injection and at determined time intervals after injection. A multi-spin echo multi-slice imaging sequence was used to determine T2 values in tumor and normal tissues using following parameters: TR = 51 ms, TE = 20 ms and slice thickness of 0.6 mm. MRI scanning was obtained from five mice and the relative intensity of T2 was averaged.

### **3.3. Results and discussion**

Multimodal core-shell nanoparticles were stabilized with mPEG with the molecular weight of 5 K and decorated by Cy5.5-MMP substrate, namely, Cy5.5-Gly-Pro-Leu-Gly-Val-Arg-Gly (Figure 3-1). Transmission

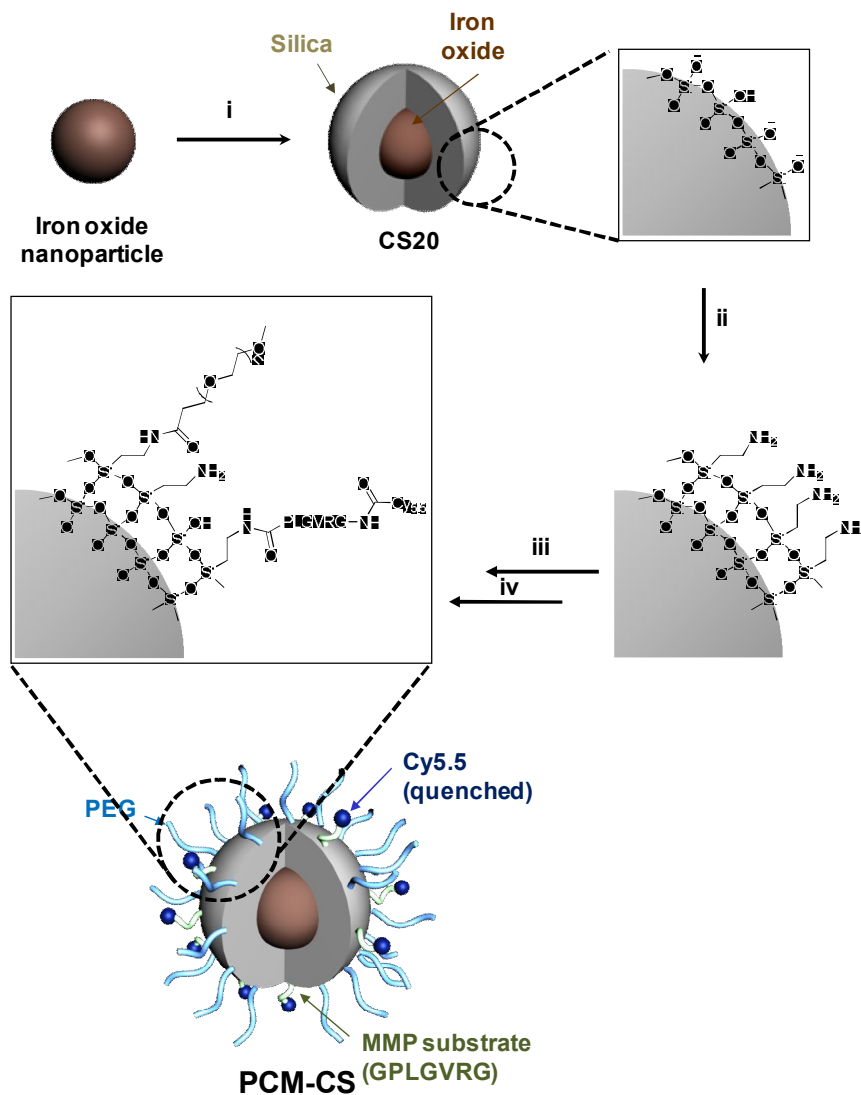


**Figure 3-1.** Fabrication method of PCM-CS; (i) Triton-X, 1-Octanol, TEOS,  $\text{NH}_4\text{OH}$ , Cyclohexane, rt, 72 h; (ii) APTES, EtOH, 25 °C, 6 h; (iii) Cy5.5-MMP substrate, EDC, NHS,  $\text{H}_2\text{O}$ , 25 °C, 12 h; (iv) mPEG-COOH, EDC, NHS,  $\text{H}_2\text{O}$ , 25 °C, 12 h.

electron microscopy images revealed uniform core-shell structured PCM-CS with an average size of about 19 nm (Figure 3-2a). The PCM-CS was well dispersed in phosphate buffer saline (PBS) and the size in aqueous condition was  $43.1 \pm 6.3$  nm due to the presence of hydrophilic PEG chains as shown in Figure 3-2b. Covalently bonded PEG chains endowed the PCM-CS with the long-term stability in PBS solution without any noticeable aggregation up to 7 days or longer (Figure 3-2c). The NIRF signals were completely quenched when measured with fluorometer. PCM-CS was treated with HF to measure full fluorescence of Cy5.5 and the total amount of Cy5.5 conjugated on the surface of silica outer layers since Cy5.5 was stable enough in HF condition to produce the same fluorescence intensity with that in PBS. Considering the total amount of Cy5.5 and the surface area of PCM-CS, the averaged distance between Cy5.5s was 14.21 nm, which is the distance beyond FRET-based quenching effect, proving that iron oxide nanoparticles had an ability to quench the fluorescence of nearby fluorophore. The quenching efficiency (QE) of the PCM-CS was calculated using the following formula,  $100 \times (1 - \beta)$ , where  $\beta$  is the ratio of fluorescence of the quenched to the dequenched state. The QE of the PCM-CS was calculated to be 97.2. The exact quenching mechanism of

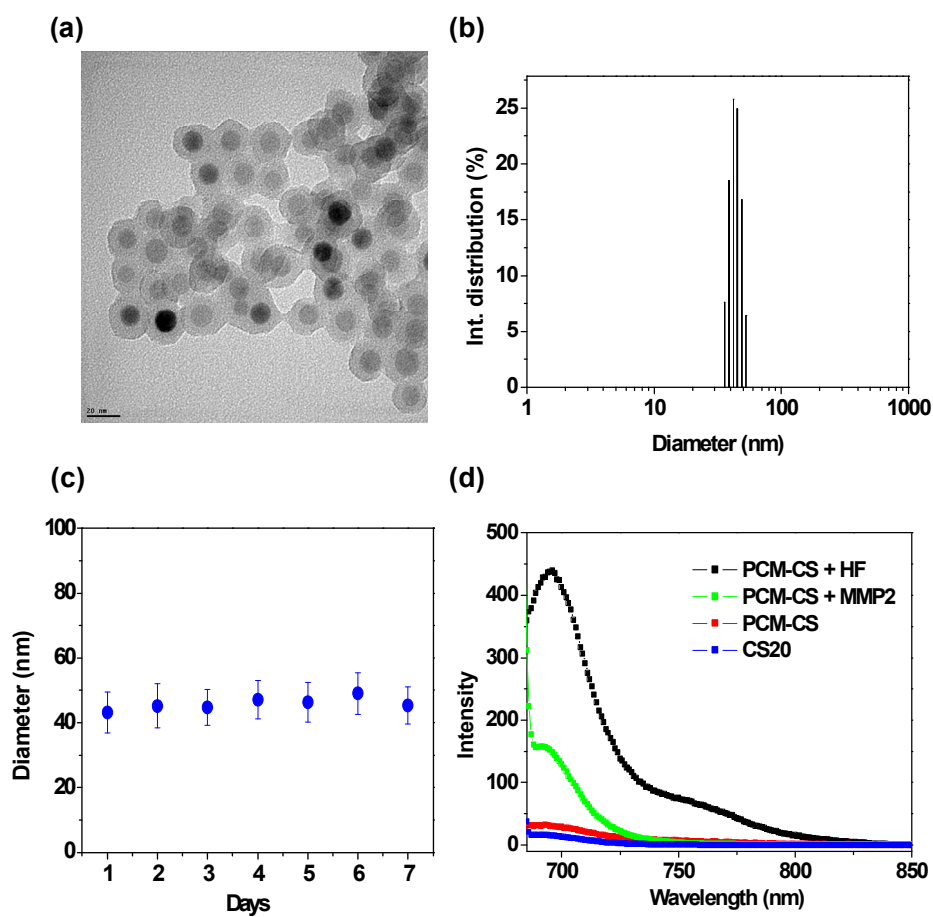


**Figure 3-2.** (a) TEM images of PCM-CS nanoparticles, (b) size distribution of PCM-CS by dynamic light scattering, (c) stability of PCM-CS in PBS, (d) Fluorescence spectra of PCM-CS, HF treated PCM-CS, MMP-2 treated PCM-CS, and CS20.

the fluorophores by iron oxide nanoparticles within a certain distance has not been clarified yet. Recovered NIRF signal of MMP-2 treated PCM-CS was 35.1 % of full fluorescence of Cy5.5 on the PCM-CS (Figure 3-2d). According to our previous report, about 30 % of peptide was cleaved from gold nanoparticles by activated MMP-2 and these results demonstrated that PEG chains on the surface of PCM-CS did not prevent cleavage of peptide by MMP-2.

MMP-2 sensitivity of the PCM-CS was evaluated *in vitro* by incubation in a vial containing the reaction buffer and 15 nM of activated MMP-2. Time dependence of NIRF recovery of PCM-CS was measured at the time points of 0 h, 0.5 h, 1 h and 2 h with a fixed excitation wavelength of 676 nm. Figure 3-3a and 3-3b displayed that NIRF gradually increased over the time and the intensity of recovered NIRF reached maximum after 2 h incubation. Sensitivity of the PCM-CS against MMP-2 was evaluated using the same experimental setup with different concentrations of activated MMP-2 in the Kodak image station. As shown in Figures 3-3c and 3-3d, NIRF signal of PCM-CS recovered proportionately with MMP-2 concentration and recovered NIRF signal of PCM-CS against MMP-2 could be detected at the sub-nanomolar enzyme level, showing that prepared core-

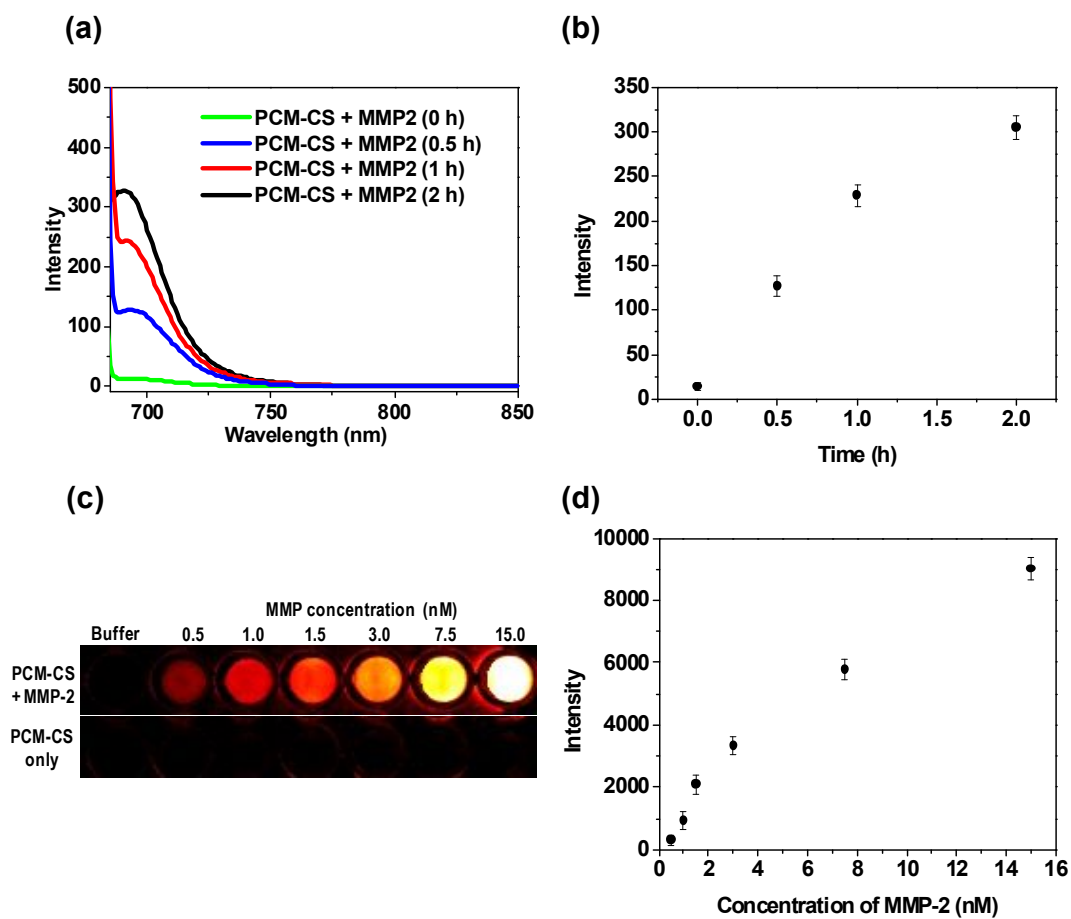


**Figure 3-3.** Fluorescence recovery against MMP-2 in various condition (a) time dependent fluorescence spectra with 15 nM MMP-2, (b) time dependent fluorescence change at 695 nm, and (c) NIRF image sections of a 96-well microplate of the PCM-CS containing various MMP-2 concentration and (d) corresponding fluorescence intensity at 695 nm.

shell nanoparticles exhibited excellent optical sensitivity against a target protease.

SCC7 tumor bearing xenografted mice were selected as the animal model. The SCC7 cell line is well-known for its high MMP-2 expression [26]. In vivo optical imaging of subcutaneously xenografted mice was performed at 3, 6, 12, and 24 h after injection of PCM-CS with and without MMP-2 inhibitor using the preclinical optical imaging system eXplore Optix configured for NIRF probe detection with excitation and emission at 670 and 700 nm, respectively. As shown in Figure 3-4c, intravenous injection of the probes into normal mice did not produce detectable NIRF signals even after 24 h. In case of tumor-bearing mice in Figure 3-4a, NIRF signal was recovered with time and reached a maximum value at 12 h post injection. The tumor region was clearly visualized at 12 h post injection and NIRF signal intensity at tumor region was 3~4 times stronger than normal tissue region. Tumors were known to have leaky vascular structure and nanoparticles showed enhanced permeability through the leaky vessels with preferential accumulation at tumor regions. The recovered fluorescence proved that PCM-CS was stable enough in the physiological condition during the systemic circulation and accumulated at the targeted

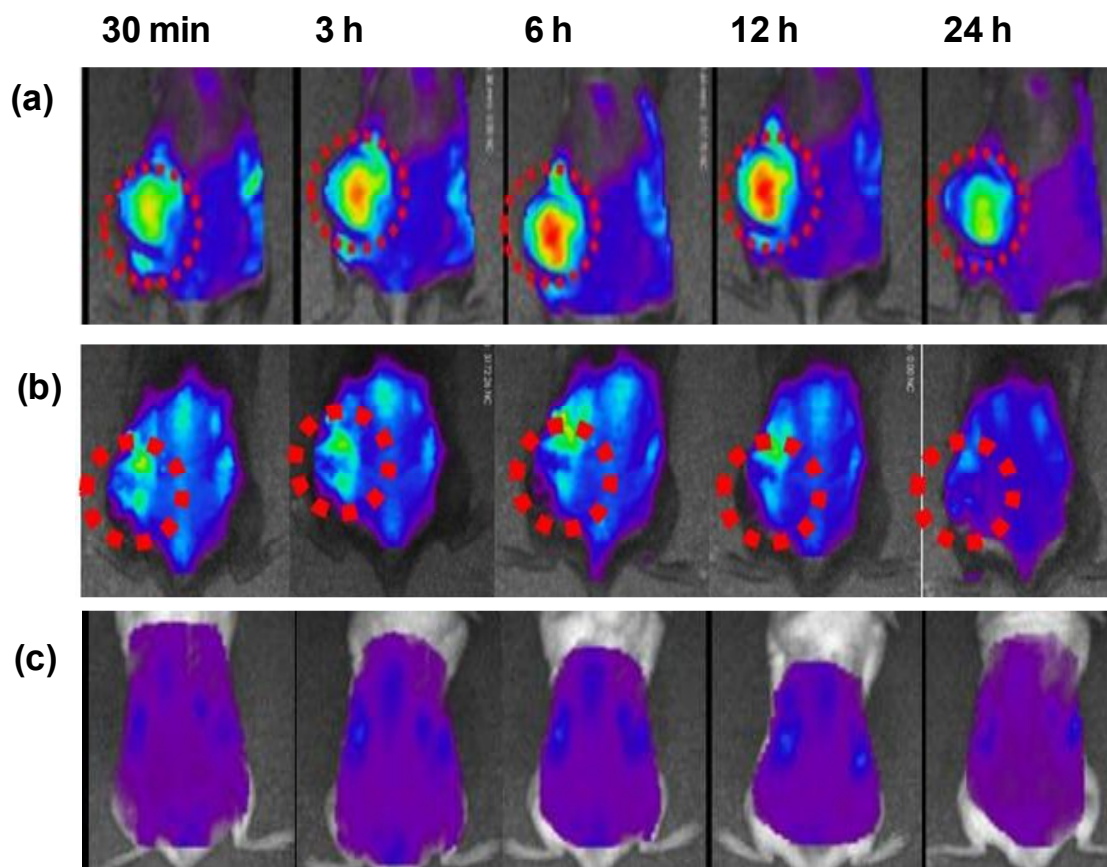


**Figure 3-4.** NIRF tomographic images of tumor-bearing mice after injection of PCM-CS (a) without inhibitor, (b) with inhibitor and (c) normal mice after injection of PCM-CS (blue: low intensity, red: high intensity).

tumor sites. Administration of MMP-2 inhibitor 30 min before the injection of the PCM-CS probe significantly reduced tumor contrast as shown in Figure 3-4b and reduction of fluorescence proved that PCM-CS had sensitivity against MMP-2 in tumor region. Slight NIRF signal at some time points was attributed to the limited diffusion of the inhibitor throughout the whole tumor region. It was believed from the results that prepared PCM-CS has a potential application in optical imaging for tumor visualization and drug/protease activity screening in living organisms.

Mice were sacrificed at 24 h post injection of PCM-CS, and NIRF images of excised organs from PCM-CS treated mice were obtained using Kodak imaging station in Figure 3-5. The NIRF signal of the excised tumors was 5~10 times stronger than other organs, such as liver, spleen, kidney, lung, and heart. The intensity of excised liver was the second highest probably due to the uptake of the nanoparticles by the RES system and nonspecific peptide cleavage.

Magnetic resonance images in Figure 3-6 were with human MRI scanner at 1.5-T field strength using the SCC7 bearing xenografted mice. Each mouse was imaged prior to, and at various time points after intravenous injection of 0.05 ml PCM-CS with concentration of 0.15 mg

Fe/mL. The relative signal enhancement of the ROI in the T2-weighted image was evaluated by the comparison between the tumor regions and the healthy muscle regions of the mice. Noticeable darkening appeared at 6 h

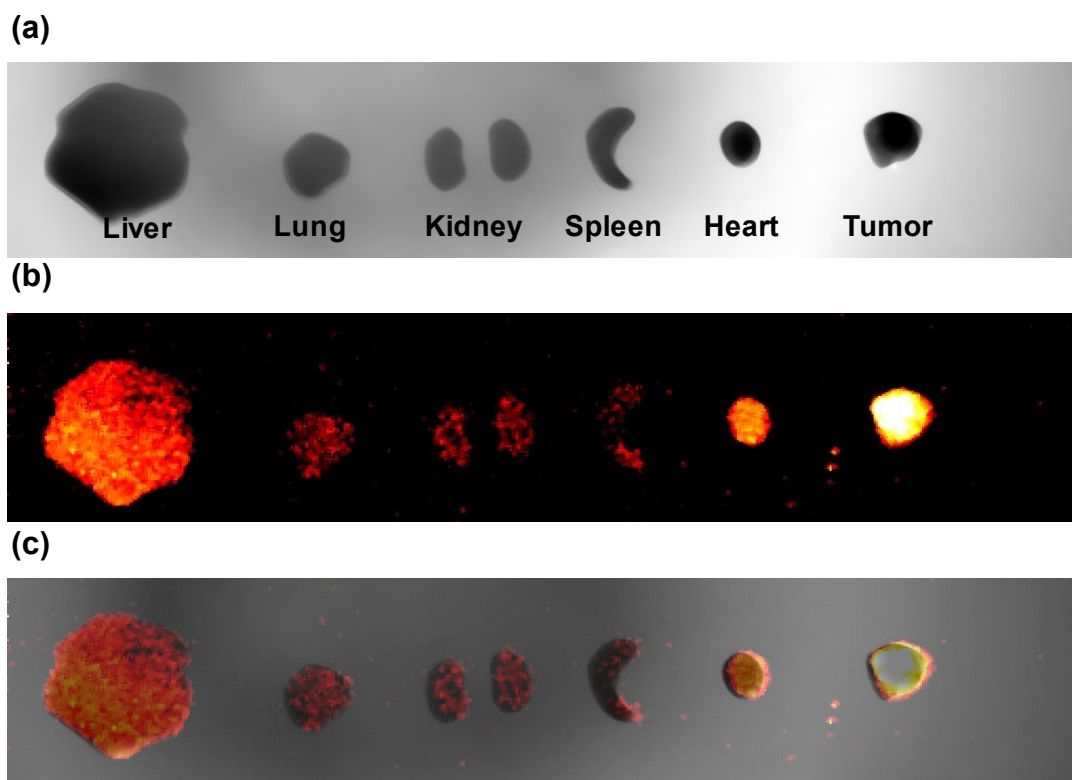


**Figure 3-5.** Images of excised organs and tumor at 24 h post injection of PCM-CS (a) white light image, (b) NIRF image and (c) merged image.

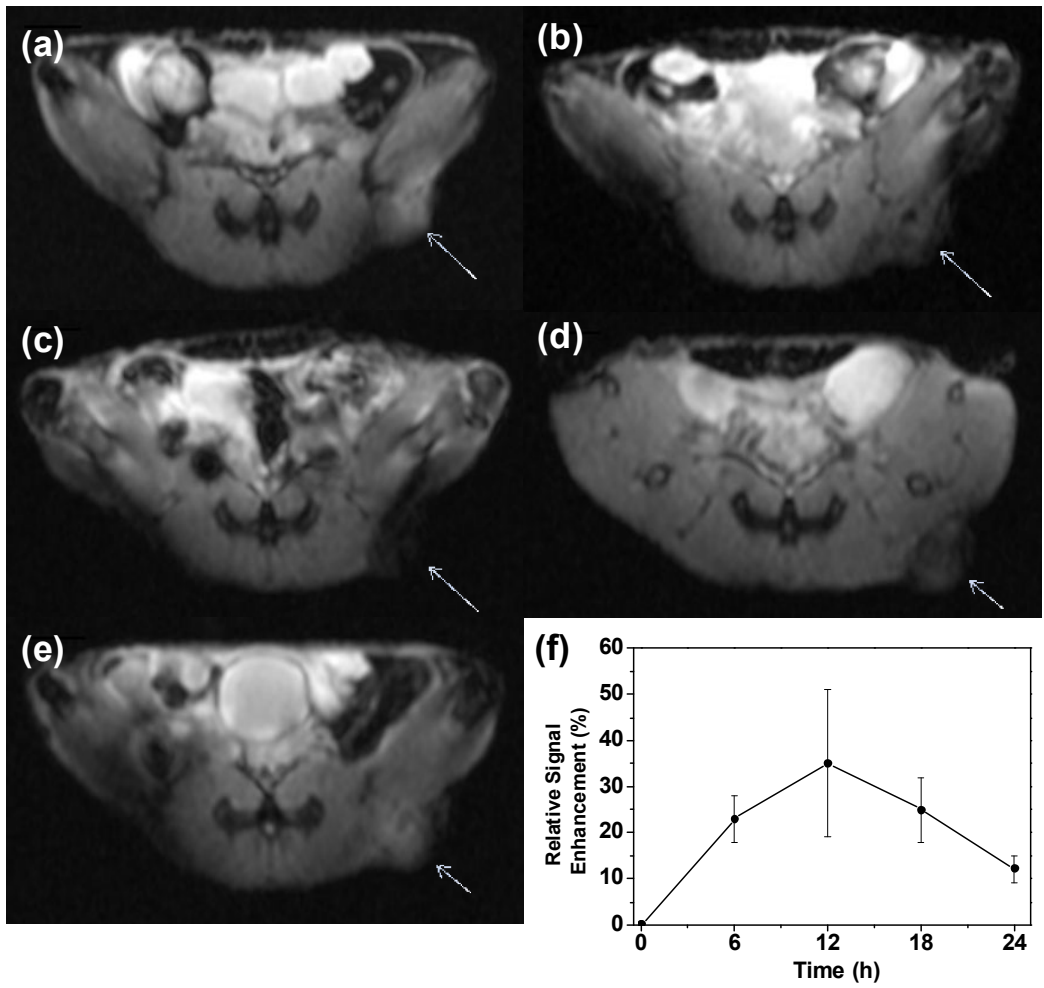


**Figure 3-6.** Magnetic resonance images of PCM-CS treated mice at various time points, (a) Pre-injection (b) 3 h, (c) 6 h, (d) 12 h, (e) 24 h after injection, and (f) relative T2 intensity of tumor regions.

post-injection of PCM-CS and the decrease in signal was maximized at 12 h post-injection, which was in a good agreement with the fluorescence recovery results. The maximum decrease in signal at 12 h was up to 34.2 % compared to the signal prior to the injection, meaning that PEG-stabilized PCM-CS was increasingly accumulated at the targeted tumor sites after systemic circulation. The relative signal enhancement in the shortening in the T2 value correlates with the signal decrease as a result of the strong T2-weighted MR images was sufficient to confirm the location of tumor region.

### **3.4. Conclusion**

Multimodal imaging probes containing both anatomical and functional imaging modality have been recently investigated due to their ability to obtain accurate biological information. Herein, we described the fabrication method of iron oxide based core-shell nanoparticles for 'activatable' dual imaging, which were available to provide anatomical and activatable functional images and highlighted the potential in disease diagnosis. The probe with two different imaging modalities, NIRF optical and magnetic resonance imaging successfully visualized the tumor regions

via tail-vein injection. The distinguished properties showed promising potential of the activatable dual imaging probe system as a novel molecular imaging probe for MRI and NIRF optical imaging.

### 3.5. References

- [1] M. Rudin, R. Weissleder, *Nat. Rev. Drug Discov.* **2003**, *2*, 123.
- [2] L. E. Jennings, N. J. Long, *Chem. Commun.* **2009**, *28*, 3511.
- [3] L. Zhang, B. Liu, S. Dong, *J. Phys. Chem. B* **2007**, *111*, 10448.
- [4] M. Ogawa, C. A. Regino, J. Seidel, M. V. Green, W. Xi, M. Williams, N. Kosaka, P. L. Choyke, H. Kobayashi, *Bioconjugate Chem.* **2009**, *20*, 2177.
- [5] S. K. Mandal, N. Lequeux, B. Rotenberg, M. Tramier, J. Fattaccioli, J. Bibette, B. Dubertret, *Langmuir* **2005**, *21*, 4175.
- [6] Z. Medarova, W. Pham, Y. Kim, G. Dai, A. Moore, *Int. J. Cancer* **2006**, *118*, 2796.
- [7] S. Aime, M. Botta, M. Fasano, E. Terreno, *Chem. Soc. Rev.* **1998**, *27*, 19.
- [8] M. Mulder, A. W. Griffioen, G. J. Strijkers, D. P. Cormode, K. Nicolay, Z. A. Fayad, *Nanomedicine* **2007**, *2*, 307.

- [9] E. A. Schellenberger, D. Sosnovik, R. Weissleder, L. Josephson, *Bioconjugate Chem.* **2004**, *15*, 1062.
- [10] T. R. Sathe, A. Agrawal, S. Nie., *Anal. Chem.* **2006**, *78*, 5627.
- [11] L. Josephson, M. F. Kircher, U. Mahmood, Y. Tang, R. Weissleder, *Bioconjugate Chem.* **2002**, *13*, 554.
- [12] K. Chen, J. Xie, H. Xu, D. Behera, M. H. Michalski, S. Biswal, A. Wang, X. Chen, *Biomaterials* **2009**, *30*, 6912.
- [13] C. Wong, T. Stylianopoulos, J. Cui, J. Martin, V. P. Chauhan, W. Jiang, Z. Popovic, R. K. Jain, M. G. Bawendi, D. Fukumura, *Proc. Natl. Acad. Sci.* **2011**, *108*, 2426.
- [14] J. Xie, K. Chen, J. Huang, S. Lee, J. Wang, J. Gao, X. Li, X. Chen., *Biomaterials* **2010**, *31*, 3016.
- [15] T. Nam, S. Park, S. Y. Lee, K. Park, K. Choi, I. C. Song, M. H. Han, J. J. Leary, S. A. Yuk, I. C. Kwon, K. Kim, S. Y. Jeong, *Bioconjugate Chem.* **2010**, *21*, 578.
- [16] X. Yang, H. Hong, J. J. Grailer, I. J. Rowland, A. Javadi, S. A. Hurley, Y. Xiao, Y. Yang, Y. Zhang, R. J. Nickles, W. Cai, D. A. Steeber, S. Gong, *Biomaterials* **2011**, *32*, 4151.
- [17] H. Y. Lee, Z. Li, K. Chen, A. R. Hsu, C. Xu, J. Xie, S. Sun, X. Chen,

- J. Nucl. Med.* **2008**, *49*, 1371.
- [18] G. Antoch, F. M. Vogt, L. S. Freudenberg, F. Nazaradeh, S. C. Goehde, J. Barkhausen, G. Dahmen, A. Bockisch, J. F. Debatin, S. G. Ruehm, *J. Am. Med. Assoc.* **2003**, *290*, 3199.
- [19] O. Veiseh, C. Sun, C. Fang, N. Bhattarai, J. Gunn, F. Kievit, K. Du, B. Pullar, D. Lee, R. G. Ellenbogen, J. Olson, M. Zhang, *Cancer Res.* **2009**, *69*, 6200.
- [20] H. Lee, M. K. Yu, S. Park, S. Moon, J. J. Min, Y. Y. Jeong, S. Jon, *J. Am. Chem. Soc.* **2007**, *129*, 12739.
- [21] K. M. K. Selim, J.-H. Lee, S.-J. Kim, Z. Xing, I.-K. Kang, Y. Chang, H. Guo, *Macromol. Res.* **2006**, *14*, 646.
- [22] J. H. Choi, S. Lee, H. J. Kang, J. Y. Lee, J. Kim, H. O. Yoo, T. R. Stratton, B. M. Applegate, J. P. Youngblood, H. J. Kim, K. N. Ryu, *Macromol. Res.* **2010**, *18*, 504.
- [23] M. F. Kircher, U. Mahmood, R. S. King, R. Weissleder, L. Josephson, *Cancer Res.* **2003**, *63*, 8122.
- [24] E. S. Olson, T. Jiang, T. A. Aguilera, Q. T. Nguyen, L. G. Ellies, M. Scadeng, R. Y. Tsien, *Proc. Nat. Acad. Sci.* **2010**, *107*, 4311.
- [25] M. K. Yu, Y. Y. Jeong, J. H. Park, S. J. Park, J. W. Kim, J. J. Min, K.

- W. Kim, S. Jon, *Angew. Chem. Int. Ed.* **2008**, *47*, 5362.
- [26] S. Lee, E.-J. Cha, K. Park, S.-Y. Lee, J.-K. Hong, I.-C. Sun, S. Y. Kim, K. Choi, I. C. Kwon, K. Kim, C.-H. Ahn, *Angew. Chem. Int. Ed.* **2008**, *47*, 2804.
- [27] N. L. Rosi, D. A. Giljohann, C. S. Thaxton, A. K. R. Lytton-Jean, M. S. Han, C. A. Mirkin, *Science* **2006**, *312*, 1027.

## **Chapter 4.**

**Activatable NIRF/MRI dual imaging probe  
using glycol chitosan coated superparamagnetic  
iron oxide nanoparticles**

#### 4.1. Introduction

Superparamagnetic iron oxide nanoparticles (SPIONs) are one of the famous materials which enable to use as a T2 contrast agent due to their high relaxivity and relatively low toxicity than gadolinium based contrast agents. In addition, SPIONs generate heat under alternating magnetic field and can be exploited for thermotherapy agent. In spite of these advantages, SPIONs has several limitations due to their hydrophobic and highly oxidative surface and appropriate surface modification is essential to SPIONs for in vivo application, consequently. Numerous fabrication and surface modification methods have been developed for several decades <sup>[1-17]</sup>.

PEG, chitosan derivatives and hyaluronic acid are well-established polymeric materials for surface modification of SPIONs and inorganic materials such as silica was also used for stabilizing SPIONs in aqueous solution. Hyaluronic acid was introduced as a stabilizing agent for SPIONs by Park et. al. Park et. al. used bio-inspired adhesive, 3, 4 - dihydroxy phenylalanine (DOPA), to immobilize hyaluronic acid molecules on the surface of SPIONs <sup>[18]</sup>. Zhang et. al. reported fabrication method of PEGylated chitosan coated SPIONs and successfully visualized brain tumor in vivo <sup>[1]</sup>. Recently, the study using glycol chitosan coated SPION was

reported to demonstrate of relationship between tumor accumulation and pH sensitive glycol chitosan coating. Our group previously introduced PEGylated core-shell nanoparticles, which has SPION core, and evaluated the potential as a T2 contrast agent for cancer imaging <sup>[19]</sup>.

Multimodal imaging is received attention for efficient diagnosis of diseases and SPIONs are combined with other imaging modalities such as PET, NIRF and CT. In particular, NIRF modalities were focused as a partner of SPIONs because the NIRF modalities and MRI are highly complementary imaging tools <sup>[3-14]</sup>. MRI is well-known imaging technique which is suitable to represent anatomical information, but limited to evaluate information of biological events in molecular level such as presence of specific protein, gene expression and protease activity. In contrast, NIRF based optical imaging provides details of biological event in molecular level using appropriate linkers and molecular triggers, but has several drawbacks in representing anatomical details. For these reasons, synergies are expected by the combination of these two imaging techniques.

Here, we described the fabrication method of glycol chitosan coated SPIONs with activatable NIRF and modalities and demonstrated the potential as a NIRF/MRI dual imaging probe in vivo. Glycol chitosan was

introduced to make stable and tumor targeting SPIONs as a MRI contrast agent. It is previously reported that glycol chitosan based nanoparticles shows distinguished stability, biocompatibility and tumor targeting ability by enhanced permeation and retention (EPR) effect. For activatable NIRF imaging, matrix metalloproteinase (MMP) sensitive peptide based probes were chemically conjugated on glycol chitosan coating layer. Fluorescence of the probe was strongly quenched by organic black hole quencher and iron oxide. Quenched fluorescence was selectively recovered by cleavage of peptide substrate linkers upon exposure to the active MMPs, which are over-expressed in tumor. Therefore, we expect that our probe can provide MR image with high spatial resolution and stimuli-sensitive fluorescence image.

## 4.2. Experimental

**Materials.** 50 nm size SPIONs (oleic acid stabilized, in chloroform) were purchased from Oceananotech (Springdale, AR). Glycol chitosan (GC, 95 %, DP > 400), N-hydroxysuccinimide (NHS, 98 %), 1-Ethyl-3-(3-dimethylaminopropyl) carbodiimide hydrochloride (EDC, 98 %), 3, 4 – dihydroxy phenylalanine (DOPA, 99 %) and sodium dodecyl sulfate (SDS, 95 %) were obtained from Sigma Aldrich (St. Louis, MO). Cy5.5 mono N-

hydroxysuccinamide ester (Cy5.5-NHS) and black hole quencher 3 (BHQ3) were commercially available from GE healthcare (Piscataway, NJ) and MMP-2 substrate (Gly-Pro-Leu-Gly-Val-Arg-Lys) were purchased from Anygen (Korea). All reagents were used without additional purification.

**Synthesis of GC-DOPAC.** DOPAC was conjugated with glycol chitosan via simple EDC/NHS coupling method in aqueous solution. GC (500.0 mg) and DOPAC (197.0 mg, 1.0 mmol) were dissolved in 100.0 mL distilled water and the solution was placed in 250 mL round bottom flask. Then, EDC (3.0 mmol) and NHS (3.0 mmol) were added into the reaction solution. After additional 24 h stirring, the solution was placed in pre-swollen dialysis membrane with molecular weight cut off 3500 and dialyzed against distilled water for 3 days. The solution was lyophilized for 3 days and light-brown colored product was obtained. Degree of DOPAC conjugation was evaluated by UV spectroscopy using Shimadzu UV-2650 PC system.

**Preparation of GC coated SPIONs.** GC coated SPIONs were prepared through followed two synthetic steps. First, SPIONs with 0.5 mg

Fe content were diluted in 30.0 mL chloroform and the solution was placed in 100 mL beaker. Then, 150 mg SDS was dissolved in 30 mL deionized water and the solution was added into the SPION solution. After 12 h vigorously stirring, chloroform in the reaction mixture was evaporated. Unbound SDS was removed by 3 times centrifugation with deionized water at 12,000 rpm. The product was stored at 4 °C for further experiment. Size distribution and particle stability of prepared SPION solution were demonstrated by DLS using Otsuka ELS-Z particle analyzer equipped with He-Ne laser at a wavelength of 630 nm. Second, 10 mL aqueous GC-DOPAC solution (20 mg/mL) was prepared and the GC-DOPAC solution was mixed with previously prepared SPION solution (30 mL). The mixture was vigorously stirred for 24 h and unreacted GC-DOPAC was removed by 3 times centrifugation. Size distribution and morphology of the product, GC coated SPION (GC-SPION), were analyzed by transmission electron microscopy (JEOL, Japan), DLS and FT-IR.

**Preparation of BCMG-SPION.** Cy5.5 and BHQ3 labeled MMP-2 substrate was prepared by previously reported procedure. Cy5.5-NHS (8.4  $\mu\text{mol}$ ) and MMP substrate (4.0  $\mu\text{mol}$ ) were dissolved in 200  $\mu\text{l}$  DMF

containing NMM (52  $\mu\text{mol}$ ) and DMAP (2.5  $\mu\text{mol}$ ) at room temperature and stirred for 2 h. The Cy5.5-MMP substrate was precipitated with 5.0 mL diethyl ether and the precipitate was dried in vacuum. Removal of protecting groups of lysine was achieved with 1.0 mL of TFA/water/anisole solution (95:2.5:2.5, v/v). Cy5.5-MMP substrate was purified by reversed-phase high performance liquid chromatography (RP-HPLC) using Agilent 1200 system (Agilent Technologies, Palo Alto, CA, USA): 22 % to 40 % acetonitrile containing 0.1 % TFA versus DW containing 0.1 % TFA over 20 min at a flow rate of 4.0 ml/min. Then, BHQ-3 (0.9  $\mu\text{mol}$ ) was coupled with primary amine of the lysine in 30.0  $\mu\text{l}$  DMF and 9.7  $\mu\text{mol}$  NMM and 1.0  $\mu\text{mol}$  DMAP were added into the reaction solution. After 12 h stirring at room temperature, the product (Cy5.5-MMP substrate-BHQ) was obtained by RP-HPLC and analyzed with Voyage-DE™ STR matrix-assisted laser desorption ionization with time of flight (MALDI-TOF) mass spectrometer (Applied Biosystems, Foster City, CA, USA). Prepared Cy5.5-MMP substrate-BHQ was conjugated with GC-SPION using simple EDC/NHS coupling chemistry. Briefly, 0.1 mg Cy5.5-MMP substrate-BHQ, 1.0 mg EDC and 1.0 mg NHS were dissolved in 0.5 mL deionized water. Then, the solution was added into 10.0 mL GC-SPION solution and stirred for 12 h.

Final product (BCMG-SPION) was dispersed in 10.0 mL deionized water after 5 times washing through centrifugation at 13000 rpm for 30 min. Iron contents of the product was measured by induced coupled plasma mass spectrometer (ICP-MS). Every reaction steps were carried out in darkness.

**In vivo NIRF imaging.** SCC7 cells ( $1 \times 10^6$  cells/mouse) cultured in RPMI 1640 medium containing 10% FBS were injected subcutaneously into the backs of mice (BALB/C, 5-6 weeks old, male). When tumors had grown to 10 mm in size, the 0.1 mL BCMG-SPION (0.15 Fe mg/mL) was intravenously injected through tail vein. For the MMP-2 inhibition experiment, TIMP-2 (100  $\mu$ g/mL) was intratumorally administered into the tumor tissue 30 min prior to injection of the BCMG-SPION. MMP expression was evaluated by NIRF tomographic images with an eXplore Optix system (ART Advanced Research Technologies Inc., Montreal, Canada). Tumor bearing mice were imaged on an animal plate heated to 36 °C in the eXplore Optix system and laser power and integration time were 10  $\mu$ W and 0.3 s per point, respectively. A 670 nm pulsed lase diode was used to excite Cy5.5 and fluorescence emission at 700 nm was collected with a fast photomultiplier tube (Hamamatsu, Japan) and time-correlated

single photon counting system (Becker and Hickl GmbH, Berlin, Germany).

**In vivo MR imaging.** For in vivo MR imaging, SCC7 xenografted mice were prepared by same procedure described above. Then, BCMG-SPION was intravenously injected and MR images were obtained at various time point. MR images were obtained by using a human MRI scanner at 1.5-T field strength with a multi-spin echo multi-slice imaging sequence. T2 values in tumor and normal tissues were measured using following parameters: TR = 400 s, TE = 10 ms and slice thickness of 1 mm. MRI scanning was obtained from 5 mice and the relative intensity of T2 was averaged.

### **4.3. Results and discussion**

We designed glycol chitosan coated iron oxide nanoparticle decorated by Cy5.5-MMP substrate-BHQ, Cy5.5-Gly-Pro-Leu-Gly-Val-Arg-Gly-Lys(BHQ)-Gly-Gly, and the schematic illustration were shown in Figure 4-1. Average size of the probe (BCMG-SPION) was 40 nm (by TEM) and 83 nm (by DLS). The result shows that glycol chitosan layer was fully swelled or stretched in aqueous solution. This means that coating layer of the BCMG-SPION can show anti-fouling effect in physiological condition. The BCMG-

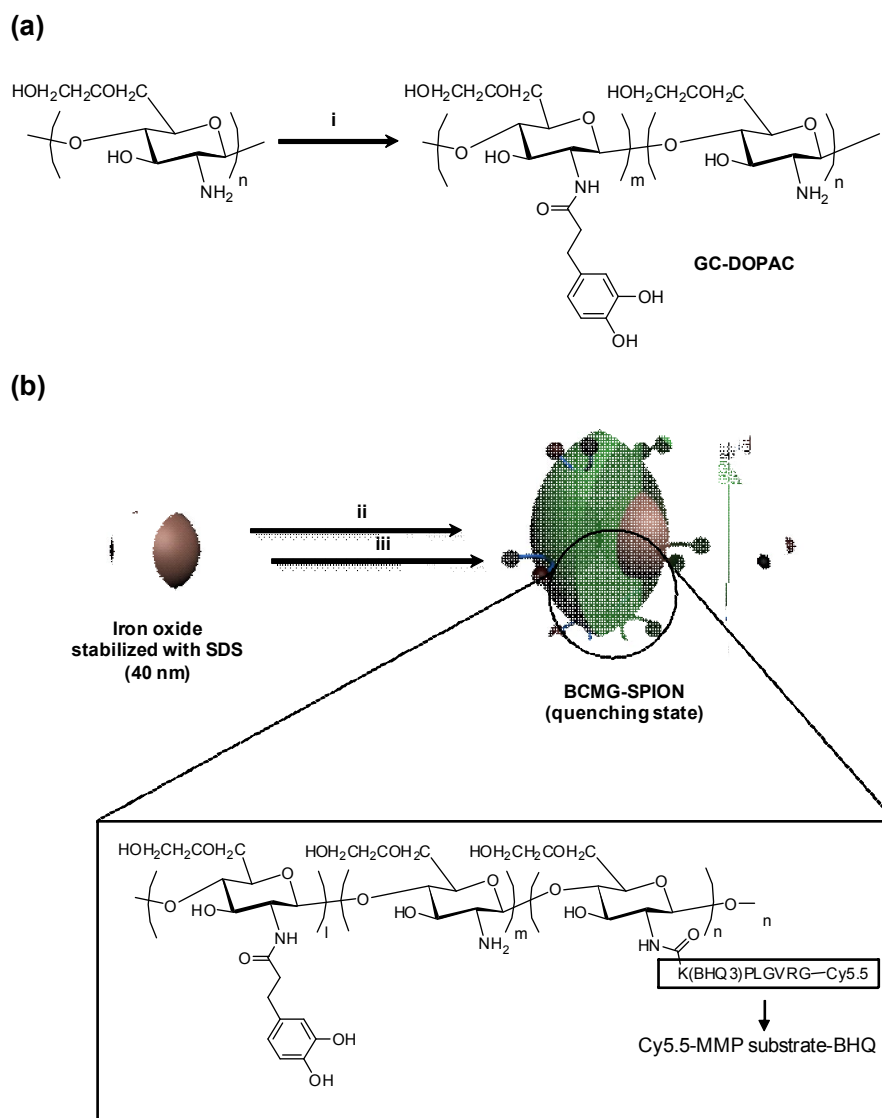


**Figure 4-1.** (a) Synthesis of GC-DOPAC and (b) fabrication of BCMG-SPION; (i) DOPAC, EDC, NHS, DMSO, rt, 24 h; (ii) GC-DOPAC, H<sub>2</sub>O, 6 h; (iii) Cy5.5-MMP substrate-BHQ, EDC, NHS, H<sub>2</sub>O, 25 °C, 12 h.

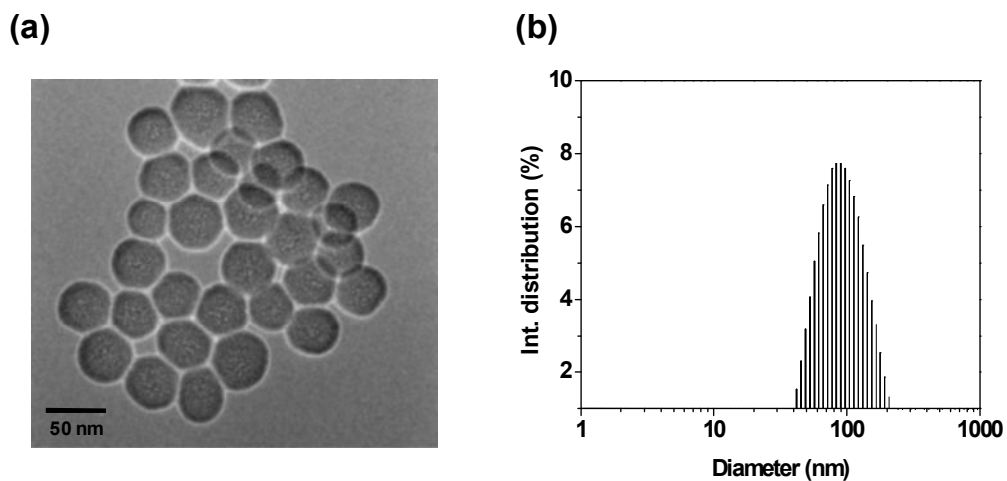


**Figure 4-2.** (a) TEM image and (b) size distribution of BCMG-SPION.

SPION was well dispersed in phosphate buffer saline over a week, and the NIRF was completely quenched when measured with fluorometer (Figure 4-3). The quenching efficiency of the BCMG-SPION was 94.3. Iron oxide nanoparticles and organic black hole quencher were act as fluorescence quencher in this system because of their fluorescence quenching property. Black hole quencher is well known organic fluorescence quencher and fluorescence quenching ability of the iron oxide nanoparticles was previously reported. We reported distance dependent fluorescence

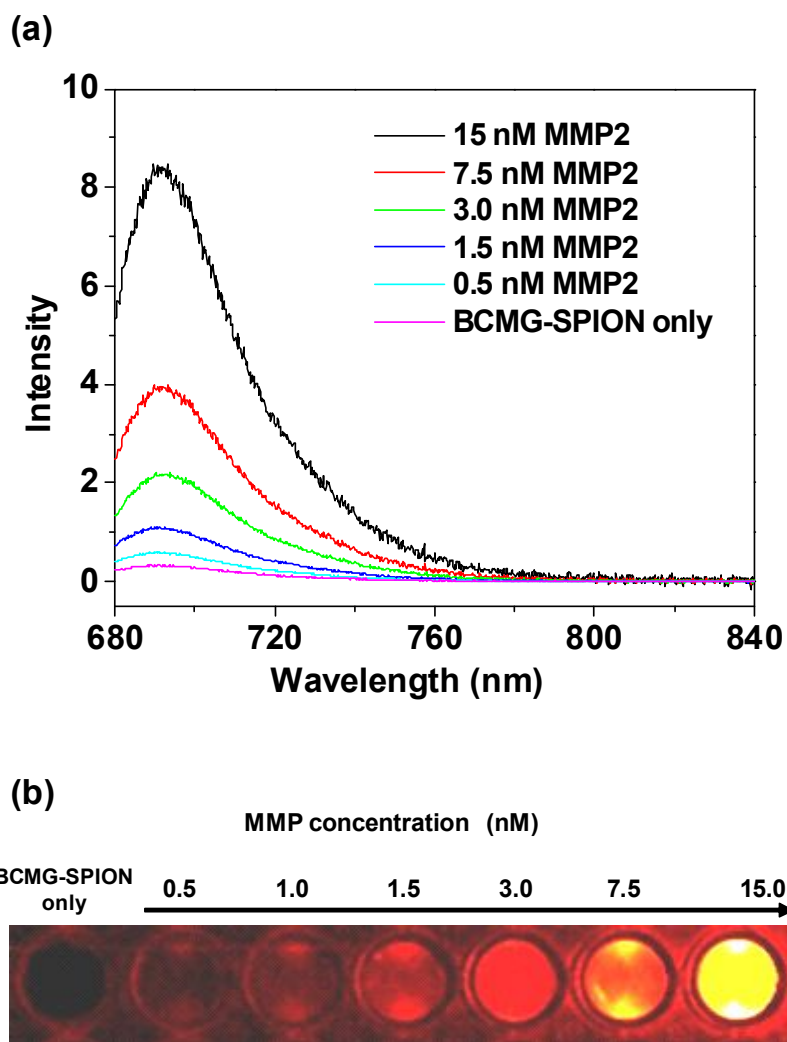


**Figure 4-3.** (a) Fluorescence spectra and (b) NIRF images of BCMG-SPION after 2 h reaction with MMP-2.

quenching of iron oxide nanoparticles and the quenching phenomenon of this system can be explained by distance between Cy5.5 and iron oxide. In spite of quenching ability of iron oxide nanoparticle, organic black hole quencher was introduced to the system because distance between Cy5.5 and iron oxide were not close enough to quench fluorescence of Cy5.5.

MMP-2 sensitivity of the BCMG-SPION was evaluated *in vitro* by incubation in a 96-well micro plate containing the reaction buffer and activated MMP-2. Concentration of the MMP-2 was varied in the range of 0.5 nM to 15 nM, NIRF emission recovery of the solution was measured after 2 h incubation at 37 °C and the measurement was achieved by Kodak imaging station with Cy5.5 excitation filter. As shown in Figure 4-3, the BCMG-SPION was able to recover NIRF signals against MMP-2 and a proportional relationship was observed between the MMP-2 concentration and the recovered NIRF signal. Recovered NIRF signal of BCMG-SPION against MMP-2 were detected at the sub-nanomolar enzyme level and these results show that PCM-CS has excellent sensitivity against MMP-2.

SCC7 tumor bearing xenografted mice were selected as the animal model for *in vivo* tumor imaging. The SCC7 cells were well-known tumor cell in terms of the high MMP-2 expression. *In vivo* imaging of

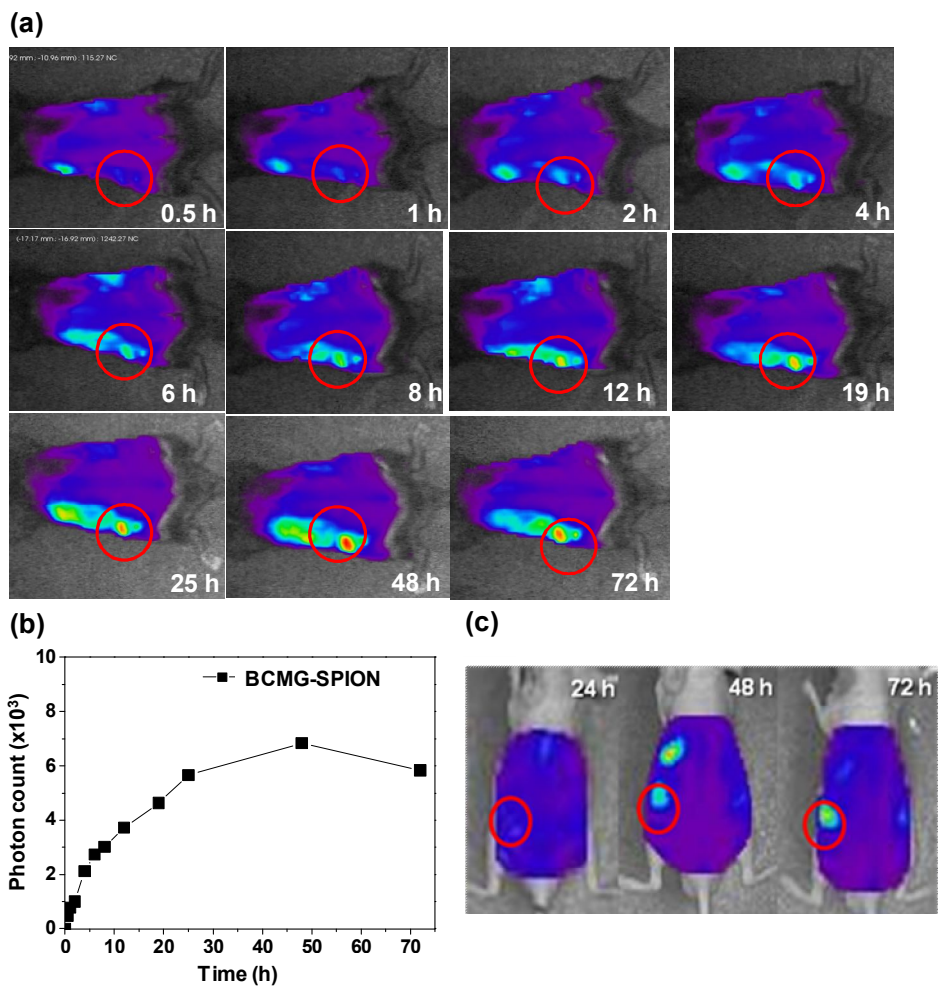
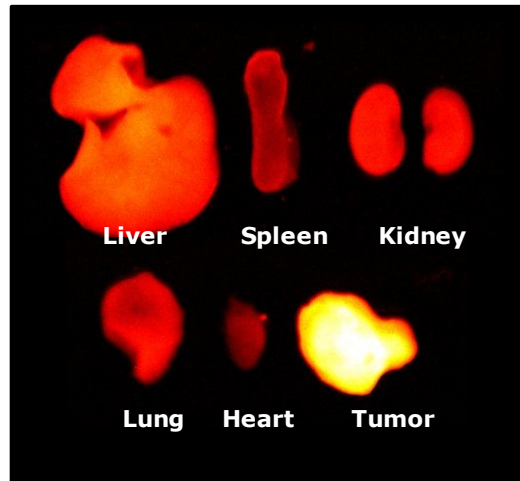


**Figure 4-4.** NIRF tomographic images of tumor-bearing mice after injection of (a) BCMG-SPION without inhibitor, (b) fluorescence intensity of tumor site and (c) BCMG-SPION with inhibitor (blue: low intensity, red: high intensity).

subcutaneous SCC7 tumor xenografted mice was performed at 3, 6, 12, 24, 48 and 72 h after injection of BCMG-SPION using the preclinical optical imaging system eXplore Optix, which was configured for NIRF fluorophore detection (excitation and emission at 670 and 700 nm, respectively). After injection of the probes into intravenous, the BCMG-SPION produced a high NIRF signal intensity and the maximum NIRF intensity was measured at 48 h post injection (Figure 4-4a, b). In particular, difference of NIRF signal was relatively higher than previously reported PEGylated nanoparticle based probe because glycol chitosan base nanoparticles have tumor targeting property. Tumors have relatively leaky vascular structure due to their abnormal cell growth rate and this phenomenon provides advantages such as enhanced accumulation of nano-sized particles in tumor tissue. Glycol chitosan based nanoparticles are suitable to pass through leaky vascular structure. Tumor contrast was significantly reduced with administration of the MMP-2 inhibitor, TIMP-2, because TIMP-2 blocked activation site of the MMP-2 and MMP-2 substrate in BCMG-SPION was not cleaved, consequently (Figure 4-4c). NIRF signal of inhibitor treated group was gradually increased after certain time because TIMP-2 was diffused out from the tumor tissue. These results show that BCMG-SPION has a potenti-

(a)



(b)

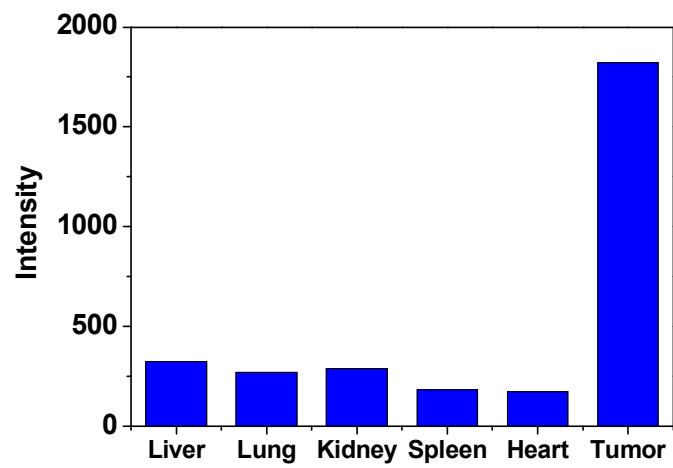


**Figure 4-5.** (a) NIRF images and (b) signal intensity of ROI of excised organs.

al application for in vivo tumor imaging and drug/protease activity screening.

NIRF images of excised organs from BCMG-SPION administered mice were evaluated by Kodak imaging station. Tumors excised from mice with administration of BCMG-SPION showed the highest NIRF signal than the liver, spleen, kidney, lung and heart. Intensity of the tumor was 8 times higher than other organs, and signal intensity of the liver was second due to the uptake in the RES system and non-specific degradation of the peptides. Figure 4-5 shows the NIRF images of each organs and the averaged signal intensity values of the ROI was used.

Magnetic resonance images were performed using same animal model, amount of particles and administration method. Human MRI scanner with 1.5 T magnetic fields was used to obtain MR images. Mice were imaged prior to injection of 0.1 mL BCMG-SPION at a concentration of 0.15 Fe mg/mL and MRI contrast enhancement and images were evaluated at various time points after administration. After injection of the BCMG-SPION, tumor site became darker and mean T2 signal intensity of the ROI was gradually decreased for 48 h because of the continuous accumulation of BCMG-SPION (Figure 4-6). Localization of the BCMG-SPION was calcul-

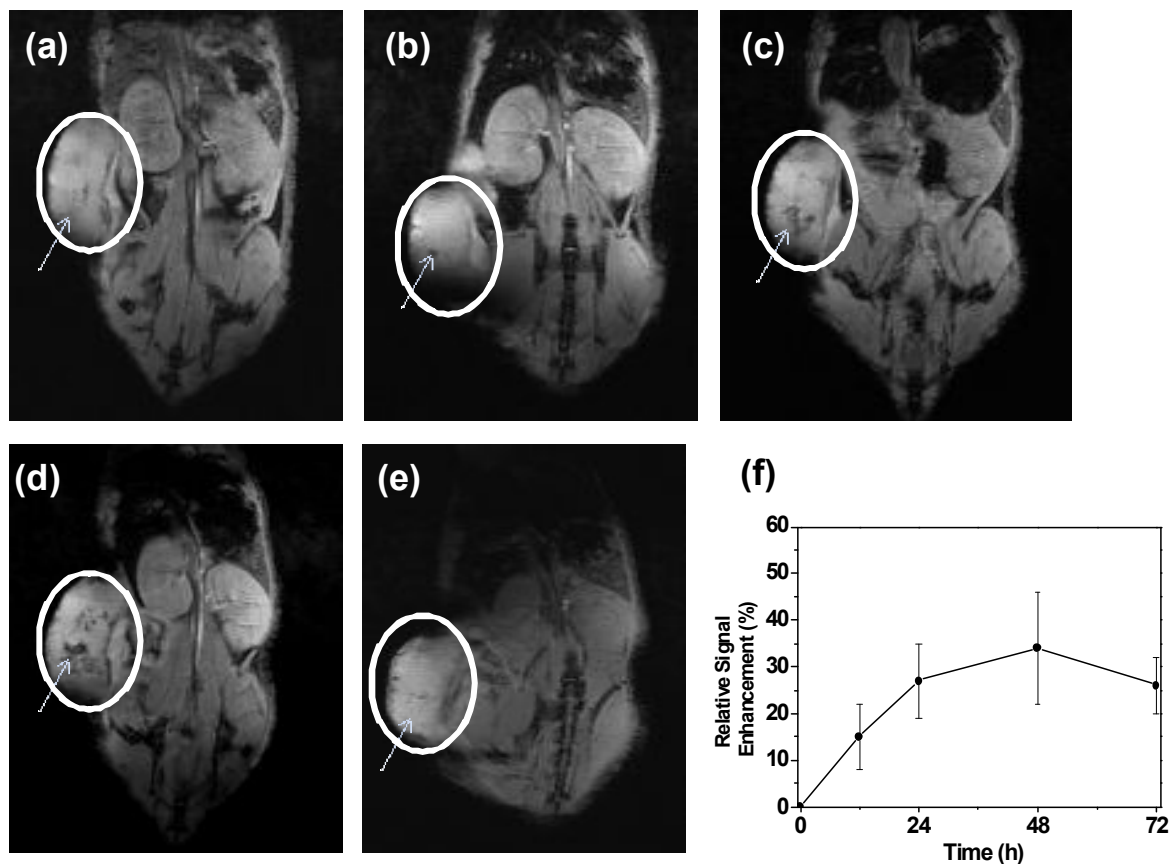


**Figure 4-6.** Magnetic resonance images of BCMG-SPION treated mice at various time points. (a) Pre-injection (b) 3 h, (c) 6 h, (d) 12 h, (e) 24 h post injection, and (f) relative signal enhancement of tumor regions.

-ated by comparing the contrast enhancement of the tumor site and the healthy muscle of the mice. Relative tumor contrast enhancement in the

T2 map was increased up to 34 %, higher than normal regions around the tumor, after 48 h post injection. T2 contrast enhancement was gradually decreased after 48 h after injection due to the removal of the BCMG-SPION from tumor site. According to previously reports, degradation of the dextran coated iron oxide nanoparticles was observed in intracellular endosome/lysosome between 3 to 5 days <sup>[21]</sup>. Considering these reports, decrease of the T2 contrast enhancement can be demonstrated in terms of metabolism of BCMG-SPION.

#### **4.4. Conclusion**

In this study, we introduced glycol chitosan coated iron oxide based nanoparticle which have activatable imaging modality and studied a potential for in vivo application of the probe. The tumor was successfully imaged by the probe using two different imaging modalities, NIRF optical imaging and MRI, and this probe can be used as a platform to any disease due to the disproportion of enzyme. The distinguished properties of our activatable dual imaging probe system set off its potential as a novel molecular imaging probe for optical imaging and MRI.

#### 4.5. References

- [1] O. Veiseh, C. Sun, C. Fang, N. Bhattarai, J. Gunn, F. Kievit, K. Du, B. Pullar, D. Lee, R. G. Ellenbogen, J. Olson, and M. Zhang, *Cancer Res.*, **2009**, *69*, 6200.
- [2] M. K. Yu, Y. Y. Jeong, S. J. Park, J. W. Kim, J. J. Min, K. W. Kim, and S. Jon, *Angew. Chem. Int. Ed.* **2008**, *47*, 5362.
- [3] S. Aime, M. Fasano, and E. Terreno, *Chem. Soc. Rev.* **1998**, *27*, 19.
- [4] K. M. Josephson L, Mahmood U, Tang Y, and Weissleder R, *Bioconjugate Chem.* **2002**, *13*, 554.
- [5] E.A. Schellenberger, R. Weissleder, and L. Josephson, *Bioconjugate Chem.* **2004**, *15*, 1062.
- [6] S. K. Mandal, B. Rotenberg, M. Tramier, J. Fattaccioli, J. Bibette, and B. Dubertret, *Langmuir* **2005**, *21*, 4175.
- [7] T. R. Sathe and S. Nie, *Anal. Chem.* **2006**, *78*, 5627.
- [8] W. P. Z. Medarova, Y. Kim, G. Dai, and A. Moore, *Int. J. Cancer* **2006**, *118*, 2796.
- [9] L. Zhang, S. Dong, *J. Phy. Chem. B* **2007**, *111*, 10448.
- [10] M. Mulder, G. J. Strijkers, D. P. Cormode, K. Nicolay, and Z. A. Fayad, *Nanomedicine* **2007**, *2*, 307.

- [11] K.Chen, H. Xu, D. Behera, M.H. Michalski, S. Biswal, A. Wang, and X.Chen, *Biomaterials* **2009**, *30*, 6912.
- [12] M. Ogawa, J. Seidel, M.V. Green, W. Xi, M. Williams, N. Kosaka, P.L. Choyke, and H. Kobayashi, *Bioconjugate Chem.* **2009**, *20*, 2177.
- [13] T. Nam, S.Y. Lee, K. Park, K. Choi, I.C. Song, M.H. Han, J.J. Leary, S.A. Yuk, I. C. Kwon, K. Kim, and S.Y. Jeong, *Bioconjugate Chem.* **2010**, *21*, 578.
- [14] T. S. C. Wong, J. Cui, J. Martin, V. P. Chauhan, W. Jiang, Z. Popovic, R.K. Jain, M.G. Bawendi, and ukumura, *Proc. Natl. Acad. Sci.* **2011**, *108*, 2426.
- [15] J. Xie, J. Huang, S. Lee, J. Wang, J. Gao, X. Li, and X. Chen., *Biomaterials* **2010**, *31*, 3016.
- [16] X. Yang, J. J. Grailer, I. J. Rowland, A. Javadi, S. A. Hurley, Y. Xiao, Y. Yang, Y. Zhang, R. J. Nickles , W. Cai, D.A. Steeber, and S. Gong, *Biomaterials* **2011**, *32*, 4151.
- [17] H. Y. Lee, Z. Li, K. Chen, A. R. Hsu, C. Xu, J. Xie, S. Sun, and X. Chen, *J. Nucl. Med.* **2008**, *49*, 1371.
- [18] Y. Lee, H. Lee, Y. B. Kim, J. Kim, T. Hyeon, H.W. Park, P. B. Messersmith, and T. G. Park, *Adv. Mater.* **2008**, *20*, 4154.

- [19] S. H. Crayton and A. Tsourkas, *ACS Nano* **2011**, *5*, 9592.
- [20] I.-C. Sun, D.-K. Eun, H. Koo, C.-Y. Ko, H.-S. Kim, D. K. Yi, K. Choi, I. C. Kwon, K. Kim, and C.-H Ahn, *Angew. Chem. Int. Ed.* **2011**, *50*, 9348.
- [21] D. Pouliquen, J.J. Le Jeune, R. Perdrisot, A. Ermias, and P. Jallet, *Magn. Reson. Imaging* **1991**, *9*, 275.

## **Chapter 5.**

### **Stabilized polymeric micelles by electrostatic interactions for drug delivery system**

## 5.1. Introduction

Nanocarriers of various bioactive agents are one of the most important topics in delivery systems. Several nanoparticle-based delivery systems, such as liposomes, solid lipid particles, self-assembled polymeric aggregates including micelles, inorganic and metal nanoparticles, have been developed to minimize the side effects encountered upon administration, and improve the biocompatibility and selective-targeting to the specific cells [1, 2].

Micelles, which are self-assembled nanostructures of amphiphilic block copolymers forming a hydrophobic core and hydrophilic outer shell, are a well studied drug carrier due to the advantages of efficiently encapsulating water insoluble drugs and excellent biocompatibility [3-8]. The hydrophobic nature of the micelle interior increases the drug solubility dramatically through hydrophobic-hydrophobic interactions [9-13], and prolongs the half-life of the encapsulated drugs in the blood stream due to the presence of a hydrophilic micelle outer shell, such as poly(ethylene glycol) (PEG), by preventing opsonization in the blood vessels and by effectively reducing the micelle clearance through the reticuloendothelial system<sup>[14-16]</sup>. In addition, micelles work as multi-modal drug carriers with

flexibility in introducing functional groups for specific targeting, increased cellular uptake and eventual enhancement of drug accumulation at the targeted place <sup>[14, 17, 18]</sup>.

The disadvantage of a polymeric micelle delivery system is the low structural stability in the blood stream due to the concentration-dependent characteristics represented by the critical micelle concentration (CMC), which has limited its applications as an in vivo drug carrier. Thermodynamically, micelles are disassembled into unimers at a concentration lower than the CMC. The injection of a micelle-based delivery system into the blood stream meets such a diluted condition <sup>[19, 20]</sup>. It is true that disassembly also takes place upon dilution even above the CMC with a decrease in the number of micelles, irrespective of the final concentration, but the disassembly proceeds slowly for the polymeric micelle system. A challenging approach to overcoming the stability problems is to chemically or physically crosslink the micelle structures. The shell crosslinked micelle is a representative of a chemically stabilized nanomaterials that resembles polymeric micelles in the spherical core-shell structures with the sites available for various modifications, such as specific binding and molecular recognition. At the same time, it behaves as a

unimolecular micelle to exhibit stability independent of the concentration [21-27]. Physical modification relies mainly on hydrophobic-hydrophobic or ionic interactions. The ionically-fixed polymeric nanoparticle system investigated by Lee et al. showed promising results on the preparation of water-insoluble anticancer drug carriers on a large-production scale [20]. A mixed micelle system was prepared using monomethoxy PEG-poly(lactide) diblock copolymers and the salt form of D, L-poly(lactic acid) upon the addition of divalent metal cations. The system showed excellent stability in vitro and efficient passive targeting to cancer sites.

Inspired by the mixed micelle approach, this study designed and synthesized amphiphilic copolymers and ionically stabilized the nanostructures for applications to a drug delivery system. The copolymer consisted of PEG, anionic oligopeptide and poly( $\epsilon$ -caprolactone) (PCL) blocks. Paclitaxel was used as the prototype drug. A new delivery system with improved stability avoiding the use of a toxic solvent was suggested. In vitro characterization was performed and its feasibility as a drug carrier was investigated.

## **5.2. Experimental**

**Materials.** Methoxy PEG amine (MW: 5,000, 95+ %) was purchased from Sunbio (Korea).  $\epsilon$ -Caprolactone (99 %), 4-nitrophenyl chloroformate (96 %), triphosgene (98 %), 2 M HCl in diethyl ether, calcium chloride anhydrous (96+ %), 1-methoxy-2-propanol (99.5+ %), palladium (10 wt % on activated carbon), chloroform-d (99+ %), dimethylsulfoxide-d<sub>6</sub> (99+ %) and anhydrous N,N-dimethylformamide (DMF, 99.9+ %) were obtained from Sigma-Aldrich (St. Louis, MO). L-Aspartic acid 4-benzyl ester (H-Asp(OBzl)-OH, 99 %) was commercially available from Bachem AG (Switzerland). Tetrahydrofuran (THF, 95 %) and n-hexane (95 %) were purchased from Daejung (Korea) and dried over sodium under nitrogen atmosphere. All other chemicals were commercially available and used as received.

**Instruments.** <sup>1</sup>H-NMR analysis was performed by Bruker Avance 300 MHz spectrometer in CDCl<sub>3</sub> or DMSO-d<sub>6</sub> at room temperature. Molecular weight and its distribution were determined by gel permeation chromatography using Shimadzu RID-10A refractometer detector with Styragel HR 3, HR 4, and HR 4E columns. THF was used as an eluent with the flow rate of 1 mL/min and polystyrene or PEG standards were used

for calibration. Measurement of particle size was carried out using Otsuka ELS-Z size analyzer equipped with He-Ne laser at a wavelength of 630 nm. UV-visible and fluorescent spectra were obtained by Shimadzu UV-1650 PC at the wavelength of 230 nm and by Shimadzu RF-500 spectrofluorophotometer, respectively. Average values of particle size, UV absorption and fluorescence were calculated with the data from three runs.

**Synthesis of L-aspartic acid N-carboxy anhydride (NCA).** Aspartic acid with benzyl ester protection group at the carboxylic acid side group, H-Asp(OBzl)-OH, was converted to corresponding N-carboxy anhydride as reported previously <sup>[1]</sup>. H-Asp(OBzl)-OH (2.00 g, 8.97 mmol), suspended in 20 mL anhydrous THF, was introduced to a 2-neck round bottom flask at room temperature and the reaction temperature was gradually increased to 55 °C. Triphosgene (1.32 g, 4.45 mmol), dissolved in 10 mL anhydrous THF, was added dropwise into the solution and the suspended mixture became clear solution with the formation of N-carboxy anhydrides. The reaction mixture was vigorously stirred for an additional 1 h to ensure the ring formation, condensed and poured into a 10-fold excess amount of anhydrous n-hexane to precipitate NCA. Aspartic acid N-carboxy

anhydride were obtained by filtration and dried in vacuum for 24 h (1.80 g, 82 %).

**Ring opening polymerization and activation of  $\epsilon$ -caprolactone.**  $\epsilon$ -Caprolactone (10.00 g, 87.72 mmol) was dissolved in 100 mL methylene chloride and introduced to a 2-neck round bottom flask. 1-Methoxy-2-propanol (0.48 g, 4.87 mmol) and 2 M HCl in diethyl ether (1 equiv mole to 1-methoxy-2-propanol) were added into the reaction mixture under nitrogen atmosphere using microsyringe<sup>[29]</sup>. Polymerization was continued at room temperature for 24 h. After the reaction was completed, the mixture was precipitated 2 times in cold n-hexane and the obtained PCL was dried under vacuum (8.07 g, 77 %).

PCL (5.38 g, 2.5 mmol), p-nitrophenyl chloroformate (0.56 g, 3 mmol) and 60 mL dried methylene chloride and introduced into a 100 mL 2-neck round bottom flask and stirred for 24 h at room temperature under nitrogen atmosphere. The reaction mixture was condensed, and poured into 500 mL cold n-hexane for precipitation. Activated PCL was obtained by filtration and dried in vacuum at 25 °C (4.7 g, 80 %). Molecular weight was 2,180 by <sup>1</sup>H NMR and 2,150 by GPC with the distribution,  $M_w/M_n$ , of

1.20.

**Synthetic procedure of block copolymer.** Aspartic acid NCA (0.40 g, 1.6 mmol) was dissolved in 25 mL anhydrous DMF and introduced to a 2-neck round bottom flask. Methoxy PEG amine (2.00 g, 0.4 mmol), dissolved in 5 mL anhydrous DMF, was added into the flask to initiate ring opening polymerization and the reaction was continued for 24 h at room temperature under nitrogen atmosphere. Different amount of aspartic acid NCA (0.25 g, 1.0 mmol) was reacted with methoxy PEG amine (0.50 g, 0.1 mmol) by same procedure mentioned above. Aliquots were taken for GPC analysis and the obtained molecular weight and  $M_w/M_n$  values were 6,200 / 1.16 and 7,680 / 1.21, respectively. mPEG-Asp(OBzl) which have four aspartic acid units was used in the experiments that follow.

Activated PCL (0.92 g, 0.4 mmol) was dissolved in 5 mL anhydrous DMF and added into the reaction mixture of mPEG-Asp(OBzl). After additional 24 h reaction, the product was precipitated in 10 folds excess amount of cold diethyl ether, filtered and dried under vacuum overnight at 25 °C (2.57 g, 78 %).

Deprotecting the ester-protection group in aspartic acid units

proceeded with polymer (2.00 g, 0.25 mmol) and Pd/C (10 wt % of polymer weight) in methylene chloride and the reaction mixture was stirred for 24 h under hydrogen pressure of 5 atm. After complete selective cleavage of benzyl ester in aspartic acid segment, Pd/C catalyst was filtered off through Celite. The solution was poured into the cold diethyl ether to precipitate polymer, mPEG-Asp-PCL, and remove by-products. The product was dried overnight under reduced pressure at 25 °C (1.12 g, 59 %). Molecular weight and the distribution,  $M_w/M_n$ , of the copolymer was 8,930 and 1.22 by GPC.

**Micelle formation and ionic stabilization.** Accurately weighed polymer, mPEG-Asp-PCL, was dissolved in 1 mL acetonitrile and transferred to a pre-swollen dialysis membrane with the molecular weight cut off of 3.5K. The solution was dialyzed against double distilled water for 2 days and micelles were obtained by lyophilization for 3 days. The obtained micelles were re-dissolved in 5 mL distilled water and sonicated for 24 h.

Ionically stabilized micelle was prepared by adding 20 times molar excess of calcium chloride to carboxyl groups of aspartic acid in distilled

water to the micelle solution, followed by stirring for 24 h at 37 °C. The solution was passed through a 0.22 micrometer filter to remove unloaded drug aggregates and dust in the micelle solution.

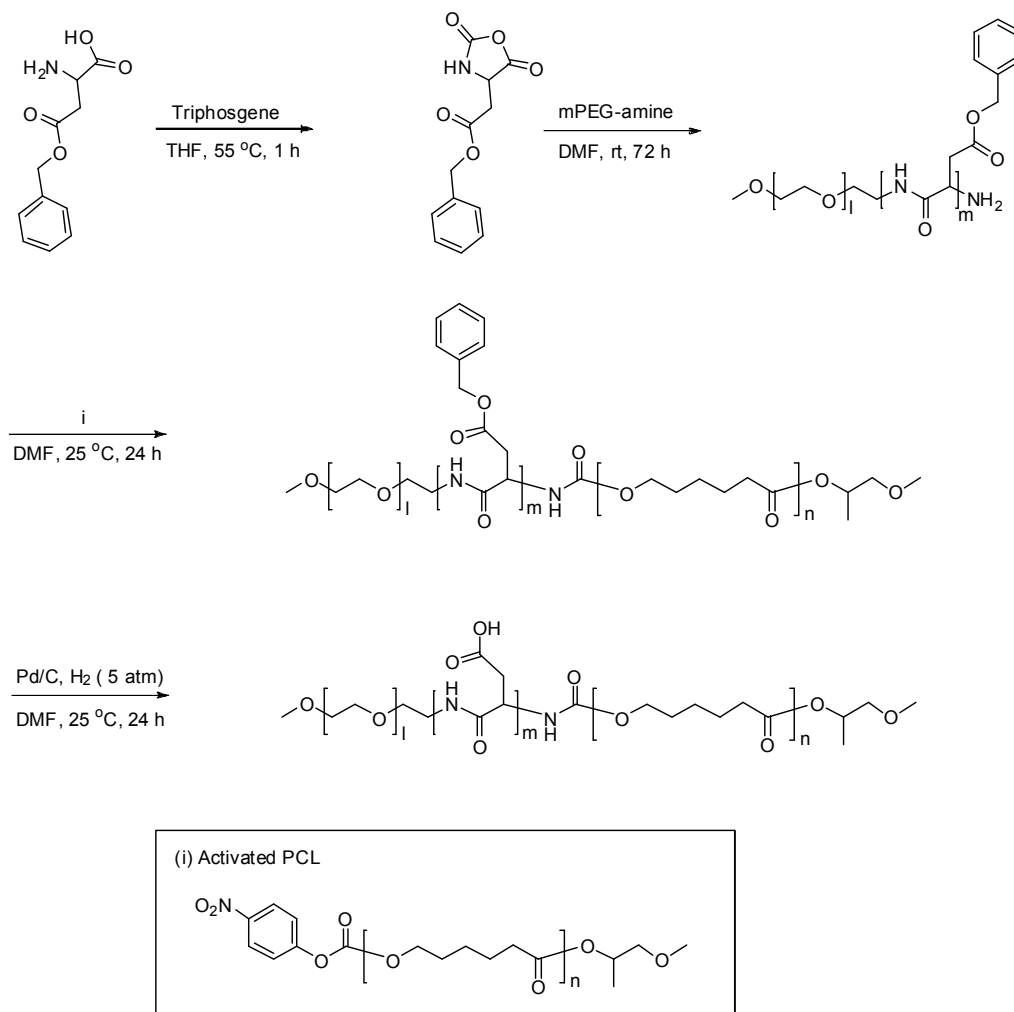
**Paclitaxel encapsulation and determination of in vitro release profile.** Accurately weighed polymer and paclitaxel of 20 wt. % to the polymer were dissolved in 1 mL acetonitrile. Paclitaxel-encapsulated micelles and stabilized micelles in distilled water were produced using the same procedure described above. 1 mL aliquot of paclitaxel loaded micelles and stabilized micelles were taken from the prepared solutions and each solution was diluted using 5 mL of DMSO. UV absorbance of diluted solutions was measured at the wavelength of 230 nm for determining the amount of loaded paclitaxel.

1 mL of freshly prepared paclitaxel loaded micelles was placed in a pre-swollen cellulose dialysis membrane with the molecular weight cut off of 3.5K. At every 2 h, 1 mL aliquot was taken from the media, phosphate buffer saline with 0.1 wt% of Tween 80, and the media was changed. The amount of released paclitaxel was measured by same procedure described above using Shimadzu UV-1650 PC at the wavelength of 230 nm.

**Determination of critical micelle concentration.** Polymer, mPEG-Asp-PCL, was dissolved in 5 ml double distilled water in different concentrations from 1.0 mg/ml to  $1.0 \times 10^{-5}$  mg/ml, and then 5 ml of  $1.2 \times 10^{-6}$  M pyrene solution was added to each sample. The solution was sonicated at room temperature for 2 h and the formation of micelles was induced for an additional 24 h. The emission intensities at 373 and 383 nm were determined by Shimadzu spectrofluorophotometer with the excitation wavelength set at 339 nm. The critical micelle concentration was determined as the intercept of the two lines extrapolated from the points before and after the relative emission fluorescence intensity ratio of 373/383 began to change <sup>[30]</sup>.

### 5.3. Results and Discussion

An amphiphilic copolymer comprising anionic aspartic acid oligomers ring-opening polymerization of aspartic acid NCA (Scheme 5-1) with amino methoxy PEG macroinitiators with a molecular weight of 5K, followed by a coupling reaction with activated PCL. The reactions were carried out in



**Scheme 5-1.** Synthetic procedure of mPEG–Asp–PCL.

situ in order to minimize the oxidation of amino groups at the distal end of mPEG-Asp(OBzl). Scheme 5-1 shows the synthetic procedure to produce mPEG-Asp-PCL, methoxy poly(ethylene glycol)-block-oligo(L-aspartic

acid)-block-poly( $\epsilon$ -caprolactone). Experiments using the two monomer/initiator ratios were performed and the number of aspartic acid groups was adjusted with a narrow distribution by controlling the monomer to initiator molar ratio (Table 5-1). The number of aspartic acid units, Asp(OBzl), in the copolymer was determined by  $^1\text{H-NMR}$  spectroscopy based on the relative peak integration ratio between the methylene protons of mPEG around 3.5 ppm and those of benzyl ester at 5.2 ppm (Figure 5-1)<sup>[31]</sup>. The polymer with four aspartic acid units was used for further experiments. The amphiphilic copolymers with carboxylic acid groups at the junction between the hydrophilic PEG and hydrophobic PCL blocks were obtained by selectively cleaving the benzyl ester protecting groups in the aspartic acid units without degrading the ester bonds in the PCL blocks<sup>[32]</sup>.

**Table 5-1.** Adjustment of the number of aspartic acids.

Amount of initiators (g)	Amount of monomers (g)	Molar ratio of monomer/initiator	Molar ratio of monomer/initiator by NMR	Molecular weight and PDI of polymers
2.00	0.40	4.00	3.92	6200 (1.16)
0.50	0.25	10.01	9.00	7680 (1.21)

<sup>a</sup> Molecular weight and PDI were determined by GPC.

Palladium, 10 wt % on activated carbon, was used as a catalyst for hydrogenolysis, and the selective cleavage was confirmed by the disappearance of the benzyl ester peak at 7.2 – 7.4 ppm and by the intact integration ratios of the other groups. Figure 5-2 shows a representative <sup>1</sup>H-NMR spectra of the final product of mPEG-Asp-PCL. The GPC traces in Figure 5-3 support the successful oligomerization, coupling and deprotection reactions. A shift of the peak molecular weight before and after the coupling reaction without noticeable shoulders in the trace indicated the successful formation of a block copolymer and the complete separation of unreacted starting polymers.

Figure 5-4 shows the size and its distributions determined by light scattering. Polymeric micelles were formed by the dialysis of mPEG-Asp-PCL block copolymers in acetonitrile against double distilled water at room temperature. The micelles had a mean diameter of 73.0 nm based on the intensity-averaged values by dynamic light scattering. The non-stabilized micelles were stabilized by an electrostatic interaction between the carboxylic acid groups in the copolymers and divalent metal cations to overcome the structural instability of the micelles in the blood stream. Calcium was chosen as the stabilizing metal over zinc or magnesium

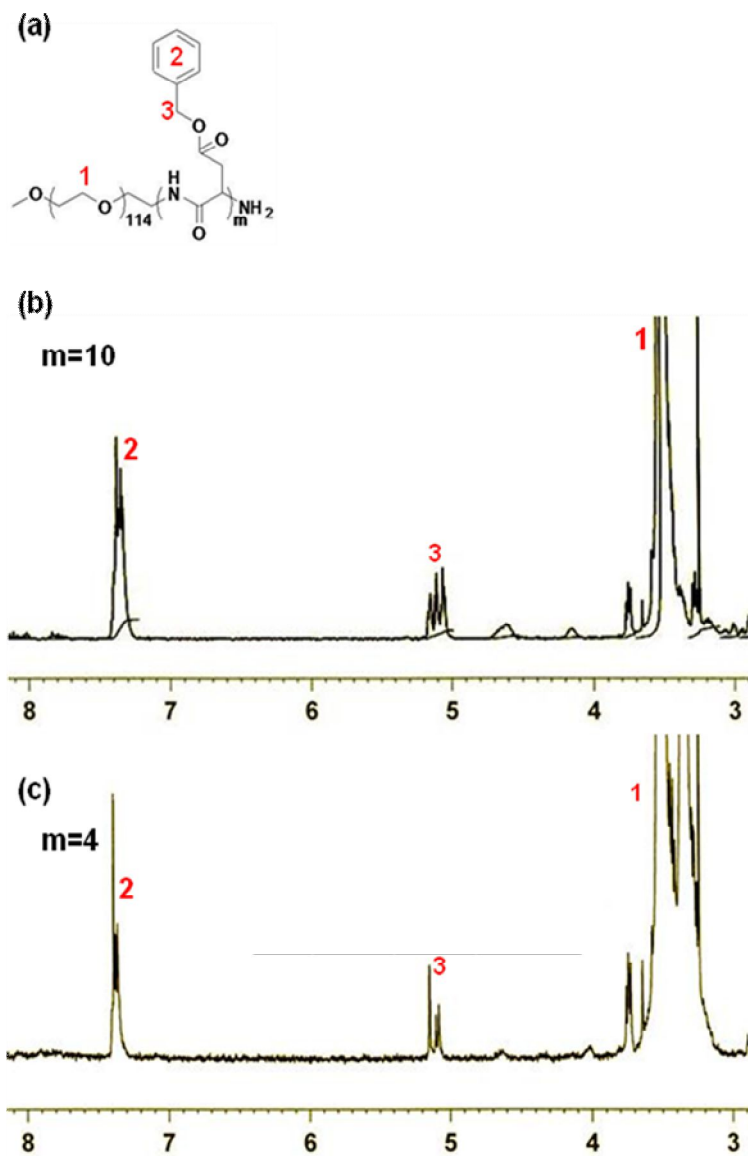


**Figure 5-1.** Chemical structure and  $^1\text{H-NMR}$  spectra of mPEG-Asp(OBzl) in  $\text{CDCl}_3$ : (a) chemical structure; (b), (c)  $^1\text{H-NMR}$  spectra.

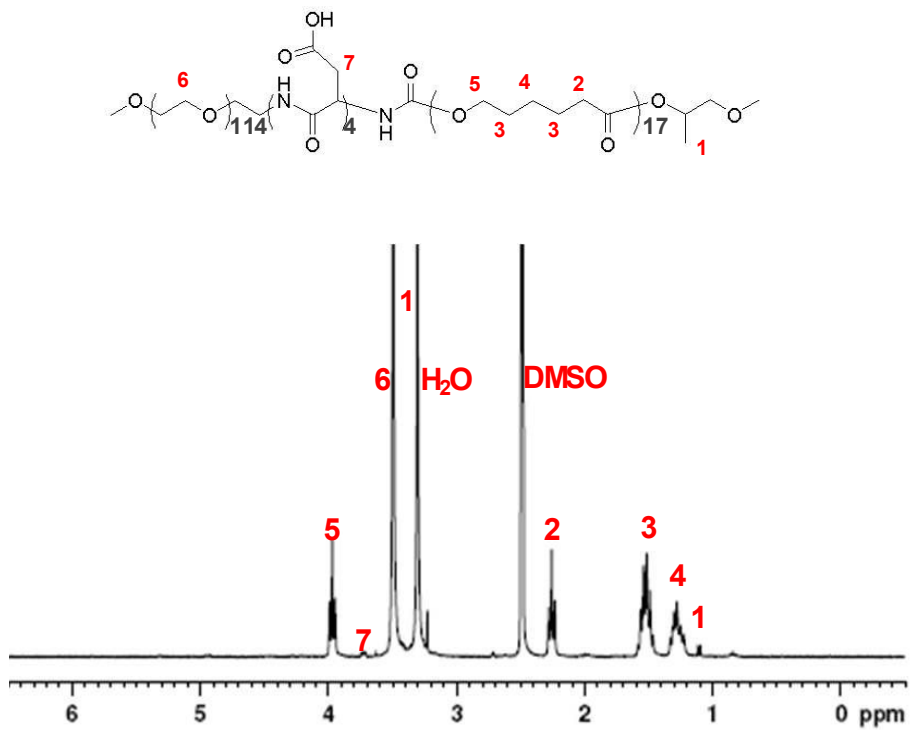


**Figure 5-2.** <sup>1</sup>H NMR spectra of mPEG-Asp-PCL in DMSO-d<sub>6</sub>.

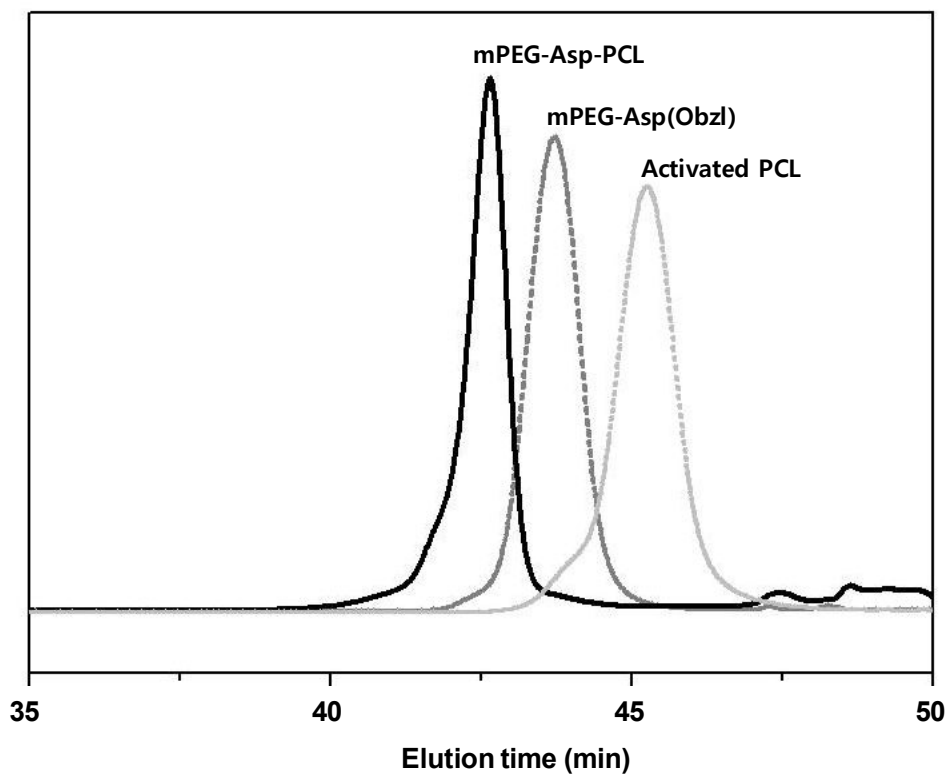


**Figure 5-3.** GPC traces of activated PCL, mPEG–Asp(OBzl) and mPEG–Asp–PCL using THF as an eluent.

because of its biosafety and the relatively large body requirement for calcium compared to other inorganic components <sup>[20]</sup>. A mean diameter of 70.4 nm was observed, which suggests that ionic stabilization did not have a significant effect on the micelle size. Paclitaxel, a hydrophobic anticancer drug, was encapsulated by addition to the polymer solution before the self-assembly process. Experiments using a range of polymer-to-paclitaxel ratios were performed to determine the optimal loading amount.

According to these results, a drug/polymer ratio of 20 % was used in the further experiments. The paclitaxel-loading and ionic fixation caused an increase in micelle size to 87 nm and 96 nm, respectively. The size of the drug-loaded and stabilized micelles is still within the range that can be used as passively targeting drug carriers, where nano-sized carriers ranging from 5 nm to 200 nm are desirable for a long term blood circulation by avoiding renal and RES clearance, and for subsequent selective tumor accumulation based on the EPR effect. Compared to the conventional polymeric micelles, the ionically stabilized micelles showed improved stability in aqueous solution even at a low polymer concentration. The CMC of mPEG-Asp-PCL copolymer was determined to be 0.078 mg/mL using fluorophotometer with pyrene as a model drug (Figure 5-5).

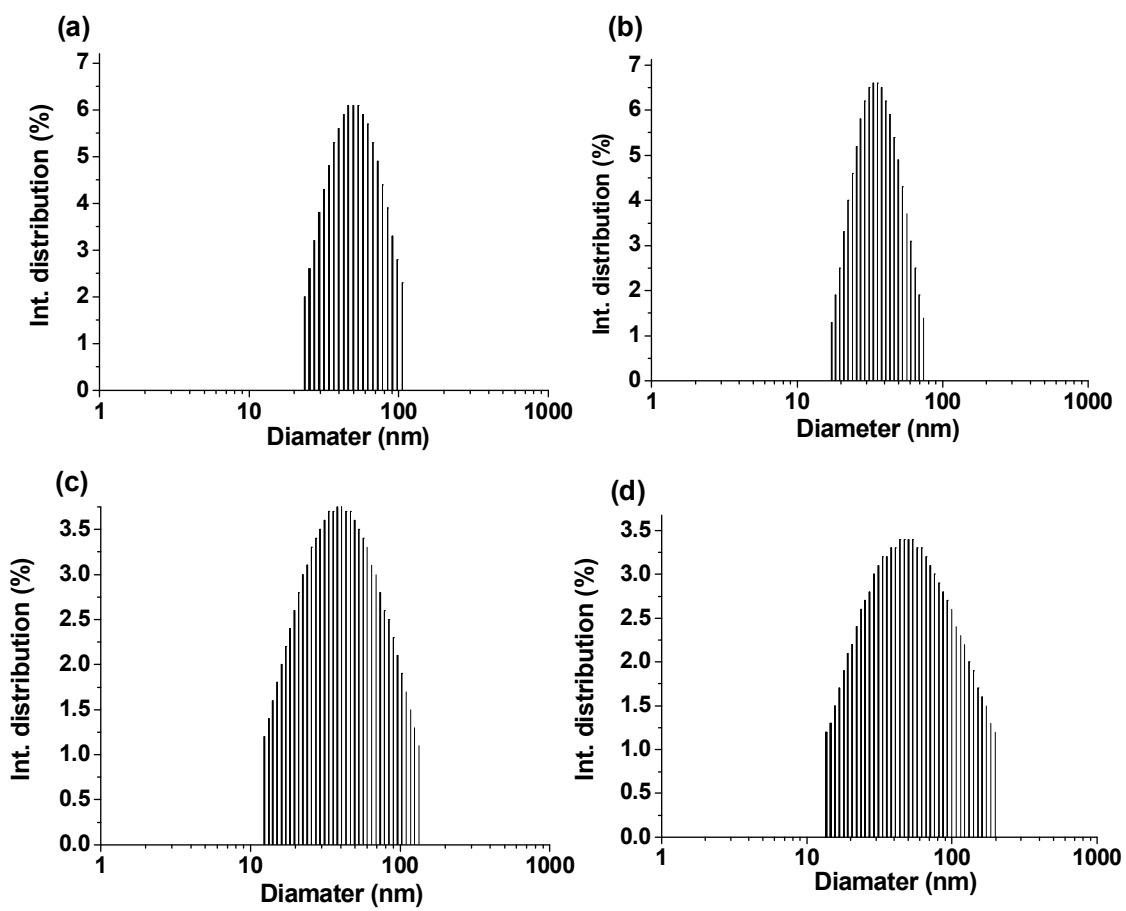


**Figure 5-4.** Size distribution of (a) non-stabilized micelle; (b) ionically stabilized micelle; (c) paclitaxel-loaded micelle; (d) ionically stabilized and paclitaxel-loaded micelle.

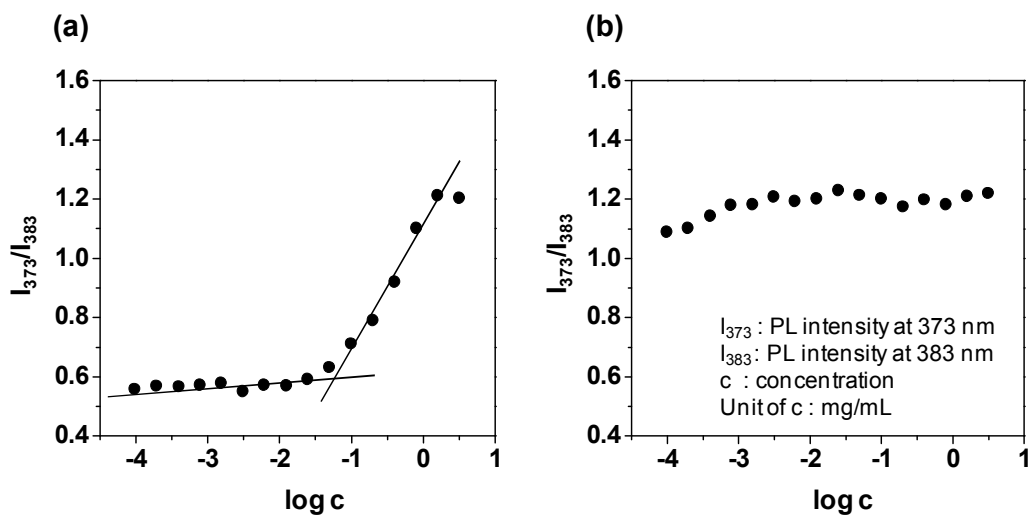


**Figure 5-5.** Ratio of intensity at 373 nm and 383 nm of pyrene emission spectra as a function of log concentration; (a) non-stabilized micelle; (b) stabilized micelle.

Figure 5-6 shows images of paclitaxel loaded micelle solutions with and without ionic stabilization at different concentrations. The clear and transparent solution at 2.00 mg/mL in Figure 5-6a demonstrated micelle formation above the CMC independently of ionic stabilization, which increased the solubility of paclitaxel in the inner core of the micelles. At a concentration below the CMC, 0.02 mg/mL, micelles without ionic stabilization dissociated into polymeric unimers and lost their capacity to

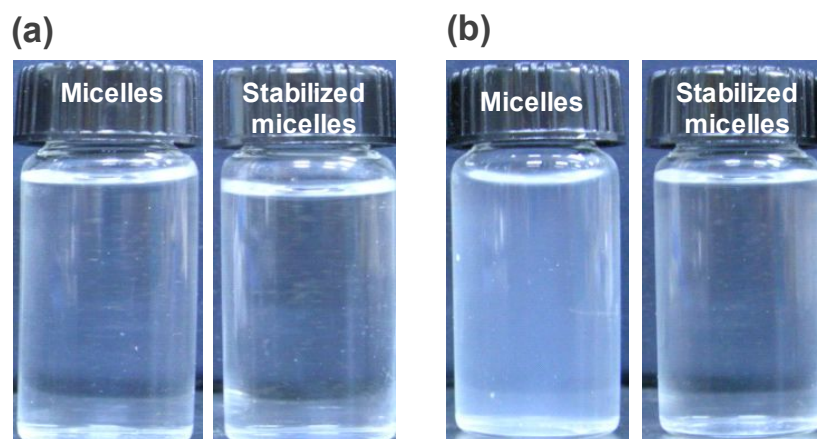


**Figure 5-6.** Pictures of non-stabilized and ionically stabilized micelle solution at the concentration of (a) 2.0 mg/mL above CMC, and (b) 0.02 mg/mL below CMC.

encapsulate the hydrophobic drugs, which resulted in an opaque, phase-separated solution after sonication, as shown in Figure 5-6b. On the other hand, no disintegration was observed with the stabilized micelles under the same conditions, which confirms the improved stability through ionic stabilization regardless of the concentration.

The paclitaxel-loading and efficiency into the micelles were 8.7 % and 47.6 %, respectively. The effect of ionic stabilization on the drug-loading was not obvious but its effect on the release behavior was clear, producing a typical two-phase-release profile. As shown in Figure 5-7,

rapid releases of approximately 65 % of the paclitaxel encapsulated by the non-stabilized micelle were observed, and a relatively small portion, approximately 45 %, from the ionically stabilized micelle was observed in the first 24 h at pH 7.4 in PBS solution containing 0.1 wt % of Tween 80, which is a low molecular weight surfactant that enhances the solubility of paclitaxel in water. The sustained and slow release over a prolonged period, up to two weeks, was observed in the ionically stabilized micelles after the rapid release. In contrast, the profile from the non-stabilized micelles reached a plateau at approximately 75 % of accumulated paclitaxel release after 50 h. The sustained release by the ionic interaction was probably due to the presence of stabilized layers between the inner core and outer shell caused by electrostatic interactions between the carboxylic acid groups and divalent calcium cations. The enhanced micelle stability independent of the concentration as a result of electrostatic interactions highlights a way of preparing a long circulating delivery system encapsulating water-insoluble drugs.

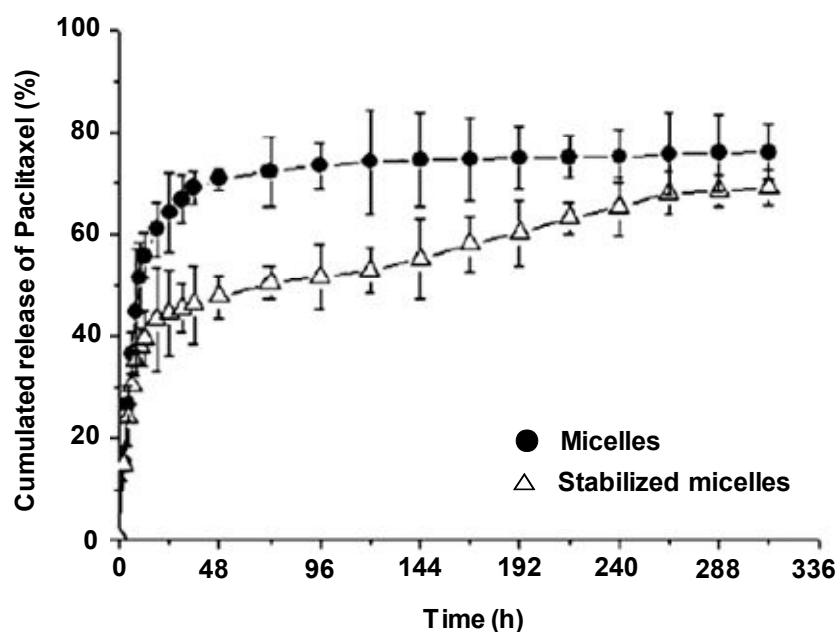


**Figure 5-7.** In vitro paclitaxel release profiles from non-stabilized micelles (●) and ionically stabilized micelles (△) in aqueous medium at 37 °C.

#### 5.4. Conclusion

A novel polymeric micelle composed of anionic oligomers between amphiphilic blocks was synthesized, and its stability was evaluated after adding divalent calcium cations to form stabilized layers at the junction of the blocks based on an electrostatic interaction. The ionically-stabilized micelles showed improved stability in aqueous solution regardless of the

concentration and no critical micelle concentration was observed. Paclitaxel was encapsulated into the micelles and its loading-releasing behavior was examined in the presence and absence of ionic stabilization. The paclitaxel-loaded stabilized micelles exhibited a typical two-phase-release profile, a stage with burst effect followed by slow and sustained release over two weeks. In contrast, the non-stabilized micelles without ionic stabilization continued to release the drug at a similar rate as the first burst phase reaching a plateau. Ionically stabilized micelles with structural stability are a promising material for the development of polymeric nano-carriers that are applicable to in vivo drug delivery systems.

## 5.5. References

- [1] S. Cohen, H. Bernstein, *Microparticulate Systems for the Delivery of Proteins and Vaccines*, Marcel Dekker, New York, 1996.
- [2] H. Muller, *Colloidal Carriers for Controlled Drug Delivery and Targeting: Modification, Characterization, and In Vivo Distribution*, Wissenschaftliche Verlagsgesellschaft, Stuttgart, 1991.
- [3] V. P. Torchilin and V. S. Trubetskoy, *Adv. Drug Deliv. Rev.* **1995**, *16*, 141.

- [4] D. D. Lasic, F. J. Martin, *Stealth Liposomes*, CRC, Boca Raton, Florida, 1995.
- [5] D. D. Lasic, *Nature* **1992**, 355, 279.
- [6] M. Jones, J. Leroux, *Eur. J. Biopharm.* **1999**, 48, 101.
- [7] A. T. Florence, Chapman & Hall, London, 1983
- [8] P. H. Elworthy, A. T. Florence, C. B. Macfarlane, Chapman & Hall, London, 1968.
- [9] O. Soga, C. F. v. Nostrum, M. Fens, C. J. Rijcken, R. M. Schiffelers, G. Storm, W. E. Hennink, *J. Control. Release* **2005**, 103, 341.
- [10] J. E. Chung, M. Yokoyama, M. Yamato, T. Aoyagi, Y. Sakurai, and T. Okano, *J. Control. Release* **1999**, 62, 115.
- [11] J. E. Chung, M. Yokoyama, T. Aoyagi, Y. Sakurai, and T. Okano, *J. Control. Release* **1998**, 53, 119
- [12] A. Benahmed, M. Ranger, and J. C. Leroux, *Pharm. Res.* **2001**, 18, 323.
- [13] J. E. Chung, M. Yokoyama, and T. Okano, *J. Control. Release* **2000**, 65, 93.
- [14] D. Sutton, N. Nasongkla, E. Blanco, and J. Gao, *Pharm. Res.* **2007**, 24, 1029.

- [15] G. S. Kwon, M. Yokoyama, T. Okano, Y. Sakurai, and K. Kataoka, *J. Control. Release* **1994**, 28, 334.
- [16] K. Kataoka, G. S. Kwon, M. Yokoyama, T. Okano, and Y. Sakurai, *J. Control. Release* **1993**, 24, 119.
- [17] R. Gref, Y. Minamitake, M. T. Peracchia, A. Domb, V. Trubetskoy, V. Torchilin, and R. Langer, *Pharm. Biotechnol.* **1997**, 10, 167.
- [18] R. T. Liggins, and H. M. Burt, *Adv. Drug Deliver. Rev.* **2002**, 54, 191.
- [19] K. Avgoustakis, A. Beletsi, Z. Panagi, P. Klepetsanis, E. Livaniou, G. Evangelatos, D. S. Ithakissios, *Int. J. Pharm.* **2003**, 259, 115.
- [20] S.-W. Lee, D.-H. Chang, M.-S. Shim, B.-O. Kim, S.-O. Kim, and M.-H. Seo, *Pharm. Res.* **2007**, 24, 1508.
- [21] R. K. O'Reilly, C. J. Hawker, and K. L. Wooley, *Chem. Soc. Rev.* **2006**, 35, 1068.
- [22] S. W. Hong, K. H. Kim, J. Huh, C.-H. Ahn, and W. H. Jo, *Macromol. Res.* **2005**, 13, 397.
- [23] A. M. Nystrom, Z. Xu, J. Xu, S. Taylor, T. Nittis, S. A. Stewart, J. Leonard, and K. L. Wooley, *Chem. Commun.* **2008**, 30, 3579.
- [24] A. N. Koo, H. J. Lee, S. E. Kim, J. H. Chang, C. Park, C. Kim, J. H. Park, and S. C. Lee, *Chem. Commun.* **2008**, 48, 6570.

- [25] J. Sun, X. Chen, T. Lu, S. Liu, H. Tian, Z. Guo, and X. Jing, *Langmuir* **2008**, *24*, 10099.
- [26] Z. Yang, S. Zheng, W. J. Harrison, J. Harder, X. Wen, J. G. Gelovani, A. Qiao, and C. Li, *Biomacromolecules* **2007**, *8*, 3422.
- [27] Y. Chan, T. Wong, F. Byrne, M. Kavallaris, and V. Bulmus, *Biomacromolecules* **2008**, *9*, 1826.
- [28] T. J. Deming, *Adv. Mater.* **1997**, *9*, 299.
- [29] Y. Shibasaki, H. Sanada, M. Yokoi, F. Sanda, T. Endo, *Macromolecules* **2000**, *33*, 4316.
- [30] P. Goona, C. Manoharb, and V. V. Kumara, *J. Colloid Interface Sci.* **1997**, *189*, 177.
- [31] H. R. Kricheldorf,  *$\alpha$ -Aminoacid-N-carboxyanhydrides and Related Materials*, Springer, New York 1987.
- [32] S.-H. Yim, J. Huh, C.-H. Ahn, and T. G. Park, *Macromolecules* **2007**, *40*, 205.

## **Chapter 6.**

**pH sensitive drug delivery system using  
ionically stabilized polymeric micelles**

## 6.1. Introduction

Micelles, self-assembled nanostructures in a selective solvent, have been investigated as a drug delivery carrier of hydrophobic water-insoluble drugs. A variety of amphiphilic copolymers were used for micelle formation and the issues of biocompatibility limited the selection of polymers in medical applications. For the hydrophilic block, the most widely investigated polymer is PEG due to its excellent solubility in water as well as in organic solvents, and non-toxic characteristics. Biodegradable polymers, such as poly(lactic- co-glycolic acid) (PLGA), poly( $\epsilon$ -caprolactone) (PCL), poly( $\beta$ -amino ester) and polypeptides, are considered for the hydrophobic core according to the delayed hydrolysis depending on the degree of hydrophobicity and enzyme-catalyzed degradations <sup>[1-10]</sup>. Micelles are not so stable in the bloodstream due to the presence of the critical micelle concentration. Chemical cross-linking at the core or the shell of the micelles as well as physical stabilization through hydrophobic or ionic interactions were proposed to overcome the instability of the micelles under the physiological conditions.

Doxorubicin is one of the most common chemotherapeutic agents that possess high anti-tumor activity for the treatment of various cancers. From

previous studies, doxorubicin is reported to interact with DNA by intercalation and inhibit the progression of the enzyme topoisomerase II, which unwinds DNA for transcription [11-13]. Doxorubicin also gives rise to strong side effects such as dilated cardiomyopathy, congestive heart failure and heart arrhythmias. In order to reduce these side effects and to enhance the therapeutic efficacy, formulation of doxorubicin with various delivery carriers has been investigated [14-16].

Our group reported the development of paclitaxel delivery system using ionically stabilized micelles composed of biocompatible PEG, anionic oligopeptide and PCL [17]. In this study, doxorubicin was encapsulated into the same delivery system based on the electrostatic interaction between doxorubicin and anionic carriers, since doxorubicin is positively charged due to the partially protonated primary amines under the physiological conditions. The pH dependent release behavior was investigated in the presence and the absence of cationic metal stabilization..

## **6.2. Experimental**

**Materials.** L-Aspartic acid 4-benzyl ester (99%) was available from Bachem AG (Switzerland) and methoxy PEG amine with a molecular

weight of 5 K was purchased from Sunbio (Korea).  $\epsilon$ -Caprolactone (99%), calcium chloride anhydrous (96+%) and palladium (10 wt% on activated carbon) were obtained from Sigma-Aldrich (St. Louis, MO). Tetrahydrofuran (95%) and n-hexane (95 %) were purchased from Daejung (Korea) and dried over sodium under nitrogen atmosphere. All other chemicals were commercially available and used as received.

**Synthesis and Characterization of mPEG-Asp-PCL Copolymer and Micelles.** Detailed synthetic procedures and characterizations of the mPEG-Asp-PCL copolymer and its micelle formation were described in Chapter 5.

**Instruments.** Measurement of particle size and zeta potential were carried out using Otsuka ELS-Z instrument equipped with He-Ne laser at a wavelength of 630 nm. UVvisible and fluorescent spectra were obtained by Shimadzu UV-1650 PC at the wavelength of 230 nm and by Shimadzu RF-500 spectrofluorophotometer, respectively. Average values of particle size, UV absorption and fluorescence were calculated with the data from three runs.

**Doxorubicin Encapsulation and Micelle Stabilization.** 25.0 mg mPEG-Asp-PCL and 10.0 mg doxorubicin were dissolved in 1 mL acetonitrile and dialyzed against deionized water for 24 h using a pre-swollen dialysis membrane with a molecular weight cut off of 3.5 K. The solution was lyophilized for 2 days and obtained micelles were re-dispersed in 4.0 mL deionized water and sonicated for 24 h. Ionic stabilization of doxorubicin encapsulated micelle was performed with vigorous stirring by dropwise addition of 1.0 mL calcium chloride solution (1.0 M) to prepared doxorubicin encapsulated micelle solutions, followed by 24 h stirring at 37 °C. The solution was filtered through a 0.22 µm filter to remove unloaded doxorubicin aggregates, if present, and dusts in the micelle solution. The amount of doxorubicin was determined using UV absorbance measurement at the wavelength of 480 nm. For determining of drug loading amount, 1.0 mL doxorubicin loaded micelles and stabilized micelles were diluted using 5.0 mL DMSO and analyzed by UV-Vis spectroscopy.

**Determination of in vitro Release Profile.** The release profiles of doxorubicin from ionically stabilized micelles were obtained by dialysis method using dialysis membrane with the molecular weight cut off of 3.5 K

at 37 °C. 1 mL doxorubicin encapsulated micelle solutions were dialyzed against 20.0 mL fresh medium (phosphate buffer, 50 mM, pH 7.4) and 5.0 mL aliquot was taken from medium for analysis at every 2 h. In order to acquire sink conditions, the medium was replenished with the same volume of fresh medium every 2 h. The amount of released doxorubicin was determined by UV absorbance measurement at the wavelength of 480 nm. The release profiles of doxorubicin from non-stabilized micelles were evaluated using dialysis membrane with the molecular weight cut off of 3.5 K at 37 °C in two different stages. Doxorubicin release was performed with neutral medium in phosphate buffer at pH 7.4 for 24 h and the medium was changed to acidic medium. The acidic medium was prepared by titration of phosphate buffer using 0.1 M citric acid. At every 2 h sampling, the pH value of the medium was checked to maintain the pH of 3.0. The same procedure mentioned above was used for determining the amount of released doxorubicin. Average value of the released drug was reported with the data from three runs.

### **6.3. Results and Discussion**

Synthesis of the copolymer composed of hydrophilic PEG, negatively

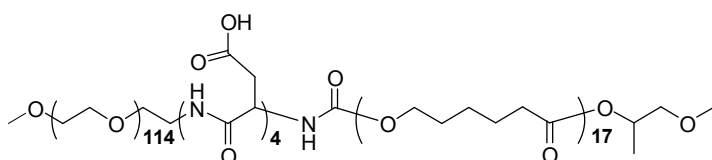
charged aspartic acid oligomer and hydrophobic PCL was described in chapter 5 <sup>[17]</sup>. Methoxy PEG-NH<sub>2</sub> with a molecular weight of 5 K initiated the ring-opening polymerization of aspartic acid N-carboxy anhydrides and followed was an in-situ coupling reaction between activated PCL blocks and mPEG-Asp(OBzl) terminated with primary amines. The mPEG-Asp-PCL copolymer was characterized to have 4 aspartic acid residues on average by <sup>1</sup>H NMR analysis. The molecular weight and M<sub>w</sub>/M<sub>n</sub> were 8.9 K of 1.22, respectively, as determined by GPC <sup>[17]</sup>. Figure 6-1a shows the chemical structure of the obtained copolymer. The copolymers were self-assembled into nanostructures in the aqueous condition and dynamic light scattering measurement produced an intensity-averaged diameter of 73.0 ± 30.6 nm, which was still within the range that could be claimed as micelles. The zeta potential of the intact micelles in aqueous solution was -2.3 mV because of the negatively charged aspartic acid residues between the two block copolymers. The critical micelle concentration of the copolymer was 0.078 mg/mL and the concentration-independent stability of the micelles was proved by stabilizing micelles with divalent calcium cations <sup>[17]</sup>.

Doxorubicin was encapsulated into the micelles as described in the previous experimental section. Addition of divalent calcium cations

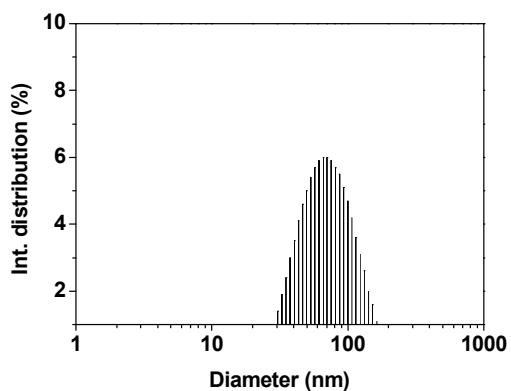
stabilized the drug-loaded micelles using ionic interactions with negatively charged aspartic acids at the interface between hydrophilic and hydrophobic blocks. As shown in Figure 6-1b and 6-1c, the intensity-averaged diameter of the drug loaded micelles and the stabilized micelles by calcium was  $75.8 \pm 26.2$  nm and  $78.1 \pm 24.3$  nm, respectively. The zeta potential of the drug loaded micelles and the stabilized micelles were +2.1 mV and +6.4 mV, respectively. The doxorubicin-loading amount was 15.1 %, which was calculated using the percentage weight of the encapsulated drug divided by the total weight of the drug and the copolymer. The drug loading efficiency into the micelles was 44.5%. Almost the same values of the doxorubicin loading amount and efficiency were obtained for the ionically stabilized micelles, which indicated that ionic stabilization did not make a significant influence on the micelle size as well as the drug-loading behavior.

Release patterns of doxorubicin were examined from the micelles with and without ionic stabilization under the physiological conditions. Figure 6-2 shows the release profiles. Previous study with paclitaxel reported the typical two-phase release patterns. Observed were the rapid paclitaxel releases of 65% from the non-stabilized micelle and 45% from the stabilized micelle in the first phase. The stabilized micelles then showed a

(a)



(b)



(c)

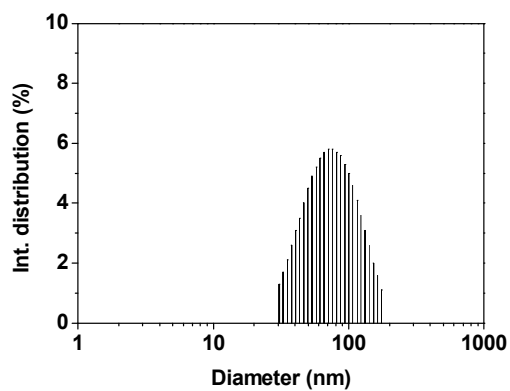


**Figure 6-1.** (a) Chemical structure of mPEG-Asp-PCL. Size distribution of (b) doxorubicin-loaded micelle; (c) ionically stabilized doxorubicin-loaded micelle.

sustained release profile over 2 weeks, whereas the profile reached a plateau at 75% after 50 h from the non-stabilized micelles <sup>[17]</sup>. Positively charged doxorubicin displayed totally different release patterns compared to the neutral paclitaxel. The typical two-phase doxorubicin release profile was observed from the ionically stabilized micelles. The amount of the released doxorubicin exceeded 53% in the first 24 h and the slow and sustained release was retained to 65% in 90 h. On the other hand, the release from the non-stabilized micelles was limited to 5% in 24 h. Considering that more than 60% paclitaxel was released from the same system under the same conditions, the slow and almost restrained release of doxorubicin from the non-stabilized micelle could be attributed to the electrostatic nature of doxorubicin at the physiological condition. Doxorubicin possesses a primary amino group and become positively charged at pH 7.4. Positively charged doxorubicin was initially interacting with negatively charged aspartic acid residues of the micelles under the physiological condition and trapped in the micelles through ionic interactions in the absence of the metal cations. From the experimental section, the amount of loaded doxorubicin was 7.7  $\mu\text{mol}$  and available carboxylic acid groups in the copolymer was calculated as 12.5  $\mu\text{mol}$ , which supported that the copolymer possessed enough anionic

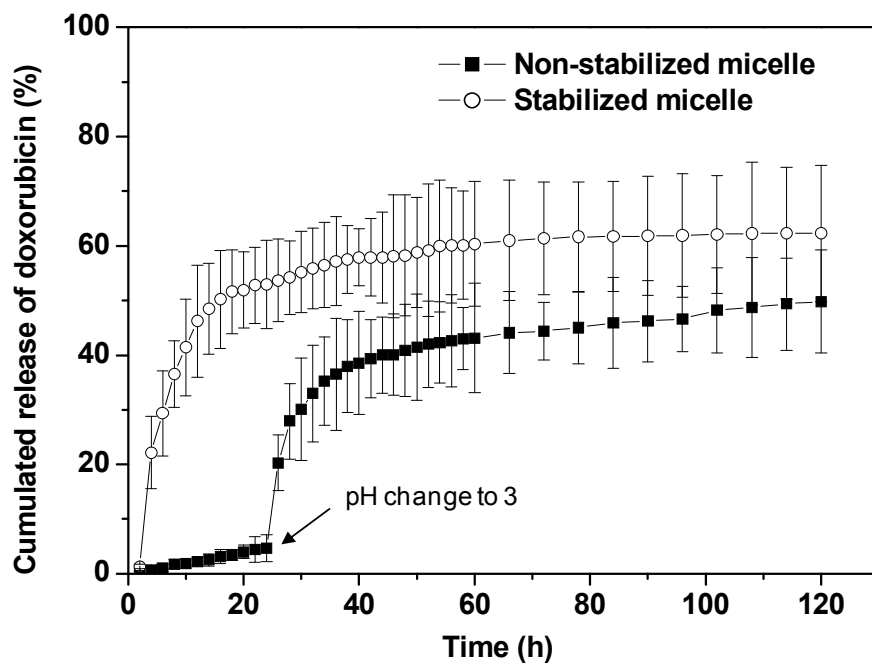


**Figure 6-2.** In vitro doxorubicin release profiles from non-stabilized micelle (■) and stabilized micelle (○) at 37 °C.

sites to hold the employed cationic doxorubicin at pH 7.4. Cationic calcium, which was added afterwards in excess, competed with doxorubicin for the ionic interaction with the fixed number of anionic binding sites and eventually took over the sites due to the higher concentration. Freed doxorubicin was then encapsulated in the hydrophobic core of the ionically stabilized micelles and followed the typical release patterns as described in the previous study with paclitaxel.

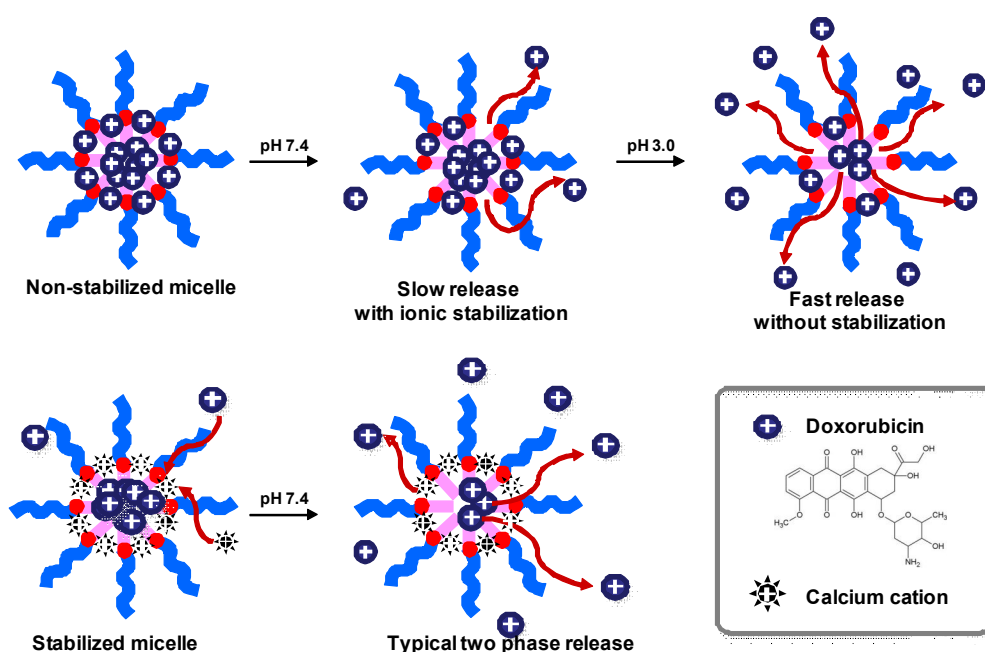


**Figure 6-3.** Plausible mechanism of pH dependent drug release patterns from (a) non-stabilized micelle and (b) stabilized micelle.

The carboxylic acid groups of the aspartic acid has the pKa value of 3.65<sup>[18]</sup> and decreasing pH of the solution below the pKa weakens the ionic interactions between the copolymer and doxorubicin via protonating the negatively charged carboxylic acids and neutralizing the compounds. As shown in Figure 6-2, changing the pH of the release media to 3.0 resulted in an abrupt release of doxorubicin from the nonstabilized micelles from 5 to 41% in an additional 12 h due to the fact that protonated neutral aspartic acid residues could not prevent doxorubicin from releasing out of the micelles. Figure 6-3 illustrates a proposed mechanism for the pH dependent release patterns. Encapsulating positively charged doxorubicin into the micelles self-assembled from an amphiphilic copolymer containing carboxylic acid segments sustained the release of the drugs through ionic interactions at the physiological condition. The micelle system selectively released the cationic drugs at the lower pH and this approach highlights a new way of preparing pH-sensitive delivery system.

#### **6.4. Conclusion**

Release profiles of positively charged doxorubicin were investigated from the polymeric micelle possessing anionic oligomers at the interface

between hydrophilic and hydrophobic blocks. The release patterns from ionically stabilized micelles using divalent calcium were compared to that from non-stabilized micelles experiencing pH change down to 3.0 after 24 h. Doxorubicin was ionically trapped in the micelles and displayed negligible release of less than 5% in the absence of calcium stabilization. Decreasing pH of the media down to 3.0 protonated the carboxylic acids and neutralized the copolymer, which resulted in decreasing ionic interactions as well as fast release of doxorubicin from the non-stabilized micelles. The doxorubicin-loaded stabilized micelles showed the two-phase-release profile, a stage with burst release, followed by slow and sustained release. Doxorubicin was ionically trapped in the non-stabilized micelle delivery system under the physiological condition and displayed the pH-dependent release behavior.

## **6.5. References**

- [1] P. H. Elworthy, A. T. Florence, and C. B. Macfarlane, *Solubilization by Surface Active Agents*, Chapman & Hall, London, 1968.
- [2] D. Attwood and A. T. Florence, *Surfactant Systems*, Chapman & Hall, London, 1983.
- [3] D. D. Lasic, *Nature* **1992**, 355, 279.

- [4] D. D. Lasic and F. J. Martin, *Stealth Liposomes*, CRC, Boca Raton, Florida, 1995.
- [5] V. P. Torchilin and V. S. Trubetskoy, *Adv. Drug Deliver. Rev.* **1995**, *16*, 141.
- [6] M. Jones and J. Leroux, *Eur. J. Biopharm.* **1999**, *48*, 101.
- [7] D. L. Garrec, S. Gori, L. Luo, D. Lessar, D. C. Smith, M.-A. Yessine, M. Ranger, and J.-C. Leroux, *J. Control. Release* **2004**, *99*, 83.
- [8] E. S. Lee, K. Na, and Y. H. Bae, *J. Control. Release* **2005**, *103*, 405.
- [9] S.-W. Lee, D.-H. Chang, M.-S. Shim, B.-O. Kim, S.-O. Kim, and M.-H. Seo, *Pharm. Res.* **2007**, *24*, 1508.
- [10] A. N. Koo, H. J. Lee, S. E. Kim, J. H. Chang, C. Park, C. Kim, J. H. Park, and S. C. Lee, *Chem. Commun.* **2008**, *48*, 6570.
- [11] R. L. Mompalber, M. Karon, S. E. Siegel, and F. Avila, *Cancer Res.* **1976**, *36*, 2891.
- [12] F. A. Fornari, J. K. Randolph, J. C. Yalowich, M. K. Ritke, and D. A. Gewirtz, *Mol. Pharmacol.* **1994**, *45*, 649.
- [13] M. S. Ewer and E. Yeh, *Cancer and the Heart*, BC Decker, Ontario, 2006.
- [14] M. Prabaharan, J. J. Grailer, S. Pilla, D. A. Steeber, and S. Gong,

- Biomaterials* **2009**, *30*, 6065.
- [15] Y. Shamay, D. Paulin, G. Ashkenasy, and A. David, *Biomaterials* **2009**, *30*, 6460.
- [16] H. Sun, B. Guo, R. Cheng, F. Meng, H. Liu, and Z. Zhong, *Biomaterials* **2009**, *30*, 6358.
- [17] E.-J. Cha, J. E. Kim, and C.-H. Ahn, *Eur. J. Pharm. Sci.* **2009**, *38*, 341.
- [18] A. L. Lehninger, D. L. Nelson, and M. M. Cox, *Lehninger Principles of Biochemistry*, W. H. Freeman, 2001.

## **Chapter 7.**

**Development of novel nanocarriers for pH sensitive drug release using calcium phosphate coated gold nanoparticles**

## 7.1. Introduction

A newly coined word “theragnosis”, meaning that a system serves both diagnosis and therapy simultaneously, has received significant attention in biomedical fields. Essential requirements for theragnosis are an efficient drug delivery system with target-specificity and controlled drug release at the target site as well as an imaging probe to selectively visualize the disease sites in anatomical and functional ways for an effective diagnosis. Representative imaging modalities developed so far consist of computed tomography (CT), magnetic resonance imaging (MRI), positron emission tomography (PET), optical imaging and ultrasound <sup>[1-17]</sup>.

Nanoparticles are known to be selectively accumulated in cancerous tumor sites by passive targeting, so called, enhanced permeation and retention (EPR) effect <sup>[18]</sup>. The advantages of EPR effect have stimulated the investigation on the nanoparticulate contrast agents with the controlled particle size in order to selectively visualize the cancerous tumors. A variety of nanoparticles were developed as a contrast agent in the imaging system: iron oxide nanoparticles, gadolinium-chelated compounds and nanoparticles containing manganese for MRI contrast agents <sup>[18-25]</sup>, gold nanoparticles (AuNPs) and iodine-labeled silica nanoparticles for CT imaging <sup>[17, 26]</sup>,

polymeric self-assembled structures conjugated with fluorescence-based dyes for optical imaging <sup>[13, 27, 28]</sup> and radioisotope-labeled nanoparticles for PET and single photon emission computed tomography (SPECT) <sup>[27, 29]</sup>. Recent interests on the hybrid material combining organic, inorganic and metallic materials keep increasing for the development of an efficient and accurate imaging system <sup>[12, 24, 25, 30-33]</sup>. Among the nanoparticles, AuNPs opened a wide range of applications in biomedical fields due to their unique characteristics, such as easy surface modification, controllable size and shapes, excellent biocompatibility, fluorescence quenching via surface plasmon resonance and higher X-ray absorption coefficient than typical iodine agents. Our group reported gold nanoparticular imaging probes for protease-activatable optical imaging, liver-specific CT imaging and NIRF and CT dual modality imaging <sup>[6, 7, 34]</sup>.

In order to make a theragnostic system, an efficient way to encapsulate therapeutic drugs into the imaging probes should be considered. Hydrophobic drugs were easily encapsulated into the organic nanostructures modified with optical or radioisotope labeling. Positively charged drugs were ionically interacted with oppositely charged iron oxide nanoparticles to report a theragnostic effect based on MRI imaging and cancer therapy <sup>[7]</sup>.

Thiol-terminated drugs were loaded onto the surface of gold nanoparticles via gold-thiol interactions for CT imaging and reducing-environment sensitive drug delivery system <sup>[35, 36]</sup>.

In this report, theragnostic hybrid nanoparticles were developed based on metallic AuNPs, organic PEG copolymers and inorganic calcium phosphate (CaP) layers. Mineralization of CaP on an organic micelle was previously reported to prepare a pH-sensitive drug delivery system <sup>[37]</sup>. A similar approach was employed to develop an AuNP based theragnostic system: a CT imaging modality, PEGylated AuNPs for the enhanced stability in the physiological condition and biodegradable CaP inorganic layer deposition for drug loading as well as selective release after cellular uptake. In vitro characterizations were performed for the drug release profiles and the cell viability with the nanoparticles.

## 7.2. Experimental

**Materials.** Methoxy PEG amine (95+ %, molecular weight: 5K) was commercially available from Sunbio (Korea). Calcium chloride anhydrous (96+ %), sodium phosphate monobasic (98 %), 2-(benzyloxy)carbonyl amino-3-(benzyloxy)carbonyl sulfanyl propanoic acid,

(Z-Cys(Z)-OH, 98+ %), N,N-dicyclohexyldiimide (DCC, 99 %), 4-dimethylaminopyridine (DMAP, 98 %), hydrogen tetrachloroaurate(III) (95 %) and palladium (Pd/C, 10 wt% on activated carbon) were purchased from Sigma-Aldrich (St.Louis, MO). L-Aspartic acid 4-benzyl ester (99 %) was obtained from Bachem AG (Switzerland). Tetrahydrofuran (THF, 95%), methylene chloride (MC, 95 %) and n-hexane (95 %) were purchased from Daejung (Korea) and dried over sodium under nitrogen atmosphere. All other chemicals were commercially available and used as received.

**Instruments.** <sup>1</sup>H NMR analysis was performed using Advance-300 of Bruker Corporation (MA, USA). Molecular weight and distribution of polymers were determined by gel permeation chromatography equipped with Shimadzu RID-10A refractometer detector and Shodex KF columns. Measurement of particle size was carried out using Otsuka ELS-Z instrument with He-Ne laser at a wavelength of 630 nm. UV-Vis absorbance spectra of doxorubicin were measured by Shimadzu UV-1650 PC at the wavelength of 480 nm. Average values of particle size and UV absorption were calculated with the data from three runs.

### **Synthesis of L-aspartic acid N-carboxy anhydride (NCA).**

Aspartic acid 4-benzyl ester was converted to the corresponding NCA as reported previously. Aspartic acid 4-benzyl ester (2.00 g, 8.79 mmol) was suspended in 20 mL anhydrous THF and the suspension was introduced to a 2-neck round bottom flask equipped with a dropping funnel under nitrogen atmosphere. Temperature of the suspension was gradually increased to 55 °C and triphosgene, dissolved in 10 mL anhydrous THF, was added dropwise into the reaction mixture. After the suspended mixture became clear solution, the reaction continued for additional 1 h and the reaction solution was poured into 10-fold excess amount of n-hexane to precipitate NCA. The product was obtained by filtration and dried in vacuum for 12 h (1.90 g, 86.5 %).

### **Synthesis of mPEG-Asp-Cys block copolymer.** mPEG-Asp(OBzl)

block copolymer was prepared by ring-opening polymerization of L-aspartic acid NCA as described in chapter 5 <sup>[38]</sup>. Aspartic acid NCA protected by benzyl ester group (1.00 g, 4.00 mmol) was dissolved in 10 mL anhydrous DMF and introduced to a 50 mL round bottom flask. Methoxy PEG amine (1.00 g, 0.2 mmol), dissolved in 10 mL anhydrous DMF, was added to the

NCA solution as a macroinitiator. The polymerization continued for 72 h at room temperature under nitrogen atmosphere. The reaction solution was poured into 200 mL diethyl ether to precipitate the product. mPEG-Asp(OBzl) was obtained by filtration and dried in vacuum for 12 h (1.76 g, 88.0 %).

Z-Cys(Z)-OH (0.19 g, 0.48 mmol), DCC (0.10 g, 0.48 mmol) and DMAP(0.06 g, 0.48 mmol) were dissolved in 10 mL anhydrous methylene chloride and introduced to a 2-neck round bottom flask. After 30 min stirring at room temperature under nitrogen atmosphere, mPEG-Asp(OBzl) (1.50 g, 0.16 mmol) was added into the reaction solution and stirred for an additional 24 h. The reaction mixture was filtrated to remove DCU and condensed prior to precipitation. The product was obtained as white powder by precipitation into 10-fold excess amount of diethyl ether (1.33 g, 81.1 %).

Deprotection of protecting groups in mPEG-Asp(OBzl)-Cys(Z) (1.00 g, 0.11 mmol) was carried out with Pd/C (20 wt% of mPEG-Asp(OBzl)-Cys(Z)) in 20 mL anhydrous THF for 24 h under hydrogen pressure of 5 atm. After the complete deprotection, 20 mL THF solution containing 10 % 1 N HCl (v/v) was added into the reaction mixture to dissolve the deprotected polymers. Pd/C catalyst was filtered off using Celite and the

filtrate was poured into the diethyl ether to precipitate mPEG-Asp-Cys. The product was obtained after drying under reduced pressure at 25 °C overnight (0.34 g, 41.2 %). The synthetic scheme for mPEG-Asp-Cys was shown in Scheme 7-1.

**Preparation of PEGylated AuNP@CaP encapsulating doxorubicin.** Gold nanoparticles (AuNPs) were prepared by simple conventional method as previously reported <sup>[39]</sup>. Hydrogen tetrachloroaurate(III) (5.00 mmol) was dissolved in 500 mL deionized water and the solution was gradually heated to 95 °C. Then, 10 mL sodium citrate aqueous solution (1 wt%) was added quickly into the reaction solution and stirred vigorously. After 2 h, the color of the solution was changed to red with the formation of AuNPs.

mPEG-Asp-Cys was introduced onto the surface of AuNP to endow the nanoparticles with enhanced stability in the physiological condition and the sites for calcium immobilization. 10 mg mPEG-Asp-Cys was added into 10 mL AuNP aqueous solution (1 nM AuNP particle concentration). After stirring for 6 h, doxorubicin was added to the reaction solution, followed by an additional 2 h stirring to localize doxorubicin to the anionic aspartic acids

by ionic interaction. Then, calcium chloride aqueous solution was added and stirred for an additional 1 h to immobilize calcium ion at anionic aspartic acid layer. The intermediates were washed 3 times with deionized water to remove unbound polymers and free calcium ions. Sodium phosphate monobasic aqueous solution was added into the reaction solution and stirred for 12 h to induce calcium phosphate mineralization. The final product was washed 3 times with deionized water through centrifugation at 10000 rpm. The amount of encapsulated doxorubicin was evaluated by UV-Vis spectroscopy.

**Determination of doxorubicin release profiles.** In vitro release profiles of doxorubicin from the PEGylated Dox-AuNP@CaP were evaluated in two different aqueous solutions with the variation of pH and the concentrations of calcium and phosphate ions; an intracellular endosomal fluid (CaCl<sub>2</sub> 100 nM, Na<sub>2</sub>HPO<sub>4</sub> 40 mM, pH 4.5, NaCl 140 mM) and an extracellular fluid (CaCl<sub>2</sub> 2 mM, Na<sub>2</sub>HPO<sub>4</sub> 1 mM, Tris 25 mM, pH 7.4, NaCl 140 mM). PEGylated Dox-AuNP@CaP was dispersed in predetermined aqueous buffer solution and transferred to a pre-swollen cellulose dialysis membrane with the molecular weight cut off of 1 K. The

release study was carried out by soaking the dialysis bag in 20 mL release media and 1 mL aliquot was taken from the media prior to media change at a predetermined time interval. The amount of released doxorubicin was measured by UV-Vis spectroscopy.

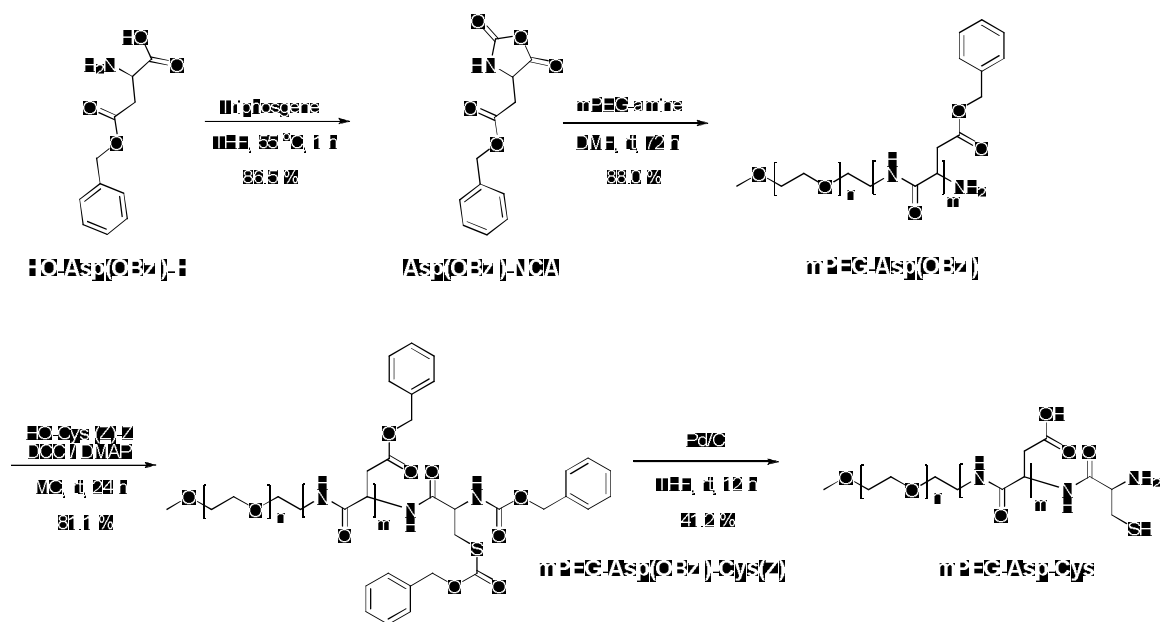
**Cell viability.** In vitro cytotoxicity of PEGylated AuNP@CaP and PEGylated Dox-AuNP@CaP was evaluated by MTT colorimetric assay. HeLa cells were grown in 96-well plates at a density of  $5 \times 10^3$  cells per well with 0.2 mL DMEM medium containing 10 % FBS. After 24 h incubation, cells were washed with pre-warmed DMEM medium before the treatment of PEGylated AuNP@CaP and PEGylated Dox-AuNP@CaP. Cells were incubated for 24 h at 37 °C with the nanoparticles and the cell viability was determined by the conventional MTT assay.

### 7.3. Results and discussion

mPEG-Asp(OBzl)-Cys(Z)-Z was synthesized by ring opening polymerization of the corresponding L-aspartic acid 4-benzyl ester NCA, followed by DCC/DMAP coupling between N-terminus of the mPEG-Asp(OBzl) and C-terminus of Z-Cys(Z)-OH. Deprotection by

hydrogenation of benzyl ester and CBZ groups produced the final water soluble mPEG-Asp-Cys. The synthetic scheme is illustrated in Scheme 7-1. mPEG-NH<sub>2</sub> with the molecular weight of 5 K and M<sub>w</sub>/M<sub>n</sub> of 1.06 initiated the polymerization for the formation of mPEG-Asp(OBzl) block copolymers. GPC traces in Figure 7-1 shows clear shift of the peak molecular weight to a higher molecular weight region after polymerization, supporting the successful formation of block copolymers. mPEG-Asp(OBzl)-Cys(Z)-Z was characterized by <sup>1</sup>H NMR to have 18 aspartic acid units and 0.95 cysteine on average, as shown in Figure 7-2a. Deprotection of the protecting groups was performed using Pd/C under 5 atm H<sub>2</sub> and the disappearance of the phenyl peaks in Figure 7-2b confirmed the complete deprotection. The molecular weight and distribution of the final product, mPEG-Asp-Cys, was 13.1 K and 1.15, respectively, by GPC analysis with the PEG standard.

Theragnostic nanoparticles were designed by decorating mPEG-Asp-Cys on the surface of AuNP with the size of 25 nm, followed by doxorubicin encapsulation and calcium phosphate (CaP) layer deposition. The nanoparticles consist of three defined domains: the hydrophilic PEG corona, drug-containing and structure-stabilizing CaP middle layer, and AuNP core



**Scheme 7-1.** Synthetic scheme of mPEG-Asp-Cys.

playing the role of CT contrast agents. The preparation scheme of PEGylated AuNPs with doxorubicin containing CaP layers (PEGylated Dox-AuNP@CaP) is shown in Figure 7-3. TEM images in Figure 7-4a supported that CaP layer was successfully introduced on the surface of AuNPs with the thickness around 27 nm. Aggregation between AuNPs and byproduct formation of free CaP particles were not observed. The mean hydrodynamic diameter of PEGylated Dox-AuNP@CaP was  $79.8 \pm 18.7$  nm

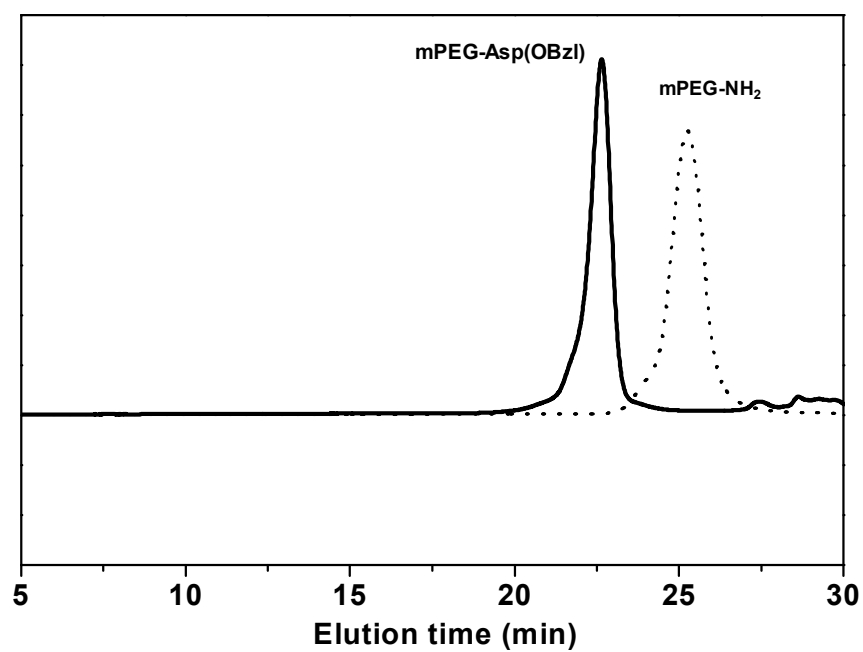


**Figure 7-1.** GPC traces of mPEG-Asp(OBzl) and mPEG-NH<sub>2</sub> using DMF as an eluent.

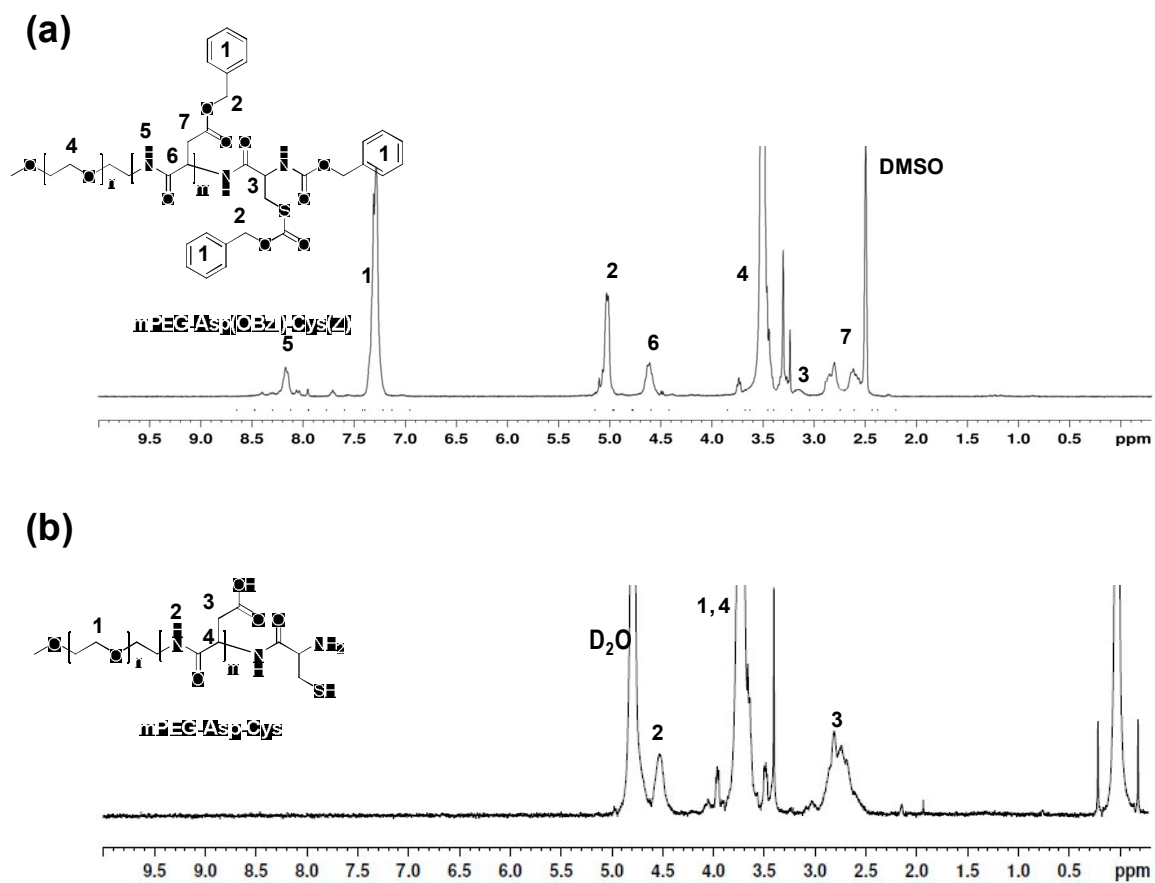


**Figure 7-2.** NMR spectra of (a) mPEG-Asp(OBzl)-Cys(Z) and (b) mPEG-Asp-Cys.

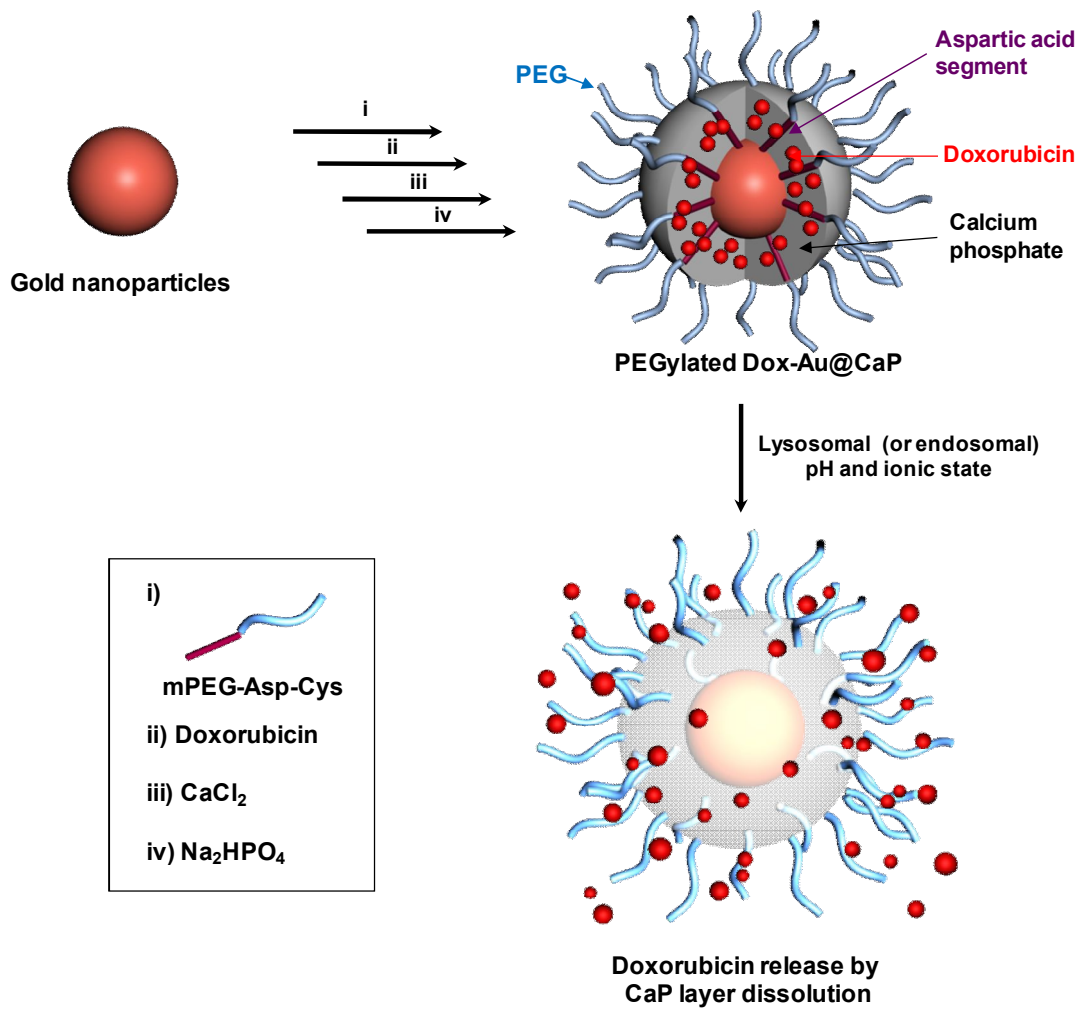


**Figure 7-3.** Synthetic method of PEGylated Dox-Au@CaP.

by light scattering measurement (Figure 7-4b). PEG corona endowed the AuNPs with biocompatibility and enhanced stability in the blood stream for long-circulation and 18 aspartic acid residues in the block copolymer hosted calcium cations for mineral deposition and doxorubicin by electrostatic interaction. Controlled amount of calcium cations, a half molar concentration of calcium to aspartic acid, induced the successful mineralization and the CaP deposition at the middle layer without any noticeable formation of free CaP particles. High ionic concentration above the critical saturation level, achieved by the localization of calcium and phosphate ions at the block copolymers on the AuNPs, was believed to trigger the CaP deposition and the growth.

mPEG-Asp-Cys was successfully attached on the surface of AuNP in aqueous condition, considering the fact that thiol group is reported to have the strongest interaction with AuNP surfaces among the functional groups. However, even thiol-linked PEGs on AuNP are unstable at elevated temperature, in the presence of biological reducing agents, and in the physiological condition with high salt concentration. The stability of PEGylated Dox-AuNP@CaP was evaluated in the presence of glutathione, which is a well known reducing agent for disulfide and gold-thiol bond,

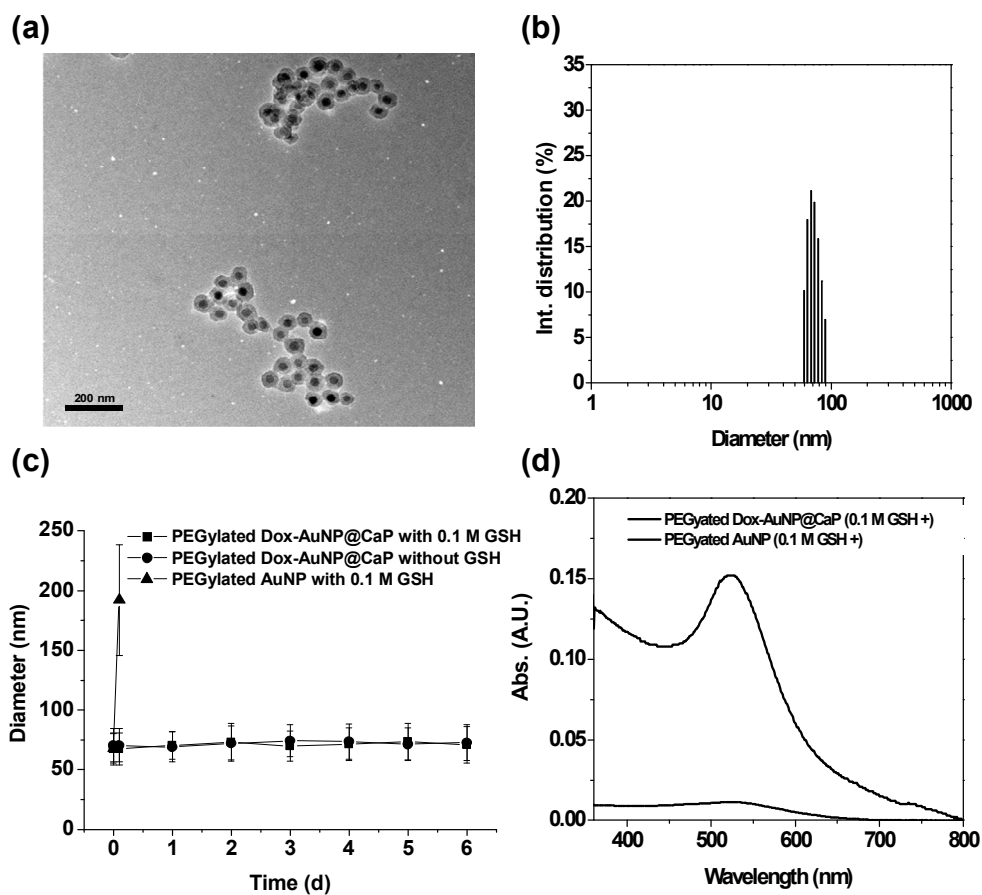


**Figure 7-4.** (a) TEM image, (b) size distribution, (c) stability of PEGylated Dox-AuNP@CaP with/without GSH and (d) UV spectra of PEGylated Dox-AuNP@CaP and PEGylated AuNP with GSH.

with time using UV/Vis spectroscopy and light scattering measurement. AuNPs exhibited a characteristic surface plasmon resonance (SPR) peak around 520 nm as analyzed by UV/Vis spectroscopy. When PEGylated AuNPs were treated with the glutathione, the SPR peak was dramatically decreased in several seconds because the reducing agent removed the mPEG-Asp-Cys from the surface of AuNPs which led to the particle aggregation. On the contrary, the UV spectra of PEGylated Dox-AuNP@CaP with glutathione still displayed the characteristic peak since the CaP middle layers cross-linked and held the polymers regardless of the stability between the AuNP and thiol terminus of the mPEG-Asp-Cys polymers. In addition, PEGylated AuNP@CaP maintained the original particle size for several weeks in PBS with and without 0.1 M glutathione at 37 °C, whereas PEGylated AuNPs without CaP layers were immediately aggregated to give an abrupt increase in size within a few minutes after exposure to glutathione. The results are shown in Figure 7-4c and 7-4d, indicating that mineralized CaP layer endowed the AuNPs with the stability even in the reducing environment in the body.

There are several papers reporting that charged molecules are co-mineralized during the formation of CaP layers. Doxorubicin, a positively

charged anti-cancer drug, was successfully incorporated into the PEGylated Dox-AuNP@CaP, as described in the experimental section. Doxorubicin was co-localized with calcium ions on the aspartic acid residues by electrostatic interaction. Quantitative calcium chloride, 0.5 equivalents against carboxyl acid groups of mPEG-Asp-Cys, was added and remaining carboxyl acid groups were interacted with doxorubicin. Loading amount and loading efficiency of doxorubicin were 1.3 % and 27.9 %, respectively.

The loading amount was much lower than that from organic self-assembled structures such as micelles or self-aggregates, however, taking into account the high atomic mass of gold, the loading amount of 1.3 % was acceptable. Optimized drug delivery system is supposed to keep the drug within the vehicles during the circulation and release the drug at the disease site with burst or sustained pattern. The extracellular exterior (extracellular fluid, pH 7.4) and intracellular lysosomal interior (intracellular fluid, pH 4.5) conditions were employed to mimic the pH condition of blood-circulation and cellular uptake at disease site, respectively. Figure 7-5 shows that doxorubicin release profiles from PEGylated Dox-AuNP@CaP and PEGylated Dox-AuNP in two different conditions. The amount of released doxorubicin from PEGylated Dox-AuNP, without CaP layer, exceeds 60 %

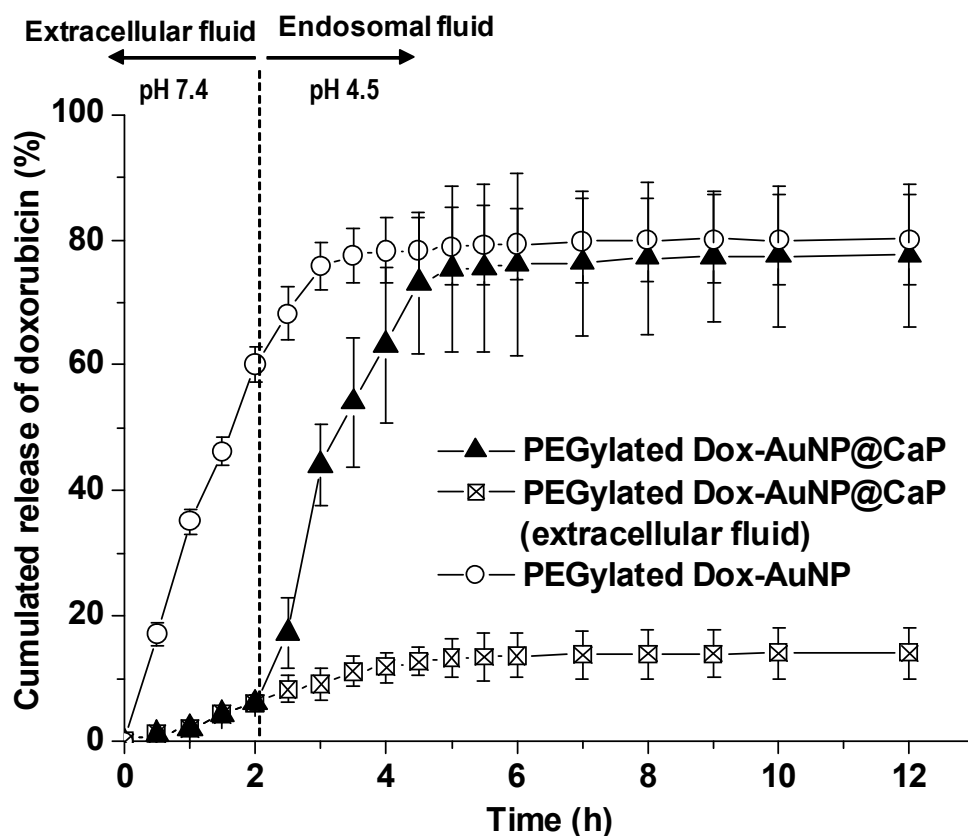


Figure 7-5. Drug release profiles of PEGylated Dox-Au@CaP.

in 2 h and the media change from extracellular to intracellular fluid did not produce any noticeable change of the release profile. In contrast, PEGylated Dox-AuNP@CaP effectively limited the doxorubicin release in extracellular condition down to 13 % after 12 h, meaning that the release of encapsulated

drugs was suppressed during the blood circulation due to the CaP barrier layer. Changing the media to the intracellular lysosomal condition, where pH is low enough to dissolve the CaP layer, resulted in a triggered release of doxorubicin from 7 to 78 % in an additional 4 h. These results imply that the CaP layer played the role of a diffusion barrier for the drug release and PEGylated Dox-AuNP@CaP delivery system selectively released the drugs at the target without wasting them during the circulation to produce a stable nanocarrier with controllable drug release and a drug carrier with great potentials as intravenous delivery system.

Cell viability of PEGylated Dox-AuNP@CaP and PEGylated AuNP@CaP were estimated with HeLa cells by MTT assay. Nanoparticles treated HeLa cells were incubated with time variation to evaluate optimized incubation time. Cell viability of PEGylated Dox-AuNP@CaP was gradually decreased and became down to 19 % after 24 h incubation. PEGylated AuNP@CaP particle itself showed slight cytotoxicity with the same condition; however, it was negligible and the following experiment was performed with the incubation time of 24 h. As shown in Figure 7-6, cell viability was dramatically decreased with particle concentration for PEGylated Dox-AuNP@CaP after 24 h. The significant difference in cell

viability between PEGylated Dox-AuNP@CaP and PEGylated AuNP@CaP was believed to stem from the doxorubicin release by the dissolution of CaP layer at the lower pH after the cells had uptaken the nanoparticles into the endosome.

AuNP decorated with matrix metalloproteinase (MMP) activatable optical probe was developed by our group. The probe was quenched in a normal state and the near infrared-fluorescence (NIRF) was recovered when the AuNPs were located near the regions overexpressing MMPs. As shown in Figure 7-7a, the AuNP-based NIRF probes allowed the visualization of tumors via direct injection into the tumor sites. Systemic delivery system was not achieved due to the fact that the hydrophilic dye and peptide on the surface of AuNPs could not prevent the nanoparticles from being aggregated in the physiological condition with the high salt concentration. In order to develop a systemic delivery system of imaging probes, AuNPs were coated with biocompatible and hydrophilic glycol chitosan (GC) and further furnished with MMP activatable NIRF probes (MMP-GC-AuNP). When injected intravenously, MMP-GC-AuNPs were efficiently accumulated in the tumor tissue and their NIRF was recovered sensitively by MMP enzymes. MMP-GC-AuNP imaging probe visualized the tumor tissue using

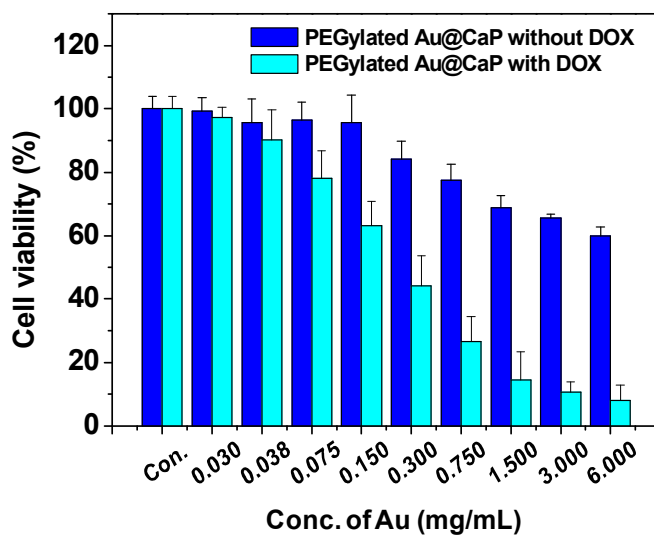
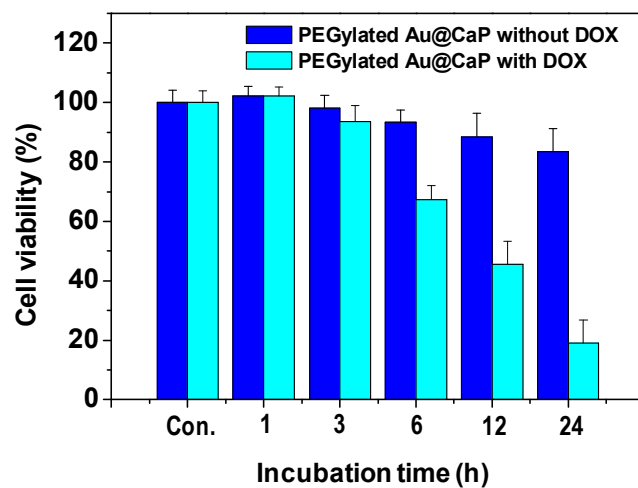


**Figure 7-6.** Cytotoxicity of PEGylated Dox-Au@CaP and PEGylated Au@CaP as a function of (a) incubation time and (b) concentration.

CT and optical imaging at the same time. It provided anatomical information on the tumor sites and MMP-dependent biological functional information, simultaneously. A target-molecule-specific CT/optical dual imaging probe for cancer was developed, but the MMP-GC-AuNP probe could not make therapeutic effects. Based on the previous results PEGylated Dox-AuNP@CaP was designed as a theragnostic nanoparticle for visualization of tumor site using the characteristics of AuNP producing CT images and therapeutic effect releasing anti-cancer drugs at the disease site. Deposited CaP layer played an important role to enhance the stability of AuNP in the reducing environment and at the same time served as a diffusion barrier for drugs during the circulation to selectively release the drugs at the target sites.

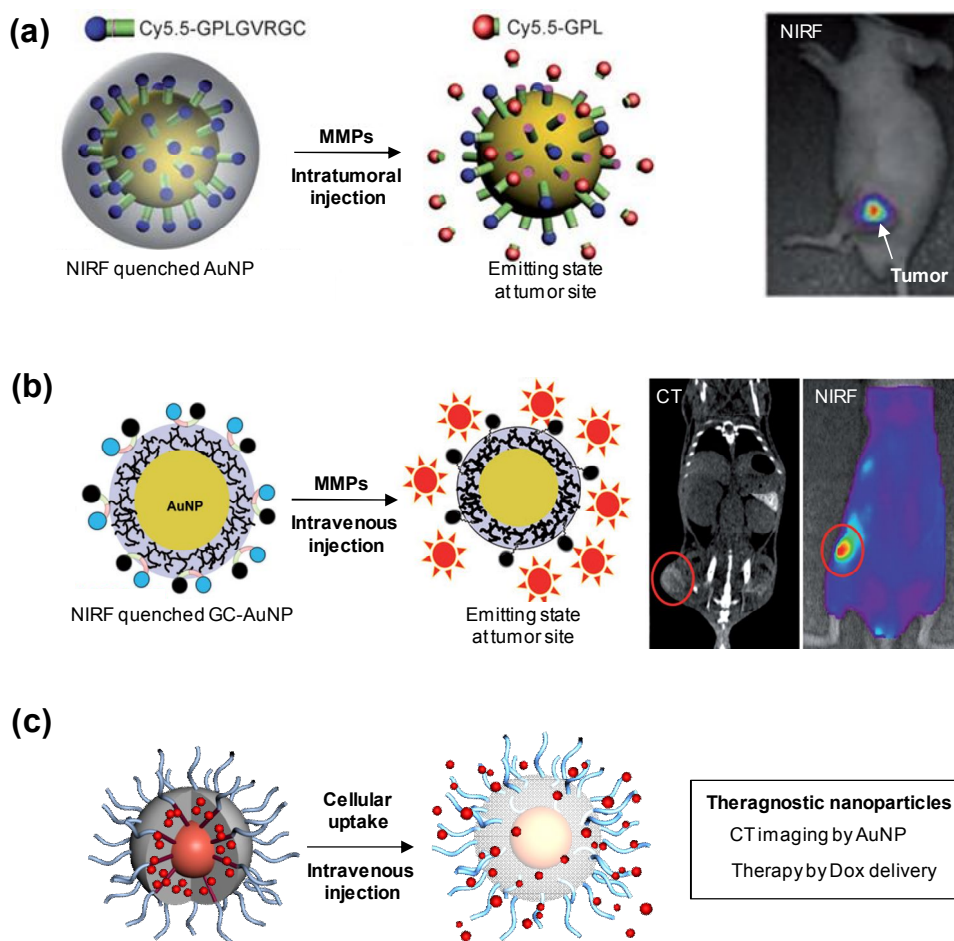


**Figure 7-7.** Cytotoxicity of PEGylated Dox-Au@CaP and PEGylated Au@CaP as a function of (a) incubation time and (b) concentration.

#### 7.4. Conclusion

PEGylated Dox-AuNP@CaP was developed and its potential as a theragnostic agent for CT imaging and cancer therapy was evaluated. AuNP

were stabilized with mPEG-Asp-Cys copolymers and CaP layer encapsulating doxorubicin was deposited by mineralization. PEGylated Dox-AuNP@CaP was stable for an extended time in the physiological conditions and displayed low cytotoxicity enough to claim that the prepared nanoparticles had a potential to be applied as a platform material for in vivo imaging agents. Prepared nanoparticles showed an increased drug release rate in the intracellular endosomal/lysosomal fluid in comparison with that in the extracellular fluid due to the dissolution of CaP layers by decreased pH at endosomal fluid. These results supports that PEGylated Dox-AuNP@CaP can be used as a stimuli-sensitive, such as pH and ion concentration, drug delivery system and work as a new theragnostic nanoparticles.

## 7.5. References

- [1] E. Dulkeith, A. C. Morteani, T. Niedereichholz, T. A. Klar, J. Feldmann, S. A. Levi, F. C. J. M. van Veggel, D. N. Reinhoudt, M. Moller, and D. I. Gittins, *Phys. Rev. Lett.* **2002**, *89*, 2030.
- [2] G. Antoch, F. M. Vogt, L. S. Freudenberg, F. Nazaradeh, S. C. Goehde, J. Barkhausen, G. Dahmen, A. Bockisch, J. F. Debatin, and

- S. G. Ruehm, *J. Am. Med. Assoc.* **2003**, *290*, 3199.
- [3] M. Doubrovin, I. Serganova, P. Mayer-Kuckuk, V. Ponomarev, and R. G. Blasberg, *Bioconjugate Chem.* **2004**, *15*, 1376.
- [4] E. A. Schellenberger, D. Sosnovik, R. Weissleder, L. Josephson, *Bioconjugate Chem.* **2004**, *15*, 1062.
- [5] H. Y. Lee, Z. Li, K. Chen, A. R. Hsu, C. Xu, J. Xie, S. Sun, and X. Chen, *J. Nucl. Med.* **2009**, *49*, 1371.
- [6] S. Lee, E.-J. Cha, K. Park, S.-Y. Lee, J.-K. Hong, I.-C. Sun, S. Y. Kim, K. Choi, I. C. Kwon, K. Kim, and C.-H. Ahn, *Angew. Chem. Int. Ed.* **2008**, *47*, 2804.
- [7] M. K. Yu, Y. Y. Jeong, J. H. Park, S. J. Park, J. W. Kim, J. J. Min, K. W. Kim, and S. Jon, *Angew. Chem. Int. Ed.* **2008**, *47*, 5362.
- [8] M. Ogawa, C. A. Regino, J. Seidel, M. V. Green, W. Xi, M. Williams, N. Kosaka, P. L. Choyke, and H. Kobayashi, *Bioconjugate Chem.* **2009**, *20*, 2177.
- [9] O. Veiseh, C. Sun, C. Fang, N. Bhattarai, J. Gunn, F. Kievit, K. Du, B. Pullar, D. Lee, R. G. Ellenbogen, J. Olson, and M. Zhang, *Cancer Res.* **2009**, *69*, 6200.
- [10] Z. Cheng, D. L. J. Thorek, and A. Tsourkas, *Angew. Chem. Int. Ed.*

- 2010**, *49*, 346.
- [11] Y. Jin, C. Jia, S.-W. Huang, M. O'Donnell, and X. Gao, *Nat. Commun.* **2008**, *1*, 1.
- [12] S.R. Mudd, V. S. Trubetskoy, A. V. Blokhin, J. P. Weichert, and J. A. Wolff, *Bioconjugate Chem.* **2010**, *21*, 1183.
- [13] T. Nam, S. Park, S. Y. Lee, K. Park, K. Choi, I. C. Song, M. H. Han, J. J. Leary, S. A. Yuk, I. C. Kwon, K. Kim, and S.Y. Jeong, *Bioconjugate Chem.* **2010**, *21*, 578.
- [14] E.S. Olson, T. Jiang, T. A. Aguilera, Q. T. Nguyen, L. G. Ellies, M. Scadeng, and R.Y. Tsien, *Proc. Nat. Acad. Sci.* **2010**, *107*, 4311.
- [15] J. Xie, K. Chen, J. Huang, S. Lee, J. Wang, J.Gao, X. Li, and X. Chen., *Biomaterials* **2010**, *31*, 3016.
- [16] M.P. Melancon, M. Zhou, and C. Li, *Acc. Chem. Res.* **2011**, *44*, 947.
- [17] I.-C. Sun, D.-K. Eun, H. Koo, C.-Y. Ko, H.-S. Kim, D. K. Yi, K. Choi, I. C. Kwon, K. Kim, and C.-H Ahn, *Angew. Chem. Int. Ed.* **2011**, *50*, 9348.
- [18] I. Brigger, C. Dubernet, and P. Couvreur, *Adv. Drug Deliver. Rev.* **2002**, *54*, 631.
- [19] J. Shin, R. M. Anisur, M. K. Ko, G. H. Im, J. H. Lee, and I. S. Lee,

- Angew. Chem. Int. Ed.* **2009**, *48*, 321.
- [20] J. Kim, H. S. Kim, N. Lee, T. Kim, H. Kim, T. Yu, I. C. Song, W. K. Moon, and T. Hyeon, *Angew. Chem. Int. Ed.* **2008**, *47*, 8438.
- [21] M. F. Kircher, U. Mahmood, R. S. King, R. Weissleder, and L. Josephson, *Cancer Res.* **2003**, *63*, 8122.
- [22] S. Cheong, P. Ferguson, K. W. Feindel, I. F. Hermans, P. T. Callaghan, C. Meyer, A. Slocombe, C.-H. Su, F.-Y. Cheng, C.-S. Yeh, B. Ingham, M. F. Toney, and R. D. Tilley, *Angew. Chem. Int. Ed.* **2011**, *50*, 4206.
- [23] Y.-X. J. Wang, S. M. Hussain, and G. P. Krestin, *Eur. Radiol.* **2001**, *11*, 2319.
- [24] J. H. Choi, S. Lee, H. J. Kang, J. Y. Lee, J. Kim, H. O. Yoo, T. R. Stratton, B. M. Applegate, J. P. Youngblood, H. J. Kim, and K. N. Ryu, *Macromol. Res.* **2010**, *18*, 504.
- [25] H. Lee, M. K. Yu, S. Park, S. Moon, J. J. Min, Y. Y. Jeong, and S. Jon, *J. Am. Chem. Soc.* **2008**, *129*, 12739.
- [26] Y.-H. Kim, J. Jeon, S. H. Hong, W.-K. Rhim, Y.-S. Lee, H. Youn, J.-K. Chung, M. C. Lee, D. S. Lee, K. W. Kang, and J.-M. Nam, *Small* **2011**, *7*, 2052.

- [27] R. Zhang, C. Xiong, M. Huang, M. Zhou, Q. Huang, X. Wen, D. Liang, and C. Li., *Biomaterials* **2011**, *32*, 5872.
- [28] S. M. Yoon, S.-J. Myung, I.-W. Kim, E.-J. Do, B. D. Ye, J. H. Ryu, K. Park, K. Kim, I. C. Kwon, and M. J. Kim, *Digest. Dis. Sci.* **2011**, *56*, 3005.
- [29] R. R. Patil, J. Yu, S. R. Banerjee, Y. Ren, D. Leong, X. Jiang, M. Pomper, B. Tsui, D. L. Kraitchman, and H.-Q. Mao, *Molecular Therapy* **2011**, *19*, 1626.
- [30] T. R. Sathe, A. Agrawal, and S. Nie., *Anal. Chem.* **2006**, *78*, 5627.
- [31] L.E. Jennings and N.J. Long, *Chem. Commun.* **2009**, *28*, 3511.
- [32] K.M.K. Selim, J.-H. Lee, S.-J. Kim, Z. Xing, I.-K. Kang, Y. Chang, and H. Guo, *Macromol. Res.* **2006**, *14*, 646.
- [33] R. Xing, F. Zhang, J. Xie, M. Aronova, G. Zhang, N. Guo, X. Huang, X. Sun, G. Liu, L. H. Bryant, A. Bhirde, A. Liang, Y. Hou, R. D. Leapman, S Sun and X. Chen, *Nanoscale* **2011**, *3*, 4943.
- [34] I.-C. Sun, D.-K. Eun, J. H. Na, S. Lee, I.-J. Kim, I.-C. Youn, C.-Y. Ko, H.-S. Kim, D. Lim, K. Choi, P. B. Messersmith, T. G. Park, S. Y. Kim, I. C. Kwon, K. Kim, and C.-H. Ahn, *Chem.Eur. J.* **2010**, *15*, 13341.

- [35] G. Han, P. Ghosh, M. De, V. M. Rotello, *Nanobiotechnology* **2007**, 3, 40.
- [36] N.L. Rosi, D. A. Giljohann, C. S. Thaxton, A. K. R. Lytton-Jean, M. S. Han, and C. A. Mirkin, *Science* **2006**, 312, 1027.
- [37] H.J. Lee, S. E. Kim, I. K. Kwon, C. Park, C. Kim, J. Yang, and S. C. Lee., *Chem. Commun.* **2010**, 46, 377.
- [38] T. J. Deming, *Adv. Polym. Sci.* **2006**, 202, 1.
- [39] G. Frens, *Nat. Phy. Sci.* **1973**, 241, 20.

## **Chapter 8.**

**Development of calcium phosphate coated  
superparamagnetic iron oxide nanoparticles for  
combined MRI and drug delivery**

## 8.1. Introduction

Cancer therapy using metallic or inorganic nanoparticles, such as gold nanoparticles and iron oxide nanoparticles, draw attention in terms of theragnostic platform because of their novel and intrinsic physical properties [1-2]. In particular, the potential of magnetic nanoparticles in drug delivery has been focused recently. The magnetic nanoparticles based on superparamagnetic iron oxide nanoparticles have several advantages in terms of i) visualization by magnetic resonance imaging; ii) hyperthermia for cancer therapy; and iii) degradability in physiological condition [3-6]. Considering what the main issue with the metallic or inorganic nanoparticles is the toxicity resulted from their long-term residence in vivo, superparamagnetic nanoparticles can be an excellent candidate for in vivo theragnostic application [3-13].

Recently, a number of nanocarriers based on superparamagnetic iron oxide have been investigated worldwide [6-21]. Jon et. al. reported drug loaded iron oxide nanoparticles using electrostatic interaction between positively charged doxorubicin and thermally cross-linked superparamagnetic iron oxide nanoparticles (TCL-SPIONs) which have negatively charged surface [11]. Haam et. al. developed anti-HER2, antibody-

conjugated, multifunctional magnetopolymeric nanohybrids and demonstrated their potential as an in vivo application [7, 8]. In addition, anticancer drugs such as epirubicin- and mitoxantrone bound magnetic fluids have been developed and used for locoregional cancer treatment in phase I clinical trials by A. S. Lubbe's group [12].

However, these systems have no target specific drug release properties and turned out to be effective only under the appropriate strength of the external magnetic field. Very recently, our group reported calcium phosphate based theragnostic nanoparticles which have environmental sensitive drug release property for overcoming these drawbacks [22]. The nanoparticles showed excellent stability in blood circulation condition, low toxicity and selective drug release in endosomal environment. Herein, we described a fabrication method and in vitro characterization of iron oxide based theragnostic nanocarrier. A similar approach was employed to develop superparamagnetic iron oxide nanoparticles based theragnostic platform which have magnetic imaging modality and biodegradable calcium phosphate layer for selective drug release after cellular uptake. Further, the potential as an in vivo theragnostic platform was evaluated in current study.

## 8.2. Experimental

**Materials.** Methoxy PEG amine (95+ %, molecular weight: 5K) was commercially available from Sunbio (Korea). Calcium chloride anhydrous (96+ %), sodium phosphate monobasic (98 %), 2-(benzyloxy)carbonyl amino-3-(benzyloxy)carbonyl sulfanyl propanoic acid, (Z-Cys(Z)-OH, 98+ %), N,N-dicyclohexyldiimide (DCC, 99 %), 4-dimethylaminopyridine (DMAP, 98 %), hydrogen tetrachloroaurate(III) (95 %) and palladium (Pd/C, 10 wt% on activated carbon) were purchased from Sigma-Aldrich (St.Louis, MO). L-Aspartic acid 4-benzyl ester (99 %) was obtained from Bachem AG (Switzerland). Tetrahydrofuran (THF, 95%), methylene chloride (MC, 95 %) and n-hexane (95 %) were purchased from Daejung (Korea) and dried over sodium under nitrogen atmosphere. All other chemicals were commercially available and used as received.

**Instruments.**  $^1\text{H}$  NMR analysis was performed using Advance-300 of Bruker Corporation (MA, USA). Molecular weight and distribution of polymers were determined by gel permeation chromatography equipped with Shimadzu RID-10A refractometer detector and Shodex KF columns. Measurement of particle size was carried out using Otsuka ELS-Z

instrument with He-Ne laser at a wavelength of 630 nm. UV-Vis absorbance spectra of doxorubicin were measured by Shimadzu UV-1650 PC at the wavelength of 480 nm. Average values of particle size and UV absorption were calculated with the data from three runs.

**Synthesis of L-aspartic acid N-carboxy anhydride (NCA) and polymerization of mPEG-PA<sub>sp50</sub>-DOPAC block copolymer.** Aspartic acid 4-benzyl ester was converted to the corresponding NCA as described at section 4.1.2. Briefly, aspartic acid 4-benzyl ester (2.00 g, 8.79 mmol) was suspended in 20 mL anhydrous THF and temperature of the suspension was gradually increased to 55 °C. Then triphosgene dissolved in 10 mL anhydrous THF solution was added dropwise into the reaction mixture. After the suspended mixture became clear, the reaction continued for additional 1 h and the NCA was precipitated with 10-fold excess amount of n-hexane. The product was obtained by filtration and dried in vacuum for 12 h.

mPEG-Asp(OBzl)<sub>50</sub> block copolymer was polymerized using same procedure previously described in section 4.1.2. Briefly, aspartic acid NCA protected by benzyl ester group (1.00 g, 4.00 mmol) was dissolved in 10 mL anhydrous DMF and methoxy PEG amine (0.40 g, 0.08 mmol) was added to

the NCA solution as a initiator. The reaction continued for 72 h at room temperature under nitrogen atmosphere. The solution was poured into 150 mL diethyl ether to precipitate the product. mPEG-Asp(OBzl)<sub>50</sub> was obtained by filtration and dried in vacuum for 12 h.

DOPAC was conjugated with mPEG-Asp(OBzl)<sub>50</sub> via simple DCC/DMAP coupling method. mPEG-Asp(OBzl)<sub>50</sub> (500.0 mg) and DOPAC (197.0 mg, 1 mmol) were dissolved in 50.0 mL methylene chloride and the solution was placed in 100 mL round bottom flask. Then, DCC (3.0 mmol) and DMAP (3.0 mmol) were added into the reaction solution. After additional 24 h stirring, the solution was filtered by PTFE filtration membrane to remove DCU and the solution was condensed. Condensed solution was poured into 300 mL diethyl ether to precipitate mPEG-PAsp<sub>50</sub>-DOPAC and the product was dried overnight in vacuum. The product was analyzed by NMR and UV spectrophotometer.

**Fabrication of the PEGylated Dox-FeO<sub>x</sub>@CaP.** mPEG-PAsp<sub>50</sub>-DOPAC (50 mg) was dissolved in 10 mL DMSO and the solution was added into 10 mL FeO<sub>x</sub> nanoparticle solution (0.1 Fe mg/mL, in chloroform). The reaction solution was vigorously stirred for 12 h and chloroform was

evaporated. After evaporation of chloroform, 0.1 N NaOH solution (10 mL) was added dropwise into the solution and stirred for 6 h. FeO<sub>x</sub> aggregates were collected using external magnet and washed 3 times with deionized water. The aggregates were re-dispersed in 10 mL deionized water for further experiments.

Doxorubicin was added to the prepared solution, followed by an additional 2 h stirring to immobilize doxorubicin to the anionic aspartic acids by electrostatic interaction. Then, calcium chloride aqueous solution was added and stirred for an additional 1 h to localize calcium ion at anionic aspartic acid layer. The intermediates were washed 3 times with deionized water to remove free calcium ions and sodium phosphate monobasic aqueous solution was added into the solution. The solution was stirred for 12 h to mineralize calcium phosphate layer and the final product was washed 3 times with deionized water through centrifugation at 10000 rpm. Morphology and the size distribution were analyzed by TEM and DLS, and the amount of encapsulated doxorubicin was evaluated by UV-Vis spectroscopy.

**Determination of doxorubicin release profiles.** In vitro release

profiles of doxorubicin from the PEGylated Dox-FeO<sub>x</sub>@CaP were evaluated with previously reported experimental setting. Two different aqueous solutions with the variation of pH and the concentrations of calcium and phosphate ions; an intracellular endosomal fluid (CaCl<sub>2</sub> 100 nM, Na<sub>2</sub>HPO<sub>4</sub> 40 mM, pH 4.5, NaCl 140 mM) and an extracellular fluid (CaCl<sub>2</sub> 2 mM, Na<sub>2</sub>HPO<sub>4</sub> 1 mM, Tris 25 mM, pH 7.4, NaCl 140 mM). 1 mL PEGylated Dox-FeO<sub>x</sub>@CaP was dispersed in aqueous buffer solution and transferred to a pre-swollen cellulose dialysis membrane with the molecular weight cut off of 1 K. The release profiles were obtained by dialysis against 20 mL release media and 5 mL aliquot was taken from the media before media exchange at a predetermined time interval. The amount of released doxorubicin was evaluated by UV-Vis spectroscopy.

**Cell viability.** In vitro cytotoxicity of PEGylated FeO<sub>x</sub>@CaP and PEGylated Dox-FeO<sub>x</sub>@CaP was evaluated by MTT colorimetric assay. HeLa cells were grown in 96-well plates at a density of 5x10<sup>3</sup> cells per well with 0.2 mL DMEM medium containing 10 % FBS. After 24 h incubation, cells were washed with pre-warmed DMEM medium before the treatment of nanoparticles. Cells were incubated for 24 h at 37 °C with the nanoparticles

and the cell viability was determined by the conventional MTT assay.

**In vivo study.** Hep3G cells ( $1 \times 10^6$  cells/mouse) cultured in RPMI 1640 medium containing 10% FBS were injected subcutaneously into the thigh of mice (BALB/C nu, 5-6 weeks old, male). When tumors had grown to 10~15 mm in size, the 0.1 mL PEGylated Dox-FeO<sub>x</sub>@CaP was intravenously injected through tail vein. For the positive control, same amount of PEGylated Dox-FeO<sub>x</sub>@CaP was intratumorally administered into the tumor tissue. Dose of PEGylated Dox-FeO<sub>x</sub>@CaP was determined based on amount of doxorubicin (2 mg/Kg).

MR images of each experimental group were evaluated by a human MRI scanner at 1.5-T field strength with a multi-spin echo multi-slice imaging sequence. T2 values in tumor and normal tissues were measured using following parameters: TR = 400 s, TE = 10 ms and slice thickness of 1 mm. MRI scanning was obtained from 3 mice and the relative intensity of T2 was averaged. MR images were obtained at predetermined time interval (0, 24, 48, 72, 96 and 120 h after administration).

After 120 h post injection, the mice were sacrificed and tumor tissues were excised. Fluorescence of the tumor tissues were measured with IVIS

imaging system (Caliper Life Science Inc., Hopkinton, MA) prior to Prussian blue staining. Tumors were imaged on the plate heated to 25 °C in IVIS imaging system and laser at a 488 nm wavelength was used to excite doxorubicin and fluorescence emission at 530 nm was collected with CCD camera in IVIS imaging system.

### **8.3. Results and discussion**

mPEG-Asp(OBzl)<sub>50</sub>-DOPAC was synthesized by ring opening polymerization of the L-aspartic acid 4-benzyl ester NCA, followed by DCC/DMAP coupling between N-terminus of the mPEG-Asp(OBzl) and DOPAC. The synthetic scheme is illustrated in Scheme 8-1. mPEG-NH<sub>2</sub> with the molecular weight of 5 K and  $M_w/M_n$  of 1.06 initiated the polymerization for the formation of mPEG-Asp(OBzl) block copolymers. Clear shift of the peak molecular weight to a higher molecular weight region was observed by GPC after polymerization, supporting the successful formation of block copolymers. mPEG-Asp(OBzl)<sub>50</sub>-DOPAC was characterized by UV spectrophotometer at 230 nm wavelength to have 0.9 DOPAC on average.

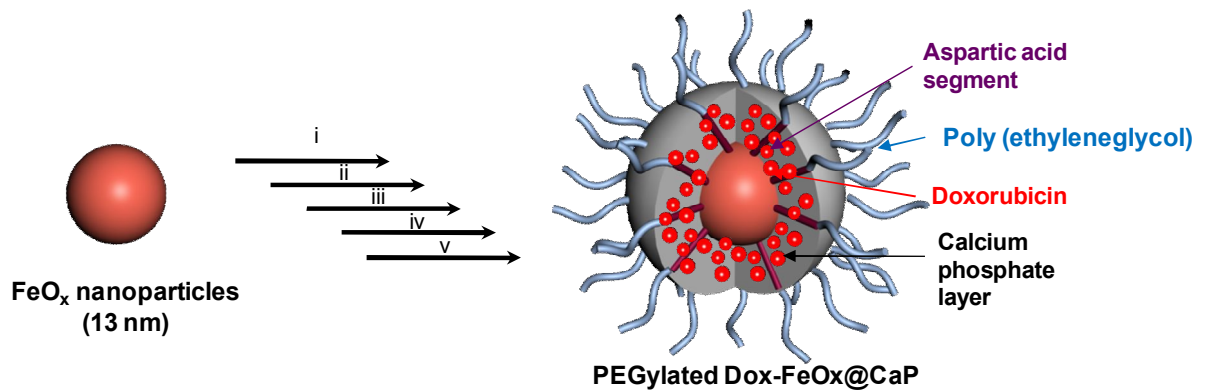


**Figure 8-1.** Fabrication method of PEGylated Dox-FeO<sub>x</sub>@CaP ; i) mPEG-Asp(Obzl)<sub>50</sub>-DOPAC, 12 h; ii) 0.1 N NaOH aq. solution, 6 h; iii) Dox, 2 h; iv) CaCl<sub>2</sub>, 1 h; v) Na<sub>2</sub>HPO<sub>4</sub>, 12 h.

Nanoparticles were designed by decorating mPEG-Asp-DOPAC on the surface of iron oxide nanoparticles with the size of 13 nm, followed by doxorubicin encapsulation and calcium phosphate (CaP) layer deposition. The nanoparticles consist of three defined domains: the hydrophilic PEG corona, drug-containing and structure-stabilizing CaP middle layer, and iron oxide core for magnetic resonance imaging. Overall scheme of PEGylated iron oxide nanoparticles with doxorubicin containing CaP layers (PEGylated Dox-FeO<sub>x</sub>@CaP) is shown in Figure 8-1. TEM images in Figure 8-2a show that CaP layer was successfully introduced on the surface of iron oxide with

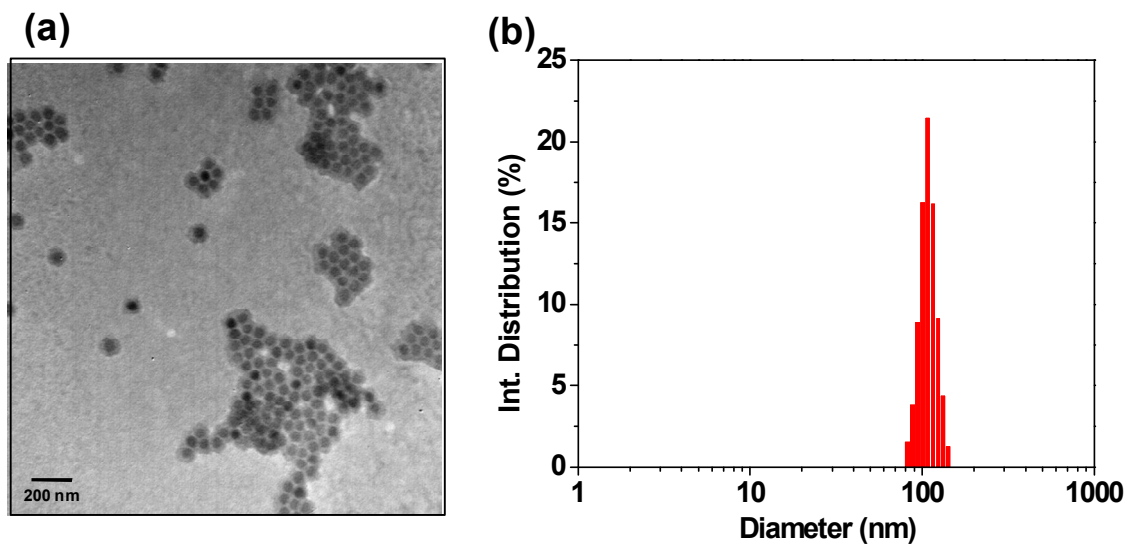


**Figure 8-2.** (a) TEM image and (b) size distribution in PBS of PEGylated Dox-FeO<sub>x</sub>@CaP.

the thickness around 20 nm. Aggregation between iron oxide nanoparticles and byproduct formation of free CaP particles were not observed. The mean hydrodynamic diameter of PEGylated Dox-FeO<sub>x</sub>@CaP was  $98.8 \pm 18.7$  nm by light scattering measurement (Figure 8-2b). PEG outer shell endowed the iron oxide with biocompatibility and enhanced stability in the blood stream for long-circulation and aspartic acid units in the block copolymer localized calcium cations for mineral deposition and doxorubicin by electrostatic

interaction. A half molar concentration of calcium to carboxyl acid groups in aspartic acid unit induced the successful mineralization and the CaP deposition at the middle layer without any noticeable formation of free CaP particles. High ionic concentration above the critical saturation level, achieved by the localization of calcium and phosphate ions at the block copolymers on the iron oxide, was believed to trigger the CaP deposition and the growth.

Several papers reported previously that charged organic molecules, such as fluorescence dye and chemotherapeutics, are able to co-mineralize during the formation of CaP layers. Doxorubicin, a positively charged anti-cancer drug, was successfully incorporated into the PEGylated Dox-FeO<sub>x</sub>@CaP, as described above in the experimental section. Doxorubicin was co-localized with calcium ions on the aspartic acid residues by electrostatic interaction. Quantitative calcium chloride, 0.5 equivalents against carboxyl acid groups of mPEG-Asp-DOPAC, was added and remaining carboxyl acid groups were interacted with doxorubicin. Loading amount and loading efficiency of doxorubicin were 5.3 % and 27.9 %, respectively. The loading amount was relatively lower than that from organic self-assembled structures such as micelles or self-aggregates

because of the high atomic mass of iron and the loading amount of 5.3 % was acceptable. Optimized drug delivery system is supposed to keep the drug within the vehicles during the circulation and release the drug at the disease site with burst or sustained pattern. The extracellular exterior (extracellular fluid, pH 7.4) and intracellular lysosomal interior (intracellular fluid, pH 4.5) conditions were employed to mimic the pH and ionic condition of blood stream and cellular uptake at disease site, respectively. Doxorubicin release profiles from PEGylated Dox-FeO<sub>x</sub>@CaP was shown in Figure 8-3. Release study was continued in two pre-determined conditions, extracellular and intracellular condition. PEGylated Dox-FeO<sub>x</sub>@CaP effectively inhibited the doxorubicin release in extracellular condition down to 11 % after 12 h, meaning that CaP layer is able to act as a diffusion barrier of encapsulated drugs during the blood circulation. Changing the media to the intracellular lysosomal condition, where pH is low enough to dissolve the CaP layer resulted in a triggered release of doxorubicin from 6 to 74 % in an additional 4 h. These results imply that the CaP layer successfully suppresses drug release in blood stream and PEGylated Dox-FeO<sub>x</sub>@CaP system selectively released the drugs at the

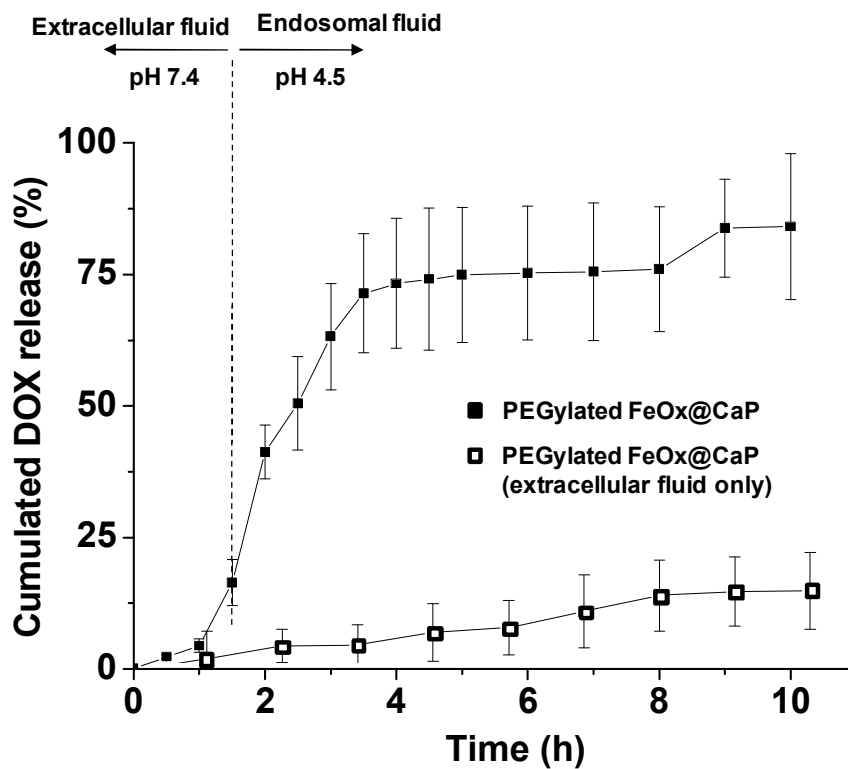


**Figure 8-3.** Doxorubicin release profile of PEGylated Dox-FeO<sub>x</sub>@CaP with media change (■) and without media change (□).

target without wasting them during the circulation. Considering these results, PEGylated Dox-FeO<sub>x</sub>@CaP is a stable nanocarrier with controllable drug release and a drug carrier with great potentials as intravenous delivery system.

Cell viability of PEGylated Dox-FeO<sub>x</sub>@CaP and PEGylated FeO<sub>x</sub>@CaP were evaluated with HeLa cells by MTT assay. As shown in Figure 8-4, cell viability was dramatically decreased with particle concentration for PEGylated Dox-FeO<sub>x</sub>@CaP after 24 h post treatment. The significant difference in cell viability between PEGylated Dox-FeO<sub>x</sub>@CaP and PEGylated FeO<sub>x</sub>@CaP was observed and these results were believed to stem from the doxorubicin release by the dissolution of CaP layer at the lower pH after cellular uptake of the nanoparticles into the endosome.

Magnetic resonance images were performed using tumor xenografted animal model and Hep3G was selected for target tumor. Human MRI scanner with 1.5 T magnetic fields was used to obtain MR images. Mice were imaged prior to injection of 0.1 mL PEGylated Dox-FeO<sub>x</sub>@CaP and injection dose was determined with consideration of amount of doxorubicin (2 mg/Kg of Dox). MRI contrast enhancement and images were evaluated at various time points after administration. After intratumoral injection of the PEGylated Dox-FeO<sub>x</sub>@CaP, tumor site became darker and T2 signal of the ROI was remained for 5 days (Figure 8-5a) due to the localized PEGylated Dox-FeO<sub>x</sub>@CaP. T2 signal was gradually decreased with time flow due to the removal of the PEGylated Dox-FeO<sub>x</sub>@CaP from tumor site. In contrast,

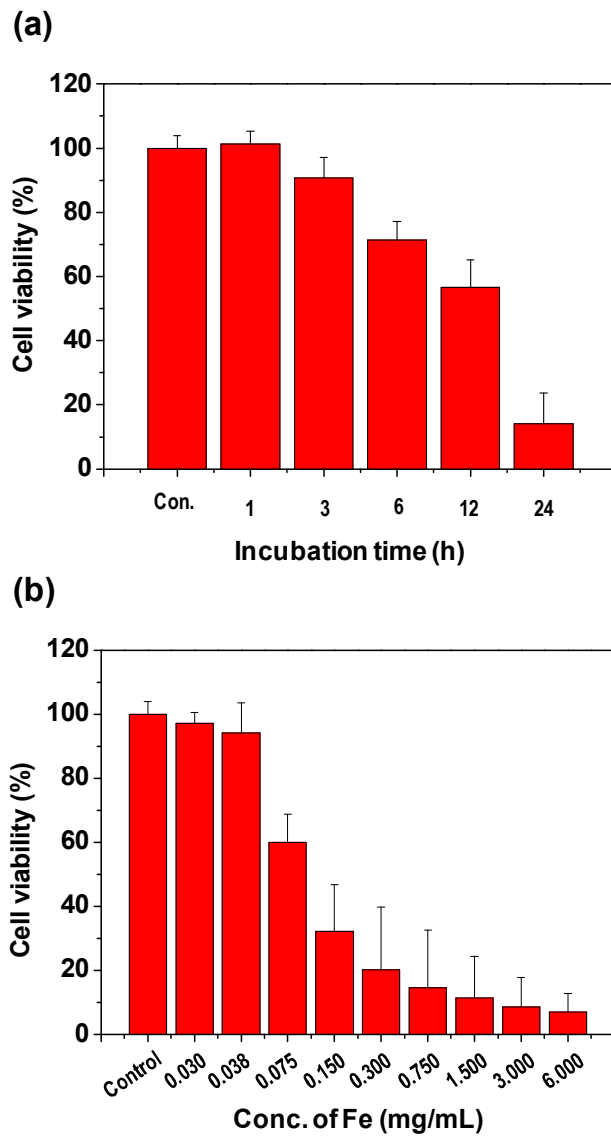


**Figure 8-4.** Cell viability of PEGylated Dox-FeO<sub>x</sub>@CaP as a function of (a) incubation time and (b) Fe concentration.

significant signal enhancement was not observed after intravenous injection of PEGylated Dox-FeO<sub>x</sub>@CaP (Figure 8-5b) because amount of accumulated PEGylated FeO<sub>x</sub>@CaP was not enough to detect by MRI scanner.

Presence of the iron oxide in tumor tissue was evaluated by immunohistology with Prussian blue staining (Figure 8-6). Prussian blue staining is well known method for iron detection in biological research. Prussian blue reaction involves the treatment of sections with acid solutions of ferrocyanides. Ferric ion present in the tissue combines with the ferrocyanide and results in the formation of a bright blue pigment called Prussian blue, or ferric ferrocyanide. As shown in Figure 8-6, Prussian blue staining demonstrated iron-containing sites as blue spots in the tumor tissue and these results mean that PEGylated FeO<sub>x</sub>@CaP was successfully accumulated at tumor tissue.

Accumulation of doxorubicin on tumor tissue was evaluated by fluorescence measurement using IVIS imaging system with 530 nm emission filter. To examine the accumulation of Dox in tumor tissues, we obtained ex vivo fluorescence images of tumor after intravenous injection and intratumoral injection PEGylated Dox-FeO<sub>x</sub>@CaP after 5 days post

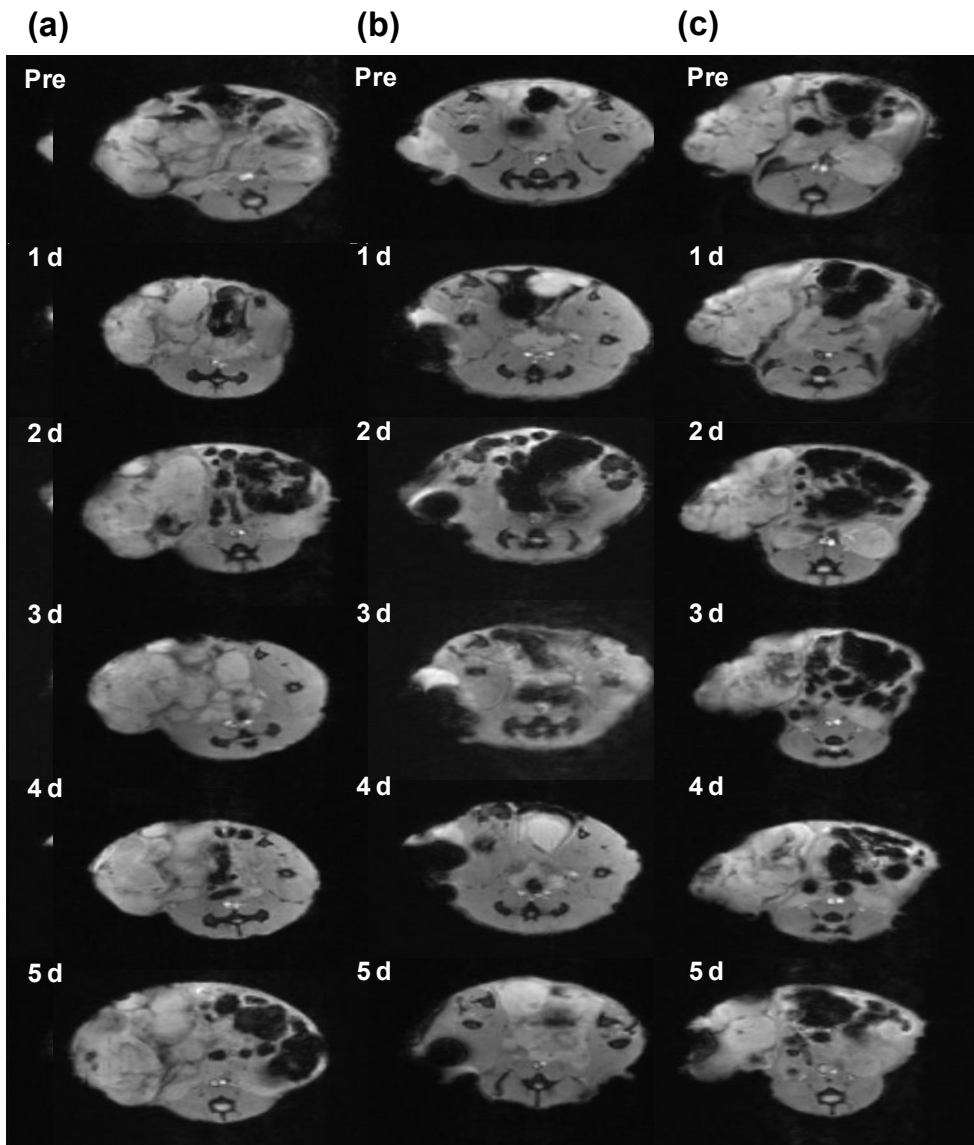


**Figure 8-5.** Magnetic resonance images after (a) intratumoral injection of particles, intravenous injection of (b) particles and (c) saline.

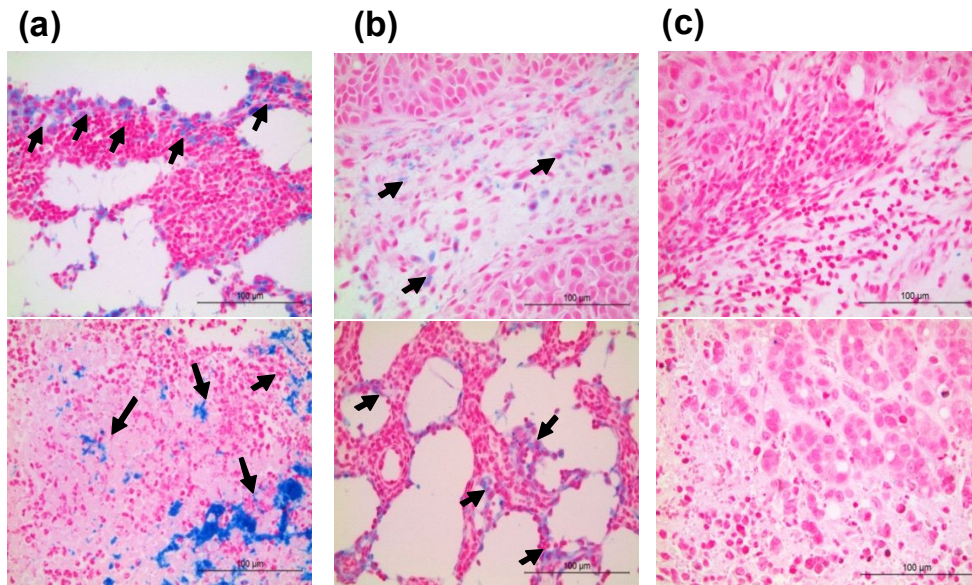


**Figure 8-6.** Immunohistological results with Prussian blue staining after (a) intratumoral injection of particles, intravenous injection of (b) particles and (c) saline.

administration. The images showed a relatively intense fluorescence signal exclusively in the tumor areas 5 days after injection of PEGylated Dox-FeO<sub>x</sub>@CaP, which is indicative of successful accumulation and the release of Dox within the tumor area (Figure 8-7). The fluorescence intensity of tumor tissues of intratumorally and intravenously injected mice was higher

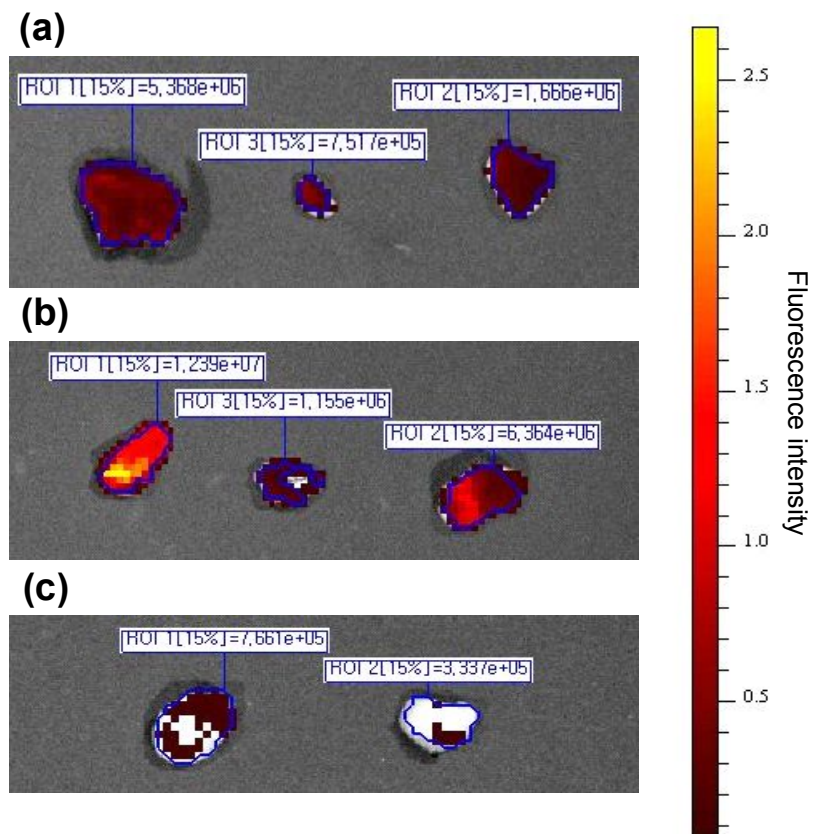


**Figure 8-7.** Fluorescence image of tumors at 530 nm emission after (a) intratumoral injection of particles, intravenous injection of (b) particles and (C) saline.

7 times and 3 times than control group, respectively. These results suggest that doxorubicin was successfully delivered to the tumor site by PEGylated Dox-FeO<sub>x</sub>@CaP and then released from the nanoparticles.

#### **8.4. Conclusion**

In this study, PEGylated Dox-FeO<sub>x</sub>@CaP was developed and its potential as a theragnostic agent for MR imaging and cancer therapy was evaluated. Iron oxide nanoparticles were stabilized with PEG outer shell and CaP layer encapsulating doxorubicin. PEGylated Dox-FeO<sub>x</sub>@CaP was stable in the physiological conditions over a week and showed low cytotoxicity enough to apply as an in vivo imaging agents. Nanoparticles showed increased drug release rate in the intracellular endosomal/lysosomal fluid while the release was limited in the extracellular fluid due to the selective dissolution of CaP layers by decreased pH. In addition, prepared nanoparticles were successfully accumulated at tumor site in vivo after intravenous administration. These results promise that PEGylated Dox-FeO<sub>x</sub>@CaP can be used as a stimuli-sensitive, such as pH and ion concentration, drug delivery system and provide a new platform as theragnostic nanoparticles.

#### **8. 5. References**

- [1] M. Arruebo, R. FernLndez-Pacheco, M. R. Ibarra, and J. Santamar Ma, *Nano Today* **2007**, 2, 22.

- [2] A. M. Derfus, G. von Maltzahn, T. J. Harris, T. Duza, K. S. Vecchio, E. Ruoslahti, and S. N. Bhatia, *Adv. Mater.* **2007**, *19*, 3932.
- [3] N. Kohler, C. Sun, A. Fichtenholtz, J. Gunn, C. Fang, and M. Zhang, *Small* **2006**, *2*, 785.
- [4] C. Alexiou, *Eur. Biophys. J.* **2006**, *35*, 446.
- [5] T. K. Jain, M. A. Morales, S. K. Sahoo, D. L. Leslie-Pelecky, and V. Labhasetwar, *Mol. Pharmacol.* **2005**, *2*, 194.
- [6] X. Wang, *J. Biomed. Mater. Res. Part A* **2007**, *80*, 852.
- [7] J. Yang, C. H. Lee, H. J. Ko, J. S. Suh, H. G. Yoon, K. Lee, Y. M. Huh, and S. Haam, *Angew. Chem.* **2007**, *119*, 8992.
- [8] J. Yang, C. H. Lee, H. J. Ko, J. S. Suh, H. G. Yoon, K. Lee, Y. M. Huh, and S. Haam, *Angew. Chem. Int. Ed.* **2007**, *46*, 8836.
- [9] R. Weissleder, D. D. Stark, B. L. Engelstad, B. R. Bacon, C. C. Compton, D. L. White, P. Jacobs, and J. Lewis, *Am. J. Roentgenol.* **1989**, *152*, 167.
- [10] P. Bourrinet, H. H. Bengel, B. Bonnemain, A. Dencausse, J. M. Idee, P. M. Jacobs, J. M. Lewis, *Invest. Radiol.* **2006**, *41*, 313.
- [11] M. K. Yu, Y. Y. Jeong, J. Park, S. Park, J. W. Kim, J. J. Min, K. Kim, and S. Jon, *Angew. Chem. Int. Ed.* **2008**, *47*, 5362.

- [12] C. Alexiou, W. Arnold, R. J. Klein, F. G. Parak, P. Hulin, C. Bergemann, W. Erhardt, S. Wagenpfeil, and A. S. Lübke, *Cancer Res.* **2000**, *60*, 6641.
- [13] H. Bin Na, I. S. Lee, H. Seo, Y. I. Park, J. H. Lee, S. W. Kim and T. Hyeon, *Chem. Commun.* **2007**, *48*, 5167.
- [14] P. Pradhan, J. Giri, F. Rieken, C. Koch, O. Mykhaylyk, M. Doblinger, R. Banerjee, D. Bahadur and C. Plank, *J. Control. Release* **2010**, *142*, 108.
- [15] C. R. Sun, K. Du, C. Fang, N. Bhattarai, O. Veiseh, F. Kievit, Z. Stephen, D. H. Lee, R. G. Ellenbogen, B. Ratner and M. Q. Zhang, *ACS Nano* **2010**, *4*, 2402.
- [16] O. Veiseh, J. W. Gunn, F. M. Kievit, C. Sun, C. Fang, J. S. H. Lee and M. Q. Zhang, *Small* **2009**, *5*, 256.
- [17] S. Nappini, F. B. Bombelli, M. Bonini, B. Norden and P. Baglioni, *Soft Matter* **2010**, *6*, 154.
- [18] O. Veiseh, F. M. Kievit, C. Fang, N. Mu, S. Jana, M. C. Leung, H. Mok, R. G. Ellenbogen, J. O. Park and M. Zhang, *Biomaterials* **2010**, *31*, 8032.
- [19] B. R. Jarrett, B. Gustafsson, D. L. Kukis and A. Y. Louie,

*Bioconjugate Chem.* **2008**, *19*, 1496.

- [20] C. J. Xu, K. M. Xu, H. W. Gu, R. K. Zheng, H. Liu, X. X. Zhang, Z. H. Guo and B. Xu, *J. Am. Chem. Soc.* **2004**, *126*, 9938.
- [21] E. Y. Sun, L. Josephson and R. Weissleder, *Mol. Imaging* **2006**, *5*, 122.
- [22] E.-J. Cha, I.-C. Sun, S. C. Lee, K. Kim, I. C. Kwon, and C.-H. Ahn, *Macromol. Res.* **2012**, *20*, 319.

## 국문 요약

다양한 분자영상 기법과 효율적인 약물 전달 시스템을 접목하여 질병의 진단과 동시에 치료를 하는 테라그노시스 (theragnosis) 는 최근 관련 분야에서 가장 관심을 받고 있는 연구 분야이다. 본 연구에서는 초상자성 산화철 나노입자 기반의 다양한 진단용 프로브를 개발하였고, 약물 전달 시스템에 응용 가능한 고분자 마이셀을 제조하였으며, 이러한 연구 결과를 바탕으로 테라그노시스에 응용 할 수 있는 나노입자를 합성하는 연구를 수행하였다.

연구의 첫 부분에서는 초상자성 산화철 나노입자의 형광 소광 효과를 검증하고, 실리카 및 글라이콜 키토산으로 코팅된 산화철 나노입자 표면에 암에서 과다 발현되는 MMP 효소의 분해반응에 의해 선택적으로 형광 복원이 가능한 펩타이드-형광체를 도입하여 암을 선택적으로 영상화 할 수 있는 진단용 프로브를 개발하였다.

두 번째 연구에서는 접합점에 카르복실산 기능기를 도입한 양친성 블록 공중합체를 합성하고, 이를 기반으로 마이셀 구조의 약물

전달체를 개발하는 연구를 수행하였다. 접합점에 도입된 기능기와 칼슘 양이온 및 양전하를 띠는 약물과의 이온결합을 이용하여 마이셀의 안정성을 높여 효율적인 약물 전달이 가능한 약물 전달체로의 가능성을 입증하였다.

마지막으로 진단과 약물 전달에 의한 치료에 관한 앞선 연구 결과들을 바탕으로 테라그노시스에 응용 가능한 나노입자를 개발하는 연구를 수행하였다. CT와 MRI 조영제로 각각 응용이 가능한 금 나노입자와 산화철 나노입자의 표면에 약물을 효율적으로 담지 할 수 있는 고분자/인산칼슘 기반의 코팅층을 도입하여 선택적인 약물 전달과 동시에 영상화가 가능한 하이브리드 나노입자를 제조하여 테라그노시스로의 응용 가능성을 확인하였다.

**주요어:** 테라그노시스, 분자영상, 산화철 나노입자, 금 나노입자, 약물전달시스템

**학 번:** 2007-30810